Electron beam calibration of aerogel for the HELIX RICH

Emma Ellingwood

Master of Science

Department of Physics

McGill University

Montreal, Quebec

2020-08-11

A thesis submitted to McGill University in partial fulfillment
of the requirements of the degree of Master of Science

ACKNOWLEDGEMENTS

Many people were involved in making this research possible. First and foremost I want to thank my supervisor David Hanna for his support and advice throughout my research and especially for his feedback while writing this thesis. I would also like to thank Thomas Rosin and Ste O'Brien for all of their work on this project. Building, setting up and running the calibration system is truly a group effort and it would not be where it is today without all our work on this project together and our endless discussions. Thank you to the rest of the research group for their feedback and advice during group meetings and office discussions.

Thank you to the staff at the National Research Council. Stewart Walker, for fixing and running the accelerator and staying late to make our short trips productive. Malcolm MacEwan and Bryan Muir for troubleshooting the linac and also making time for us to use the linac in their own busy schedules. Also, thanks to Adam Gilbert for designing the CCD board and helping us fix it whenever we managed to cause a problem.

Thank you to my parents and my siblings for their support and patience with me throughout my MSc.

ABSTRACT

The High Energy Light Isotope eXperiment (HELIX) is a balloon-borne detector, currently in development, to measure the chemical and isotopic abundances of light cosmic-ray nuclei. One of the primary goals is to measure the ^{10}Be/^{9}Be ratio for 0.2 - 10 GeV/n over two flights. ^{10}Be is a radioactive isotope with a half-life of 1.39 Myr so its abundance, compared to the stable ^{9}Be, constrains cosmic-ray propagation models. HELIX consists of a 1 Tesla superconducting magnet and a drift chamber tracker to measure the particle rigidity. The velocity is measured with a time-of-flight system and a ring-imaging Cherenkov detector (RICH). The RICH radiator plane consists of 32 aerogel tiles with a refractive index of n = 1.15 - 1.16 and four NaF tiles. In order to achieve the desired HELIX mass resolution of 2.5 %, the aerogel refractive index n must be known to a resolution of less than 0.07 %. Due to the fabrication process, the refractive index variations for each tile could be larger than 0.07 %, which requires measuring the refractive index changes in a grid along each aerogel tile. In this thesis, I will describe the calibration system designed to measure aerogel tile refractive index variations using an electron linear accelerator. I will also explore the effect of the properties of the electron beam and the calibration system on producing accurate and precise refractive index and particle velocity measurements.

ABRÉGÉ

Le High Energy Light Isotope eXperiment (HELIX) est un détecteur en ballon, présentement en développement, pour mesurer l'abondance chimique et isotopique des noyaux de rayons cosmiques légers. Un des objectifs principaux est de mesurer le rapport ^{10}Be/^{9}Be pour 0.2 - 10 GeV/n au cours de deux vols. ^{10}Be est un isotope radioactif avec une demi-vie de 1.39 millions d'années alors son abondance, en comparaison avec ^{9}Be qui est stable, limite les modèles de propagation des rayons cosmiques. HELIX consiste d'un aiment supraconducteur de 1 Tesla et une chambre de dérive pour mesurer la rigidité de la particule. La vélocité est mesurée avec des détecteurs temps-de-vol et un détecteur Cherenkov (RICH). Le plan radiateur RICH contient 32 tuiles d'aérogel avec un indice de réfraction de n = 1,15 - 1,16 et quatre tuiles de NaF. Pour atteindre la résolution de masse désirée d'HELIX de 2,5 %, il faut que l'indice de réfraction n soit connu à une résolution moins que 0,07 %. À cause du processus de fabrication, les variations d'indice de réfraction pour chaque tuile pouvait être plus grand que 0,07 %, qui rend nécessaire des mesures des changements de l'indice de réfraction sur une grille à travers chaque tuile d'aérogel. Dans cette thèse, je vais décrire le système d'étalonnage conçu pour mesurer la variation de l'indice de réfraction de la tuile d'aérogel avec un accélérateur linéaire d'électrons. Je vais aussi examiner l'effet des propriétés du faisceau d'électrons et le système d'étalonnage sur la production des mesures exactes et précises de l'indice de réfraction et la vélocité des particules.

CONTRIBUTION OF AUTHOR

The purpose of this thesis is to describe the development and running of a detector to map the refractive index of aerogel tiles and to explore the system's systematic uncertainties. Original contributions from the author are as follows:

- Chapter 3: The author was involved in all aspects of building, troubleshooting, improving and running the calibration system described in the thesis. This chapter is a summary of the calibration system that was built and run alongside work from Thomas Rosin, Ste O'Brien and David Hanna.
- Chapter 4: This chapter is a description of the analysis code written by Ste O'Brien. All of the text and the plots to explain the analysis code were done by the author.
- Chapter 5: All of the studies done using the RICH Geant4 simulation and studies of the effects of changing calibration parameters and distinguishing isotopes are original work by the author.

Chapter 1, 2 and Appendix A present information that can be found in literature. Appendix B is written by the author, but the measurements were done with Ste and Thomas.

TABLE OF CONTENTS

ACKNOWLEDGEMENTS ii

ABSTRACT iii

ABRÉGÉ iv

CONTRIBUTION OF AUTHOR v

LIST OF FIGURES ix

LIST OF TABLES xi

1 Introduction 1

1.1 History 1
1.2 Spectrum 2
1.3 Composition of Cosmic Rays 3
1.3.1 Primary 3
1.3.2 Galactic 4
1.3.3 Electrons and Positrons 5
1.4 Secondary-to-Primary Ratios 6
1.5 Radioactive Clock Isotopes 7
1.6 Propagation Mechanisms 9
1.6.1 Leaky Box Model 9
1.6.2 More Complex Models 10
1.6.3 Transport Equation for Primary Cosmic Rays 11
1.7 HELIX Scientific Motivation 12

2 High Energy Light Isotope Experiment (HELIX) 14

2.1 Overview of Balloon-Borne Experiments 14
2.2 Detector Background Information 15
2.2.1 Measurement Goals 15
2.2.2 Expected Resolution 17
2.3 HELIX Detector Components 19
2.3.1 Superconducting Magnet 19
2.3.2 Drift Chamber Tracker 20
2.3.3 Time-of-Flight 21
2.3.4 Ring-Imaging Cherenkov Detector 22
2.4 Aerogel Manufacturing and Properties 23
2.4.1 Aerogel Production 23
2.4.2 Fabricating the Aerogel 24
2.4.3 Aerogel Properties 25

3 Aerogel Calibration System 27

3.1 Aerogel Calibration Background 27
3.1.1 Motivation for Aerogel Calibration 27
3.1.2 Cherenkov Ring Measurement Geometry 28
3.1.3 Measuring the Cherenkov Ring 29
3.1.4 Previous Aerogel Calibration Experiments 30
3.1.5 Challenges in Measuring the Aerogel Refractive Index . . . 31
3.1.6 Method Adopted for Calibration 32
3.1.7 Requirements 34
3.2 HELIX Aerogel Calibration System Components 34
3.2.1 Electron Beam 34
3.2.2 Charge Coupled Devices 35
3.2.3 The Cherenkov Ring Detection Board 37
3.3 Readout Sequence and Electronics 38
3.3.1 Linac Electronic Pulses 38
3.3.2 CCD Timing Signals 39
3.3.3 Data Acquisition Computer 41
3.3.4 CCD Settings 42
3.4 Scanning Setup 43
3.4.1 Detection Board Position and Orientation 44
3.4.2 Detection Board Positioning System 45
3.4.3 Aerogel Frame and Holder 45
3.4.4 Aerogel Scan Coordinate System 46
3.4.5 Frame Scanning System 47
3.4.6 Frame and Board Systems Power and Control 47
3.5 Scanning Procedure 47
3.5.1 Pre-Beam System Checks 47
3.5.2 Initialization 48
3.5.3 Graphical User Interface 49
3.5.4 Grid Scan Parameters 50
3.5.5 Data Formatting and Management 50
3.5.6 Beam Scan Timing 51
3.6 Data Summary 53

4 Aerogel Scan Analysis 55

4.1 Mapping CCD Output to Physical Position 55
4.2 Determining the Peak of the Cherenkov Ring 57
4.3 χ^2 Cut to Poor Parabolic Fits 58
4.4 Excluding CCDs 61
4.5 Fitting Data to a Circle 62
4.6 Calculating the Refractive Index 62
4.7 Producing Refractive Index Maps 64

5 Exploring Aerogel Scan Systematic Uncertainties 66

5.1 Simulating the Cherenkov Ring with Geant4 66
5.1.1 Simulation Setup 66
5.1.2 Analyzing Geant4 Results 67
5.1.3 Determining the Beam Divergence for Geant4 68
5.1.4 Contributions to the Cherenkov Ring Width 69
5.1.5 Cherenkov Ring Width Dependence on Aerogel Tile Thickness 72
5.1.6 Calculating the Refractive Index of Simulations 73
5.2 Effect of Parameter Variations on the Refractive Index 75
5.2.1 Distance d Variations 75
5.2.2 Half-Thickness z_e Variations 76
5.3 Distinguishing Isotopes with Refractive Index and Rigidity Variations 77
5.3.1 Adding Variations to the Refractive Index and Rigidity . . 78
5.3.2 Comparing Precision and Accuracy in Index Measurements 80

6 Conclusion 82

APPENDIX A: The Cherenkov Effect 83

APPENDIX B: Distance Calibration 84

REFERENCES 85

LIST OF FIGURES

Figure		page
1–1	Cosmic-ray all-particle energy spectrum	2
1–2	Differential energy spectrum of primary cosmic rays	3
1–3	Composition of Galactic cosmic rays	4
1–4	The cosmic-ray positron fraction	5
1–5	The B/C ratio	6
1–6	^{10}Be/^{9}Be ratio as a function of energy per nucleon	8
1–7	Leaky box model diagram	9
1–8	^{10}Be/^{9}Be for different diffusive halo half thicknesses	11
2–1	NASA balloon launch at McMurdo Station	14
2–2	HELIX mass resolution requirements	18
2–3	Mass resolution of HELIX components	18
2–4	The HELIX detector	20
2–5	The HELIX RICH detector	22
2–6	Pinhole drying aerogel procedure	25
2–7	Picture of aerogel tile in its frame	26
2–8	Transmittance and mean corner refractive index of aerogel	26
3–1	Geometry of the Cherenkov photon path through aerogel	28
3–2	Position of CCDs for the aerogel calibration system	33
3–3	Linear accelerator exit window with aerogel and laser alignment	35
3–4	Toshiba TCD1304DG CCD	36
3–5	CCD diagram from datasheet	36
3–6	Photograph of the Cherenkov ring detection board	37
3–7	CCD timing and control pulses relative to the beam pulse	39
3–8	NIM and CAMAC logic diagram for CCD timing signals	40
3–9	Single CCD readout for the Cherenkov ring profile and a dark frame	43

3–10 Single CCD readout with background subtracted 43
3–11 Digital model of the aerogel calibration system 44
3–12 The back of the detection board system 44
3–13 Aerogel frame and holder 45
3–14 HELIX aerogel calibration coordinate system 46
3–15 Graphical user interface for the scanning system 49
4–1 Sample Cherenkov ring profile and mapping pixel to board position . 55
4–2 Matching the CCD output to the true position 57
4–3 The parabolic fits to the Cherenkov ring CCD profile 58
4–4 Background wave in dark frame traces 59
4–5 Acceptable and excluded CCD readouts 61
4–6 Board view of blocked Cherenkov light 61
4–7 Fitting the CCD readouts with a circle 62
4–8 Refractive index maps 65
5–1 Geant4 simulation diagram 66
5–2 Comparing simulated photon distribution compared to real CCD . . . 67
5–3 Comparing Geant4 and data 68
5–4 Contributions to the Cherenkov ring width 70
5–5 Simulated energy distribution of electrons for different electron processes 71
5–6 The effect of changing the tile thickness on the Cherenkov ring width 73
5–7 Calculating n for a Geant4 simulation 74
5–8 Refractive index change due to aerogel-CCD distance 76
5–9 Refractive index change due to half-thickness z_e 77
5–10 Effect of n and R variations on distinguishing ^{10}Be and ^{9}Be 78
5–11 Precision and accuracy of n measurements in β-R 80
A-1 Huygens wavelets diagram 83

LIST OF TABLES

Table page

1–1 Primary scientific goals of HELIX 13

3–1 Aerogel scan logbook summary 54

CHAPTER 1
Introduction

The High Energy Light Isotope eXperiment (HELIX) is a new balloon-borne experiment designed to measure the isotopic composition of light cosmic-ray nuclei. It will be launched during the NASA Antarctic Balloon Campaign in 2021/2022. One of its principal goals is to make high precision measurements of the ^{10}Be/^{9}Be ratio, which is a key measurement in distinguishing cosmic-ray propagation models. This chapter provides background information on cosmic rays to motivate the scientific goals of HELIX. The proceeding chapters will be a description of the HELIX experiment followed by the aerogel calibration system. The calibration system is designed to measure the refractive index variations across the aerogel used in the HELIX ring-imaging Cherenkov detector. It will be followed by a series of simulations and calculations to understand sources of systematic uncertainty caused by the calibration system and the electron beam properties.

1.1 History

The history of cosmic rays is closely linked to the history of radioactivity with early detections by Hess and Wulf. Theodor Wulf expected that spontaneous penetrating radioactive emission came from the Earth. He brought electroscopes to the top of the Eiffel tower and he noted a decrease in the event rate he observed compared to the ground, but not as much as he predicted [1].

Victor Hess then carried out similar measurements using three electroscopes on multiple hot-air balloon flights in 1912, reaching a height of 5350 m [2, 3]. He observed a decrease in counts up to 1000 m, consistent with the ground based radiation theory and Wulf's results. However, that theory did not explain the increase in the count rate at higher altitudes. He concluded that the source of radiation must therefore come from above the atmosphere. This is considered the first observation of cosmic rays,

which was followed by the discovery of the positron in 1932 [4] and the observation of what turned out to be muons in 1937 [5].

These discoveries led to the emergence of the field of cosmic-ray astrophysics. Research in this field includes measurements of the composition of cosmic rays and trying to understand the sources and propagation mechanisms of these particles.

1.2 Spectrum

Fig. 1–1 is the cosmic-ray energy spectrum showing results from different experiments. There are three features of this spectrum that will be discussed: the knee, the second knee and the ankle.

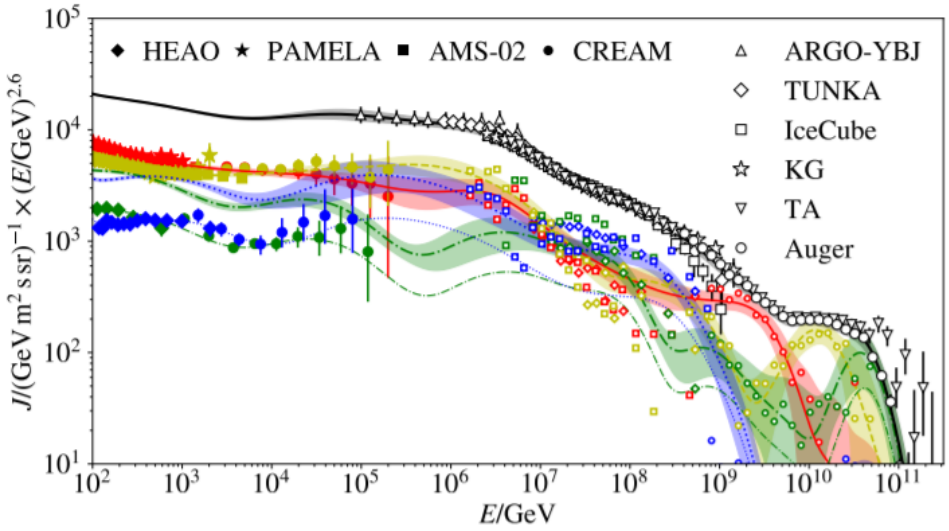

Figure 1–1: Cosmic-ray all-particle energy spectrum with data from different experiments. TA is the Telescope Array and KG is KASCADE-Grande. The lines are global spline fit models for specific nuclei or groups of nuclei. This plot includes the all-particle flux (black), protons (red), helium (yellow), oxygen group (green) and iron group (blue). The oxygen group is Li - F and the iron group is Na - Ni, named after the nucleus that contributes most to the flux. Image Source: [6].

The knee is one of the key features in the cosmic-ray spectrum, at about 3×10^6 GeV [6, 7]. This feature could indicate that there is a maximum energy for Galactic cosmic accelerators, for example, in the shock front of a supernova [8, 9]. The knee has also been associated with a higher escape rate of particles in the Galaxy at this energy, as discussed in [8]. The second knee is observed by experiments on the order of 10^8 GeV. This is often associated with a greater contribution of heavier nuclei to the spectrum.

The ankle of the spectrum is at approximately 3×10^9 GeV and it is postulated to be due to extragalactic sources becoming the dominant flux source [7].

At about 3×10^{10} GeV [7], it is theorized there should be a quick decrease of the spectrum when inelastic collisions of cosmic rays and CMB photons, such as $p + \gamma_{CMB} \rightarrow p + \pi^0$ and $p + \gamma_{CMB} \rightarrow n + \pi^+$, start to become a dominant feature. This is known as the Greisen-Zatsepin-Kuzmin (GZK) limit [10, 11].

1.3 Composition of Cosmic Rays

This section focuses on the various cosmic-ray particles that are either primaries produced by astrophysical sources or secondaries produced by spallation of primary cosmic rays with the interstellar medium (ISM).

1.3.1 Primary

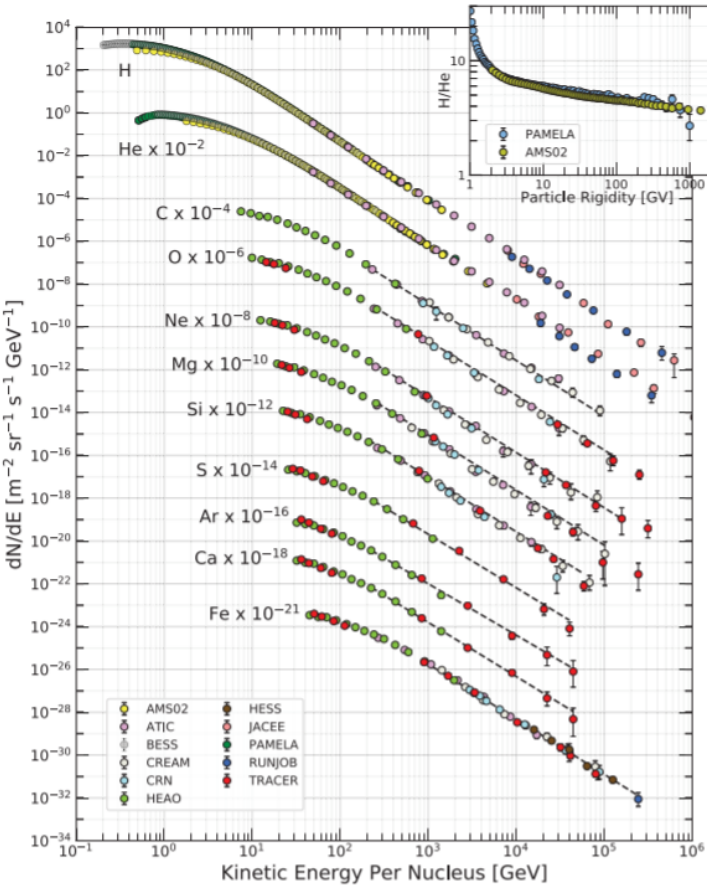

Figure 1–2: The differential energy spectrum flux of primary cosmic rays as a function of the kinetic energy per nucleus. The inset is the H/He ratio for a given rigidity. The flux is scaled for each species to make it easier to read. Image Source: [7].

Primary cosmic rays consist of those elements that are produced and accelerated by astrophysical sources including e^-, p, He, C, O and Fe [7]. Some of these particles will originate from the Sun, but in general these particles are Galactic or extragalactic in origin [7]. Although cosmic rays are expected from sources such as supernova remnants [12], it can be difficult to determine their origin due to multiple magnetic fields and materials these particles can interact with as they travel. The trajectories of the cosmic rays bend in the magnetic field so that they do not point directly to their source. Cosmic-ray propagation will be discussed in Section 1.6.

The composition of primary cosmic rays is dependent on the energy of the particle. It is about 86 % protons, 11 % alpha particles, 1 % heavier nuclei and 2 % electrons [13]. The energy spectra of several primary cosmic-ray nuclei are shown in Fig. 1–2, which includes data from multiple experiments. The primary cosmic rays at lower energies than the spectrum knee obey the differential intensity equation [7]

$$I_N(E) \approx 1.8 \times 10^4 (E/1 \text{ GeV})^{-2.7} \frac{\text{nucleons}}{\text{m}^2 \text{ s sr GeV}} . \tag{1.1}$$

1.3.2 Galactic

The chemical composition of Galactic cosmic rays is presented in Fig. 1–3 where the composition is graphed in terms of abundance relative to C. Often this composition is compared to the chemical composition of the Solar System due to the striking similarities in the relative abundances of nuclei. These similarities point to the possibility that Galactic cosmic rays originate

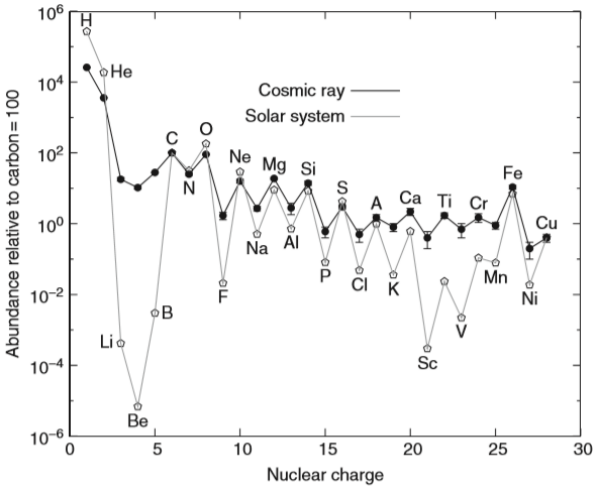

Figure 1–3: The nuclear abundance of Galactic cosmic rays compared to the Solar System composition. Image Source: [14].

from stars or stellar remnants so the cosmic-ray nuclei from those sources have a similar composition.

A notable trait in Fig. 1–3 is the low amount of Li, Be and B in the Solar System; they are much more abundant in Galactic cosmic rays. Those elements are not generally formed during nucleosynthesis or nuclear fusion. They are almost exclusively spallation products from heavier nuclei like C and O. Some of these nuclei are unstable, such as ^{10}Be. There is a similar trend for nuclei like Sc, Ti, V and Mn, from the spallation of Fe and Ni [13].

1.3.3 Electrons and Positrons

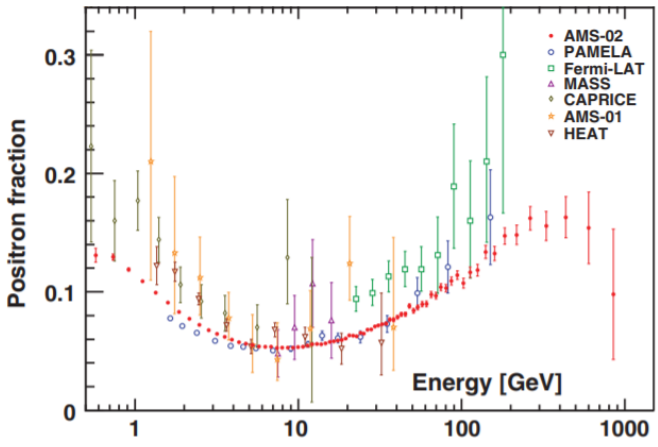

Figure 1–4: The cosmic-ray positron fraction $e^+/(e^+ + e^-)$ with results from multiple experiment. Image Credit: [15].

Electrons and positrons are a key measurement by a number of direct and indirect cosmic-ray experiments. The positron fraction $e^+/(e^+ + e^-)$ is particularly interesting because several experiments, including AMS-02 [15], have measured an increase above about 20 GeV, as seen in Fig. 1–4. Cosmic-ray models must be adjusted to account for the observed increase [16]. The electron and positron fluxes have distinctly different flux structures, which suggests that they must come from different sources [15]. The positron flux is postulated to be a result of a diffuse term from cosmic-ray collisions at low energies, and from a source term at high energy with cutoff at 810 GeV [16]. This new source is consistent with either an astrophysical object, such as a pulsar, or from dark matter annihilation [16, 17].

A definitive explanation for the observed increase past 20 GeV is particularly difficult since the exact cosmic-ray propagation mechanism is not well understood.

Measurements of the isotopic composition would be useful to constrain the propagation models.

1.4 Secondary-to-Primary Ratios

Primary cosmic rays are nuclei produced and accelerated by astrophysical sources, as discussed in Section 1.3.1. Secondary cosmic rays are those produced in the spallation of the heavier primary nuclei with the interstellar medium (ISM). Since the secondary nuclei are exclusively produced during primary cosmic-ray propagation, the ratio of secondary to primary cosmic rays helps to probe cosmic-ray propagation mechanisms [19]. Secondary-to-primary ratios can refer to ones where both nuclei are stable, as discussed in this section, or where one is unstable, discussed in Section 1.5.

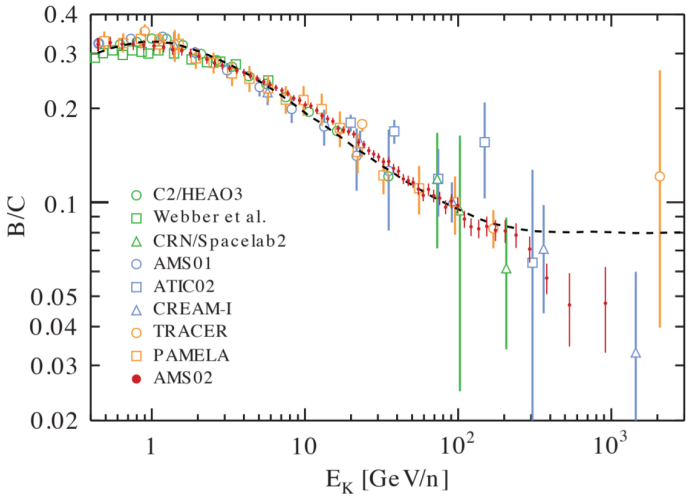

Figure 1–5: The boron to carbon (B/C) ratio in terms of the kinetic energy per nucleon for multiple experiments. The dashed line is the ratio for the model in [18]. Image Source: [19].

The most commonly measured secondary-to-primary ratio is the boron to carbon ratio (B/C). Secondary cosmic-ray B is formed by spallation of primary cosmic-rays like C, N and O from interactions with the ISM. Consider a simple case where the spallation of C and O produces B. For a simple propagation model, like the Leaky Box model discussed in Section 1.6.1, assume that there is a particle lifetime τ and an interaction length λ_B of B in the Galaxy. For a given species, this lifetime τ can include the expected escape time out of the Galaxy halo or loss due to spallation [20]. Since B is a secondary particle and some of it is formed by the C spallation, the density of C, N_C, should influence the amount of B, N_B, and it should depend

on the amount of interaction with the ISM. The notation N_i refers to the density of cosmic-ray species i at specific point in the Galaxy and differential in energy [14]. Assuming C and O have the same Galactic flux, the B/C ratio can be estimated by [14]

$$\frac{N_B}{N_C} = \frac{\lambda_{esc}(E)}{1 + \lambda_{esc}(E)/\lambda_B} \frac{\sigma_{C\to B} + \sigma_{O\to B}}{m_p} \ , \tag{1.2}$$

where $\lambda_{esc}(E) = \beta c \rho \tau_{esc}(E)$ is the escape length, the mean amount of matter that the particle goes through. βc is the particle velocity, ρ is the density of the ISM and $\tau_{esc}(E)$ is the mean containment time for particles in the halo of the Leaky Box model. λ_B is the interaction length of B in the Galaxy ≈ 71 kg/m^2, $\sigma_{C\to B}$ and $\sigma_{O\to B}$ are cross sections of the spallation to boron from carbon and oxygen, respectively [14]. The majority of the ISM is made up of protons with mass m_p.

The B/C ratio has been measured by a number of experiments, as shown in Fig. 1–5. Comparing this data with a model and known spallation cross sections, $\sigma_{C\to B} \approx 73$ mb and $\sigma_{O\to B} \approx 30$ mb [14], allows for a prediction of $\lambda_{esc}(E)$, the amount of material that the cosmic rays have traversed as a function of energy [14]. The spallation cross section and the escape time τ_{esc}(E) are energy dependent, which is reflected in the energy dependence in Fig. 1–5. Therefore, it is important to have multiple measurements of B/C covering a wide range of energies to fit an accurate model. For one example from [14] using the Leaky Box model and Eq. 1.2, a particle with 5 GeV/n corresponds to a ratio of 0.239, which results in λ_{esc}=85 kg/m^2. λ_{esc} decreases with increasing energy. These measurements of λ_{esc} alone are not enough to fully constrain the propagation model. Another ratio, like a radioactive clock isotope ratio, is necessary to provide further constraints.

1.5 Radioactive Clock Isotopes

Cosmic-ray spallation produces both stable isotopes, such as ^{10}B and ^{11}B, and unstable ones, such as ^{10}Be, ^{26}Al, ^{54}Mn and ^{36}Cl isotopes [21]. These unstable radioactive isotopes decay as they travel through the ISM. Since radioactive isotopes

could only have travelled a finite distance before decaying, it sets a confinement time on cosmic rays in the Galaxy and thus they are known as clock isotopes.

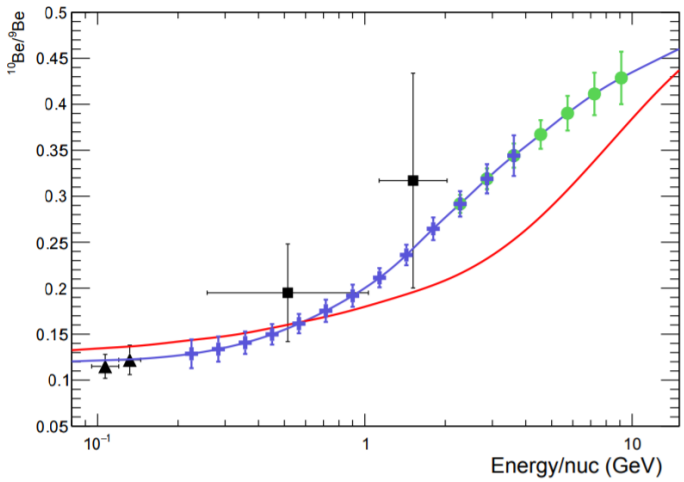

Figure 1–6: The ^{10}Be/^{9}Be ratio with data from ACE/CRIS [22] (triangles) and ISOMAX [23] (squares). The solid lines are the propagation models: the Leaky Box model with the Local Bubble (blue) [24] and a diffusive halo model (red) [25, 23]. The blue and green points are the HELIX predicted results for the first flight (7 days) and the second flight (28 days) respectively. Image Source: [26].

^{10}Be is an example of one of these clock isotopes that radioactively decays with a half-life of 1.39 Myr [27]. It is produced along with the stable ^{9}Be almost exclusively in spallation interactions. The ratio of a clock isotope to a stable isotope depends completely on the propagation of the cosmic rays and the length of time of their travel. Combined with the secondary-to-primary ratio B/C, ^{10}Be/^{9}Be can be used to distinguish between many different propagation models [28]. For a model like a diffusive halo, the combination of secondary-to-primary ratios and clock isotope ratios helps to determine the halo size and diffusion coefficient [29].

Fig. 1–6 is a plot of the predicted ^{10}Be/^{9}Be ratio as a function of energy for two propagation models. The black points are measurements from ACE/CRIS and ISOMAX and the coloured points are predictions for the HELIX experiment. It is apparent from this graph that ISOMAX has large uncertainties that make it difficult to distinguish between different propagation models. The HELIX experiment will be

attempting to produce high resolution results of the ^{10}Be/^{9}Be ratio at larger energies where there is better distinguishing power between propagation models.

1.6 Propagation Mechanisms

One of the major goals in cosmic-ray astrophysics is to understand the propagation mechanism of cosmic rays through the Galaxy. This section discusses some simple propagation models and the equations that define their diffusion and transport.

1.6.1 Leaky Box Model

The Leaky Box model [30] is the simplest image of cosmic-ray propagation. It assumes that the Galaxy is a flattened cylinder where the sources are distributed uniformly and axisymmetrically in the disk and the cosmic rays are confined to move within the halo, a larger concentric cylinder, as shown in Fig. 1–7 [20]. The halo has a total thickness $2H$ and radius R. In this model, the cosmic rays are initially accelerated in the Galactic plane. The particles propagate throughout the cylindrical halo interacting with different particles without additional acceleration [30]. When a particle reaches the boundary, it will typically reflect off and continue its movements within the halo. Every time that the particle reaches the boundary there is a small probability that it escapes, hence the name the Leaky Box model.

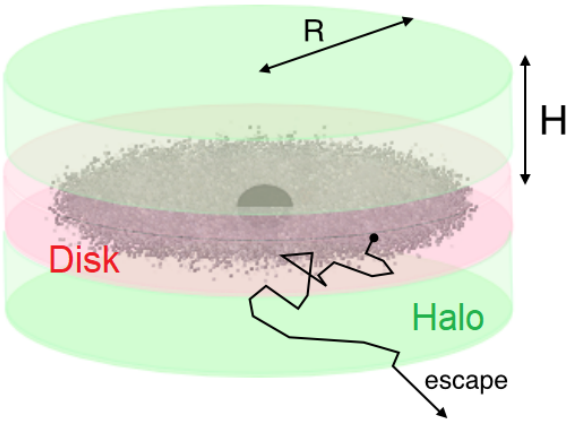

Figure 1–7: Diagram of the Leaky Box model. The cosmic rays are produced in the disk and propagate within the cylinder of the halo with a total height of $2H$ and a radius R. Image Source: [20].

The Galactic sources of cosmic rays should be concentrated in the Galactic plane where they are transported along magnetic field lines. The simplest case is with static field lines where charged particles will spiral around the lines, but generally the field

changes with time. The magnetic field also gets altered by these charged particles. Cosmic rays diffuse in this more complicated magnetic field environment [14].

The diffusion equation for cosmic rays is found by considering the continuity equation [14, 20] relating the differential density N, its flux $\vec{J}$ and the contribution of local source intensity Q by

$$\frac{\partial N}{\partial t} = -\nabla \cdot \vec{J} + Q \ . \tag{1.3}$$

These relate to Fick's first law of diffusion for an isotropic medium where the flux relates the number density and a diffusion coefficient D by $\vec{J} = -D\nabla N$ [14, 20]. The diffusion equation then becomes

$$\frac{\partial N}{\partial t} = \nabla \cdot (D\nabla N) + Q \ . \tag{1.4}$$

For the Leaky Box model there is no local source of cosmic rays in the wider halo so the Q term is not included. There is also a constant escape probability to simplify the equation for the density. Instead of a differential term, it can be expressed as a constant loss over time. This can be summarized for a specific species i as

$$\frac{\partial N_i}{\partial t} = \nabla \cdot (D\nabla N_i) = -\frac{N_i}{\tau_{esc}} \rightarrow N_i(t) \propto exp(-t/\tau_{esc}) \ . \tag{1.5}$$

This equation includes the escape time τ_{esc}. It is the mean time for a cosmic ray to escape the halo including time interacting with particles inside the halo [20]. These interactions make τ_{esc} much longer than a simple straight path to travel the distance H to the edge of the halo from the disk. The exponential part points to the probability that a particle is still in the halo after time t [14].

1.6.2 More Complex Models

The Leaky Box is one of the simplest models of cosmic-ray propagation. Many newer models addressed problems and limitations of the Leaky Box model to match observed data.

The local bubble is an extension to the steady-state solution for the Leaky Box model where, instead of assuming a uniform distribution of sources and material in the plane of the disk, there is a local low density bubble or hole where there are no sources of primary cosmic rays [24]. The Solar System is thought to currently be, or formerly have been, in a local bubble.

Some cosmic-ray experiments, like AMS-02, use a diffusive halo propagation model to interpret their data discussed in more detail in [29]. The Galaxy is still considered to be a flattened cylinder. The main takeaway from this model is that its solution is very dependent on the size of the halo to define the escape time. Secondary-to-primary ratios like B/C only weakly constrain the model and require measurements of unstable nuclei like ^{10}Be/^{9}Be to further constrain the model. Fig. 1–8 shows the predicted ^{10}Be/^{9}Be ratio for the diffusive halo model for different H compared to current measurements and models, as shown in Fig. 1–6.

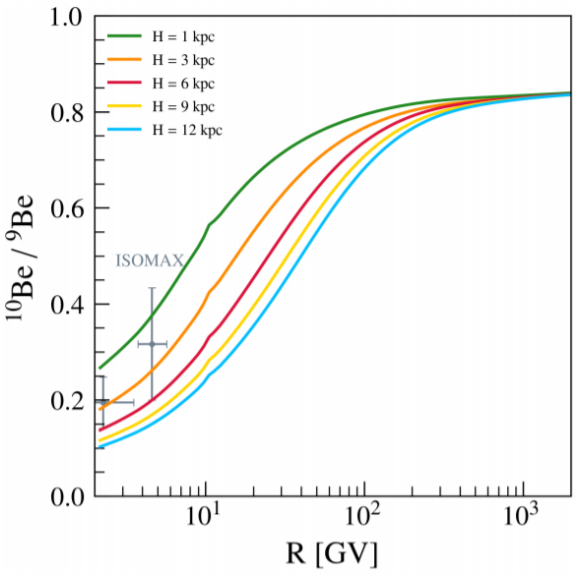

Figure 1–8: The prediction of the ^{10}Be/^{9}Be for the diffusive halo model for various halo half thicknesses H. Image Source: [29].

1.6.3 Transport Equation for Primary Cosmic Rays

The general cosmic-ray transport equation described by [14] is

$$\frac{N_i(E)}{\tau_{esc}(E)} = Q_i(E) - \left(\frac{\beta c\rho}{\lambda_i} + \frac{1}{\gamma\tau_i}\right) N_i(E) + \frac{\beta c\rho}{m_p} \sum_{k \geq i} \sigma_{k\to i} N_k(E), \tag{1.6}$$

where the subscript i denotes the secondary cosmic rays formed by the spallation of primary cosmic rays denoted with subscript k. N is the number density, $Q_i(E)$ is the local production rate, and λ_i is the interaction length of nuclei i in the Galaxy. The first term $Q_i(E)$ is the cosmic-ray production rate by a local source in the halo.

For the Leaky Box, $Q_i(E) = 0$. The term within the brackets relates to the loss of a nucleus from its interaction with the ISM and the decay of radioactive species produced in spallation with a Lorentz dilated lifetime of $\gamma\tau_i$. The final term has to do with the production of a secondary cosmic ray species from heavier nuclei.

For a given species, it may not be necessary to include all of the terms of Eq. 1.6. Consider stable primary cosmic rays where there is no production due to spallation and there is no decay. In this case, the transport equation simplifies to

$$N_p(E) = \frac{Q_P(E)\tau_{esc}(R)}{1 + \lambda_{esc}(R)/\lambda_P} \ , \tag{1.7}$$

where the terms now apply to a primary cosmic ray denoted by the subscript P [14]. The escape time and length are a function of the rigidity R, the resistance of a charged particle to bending in a magnetic field, to make it easier to compare different nuclei. Particles with the same rigidity behave the same in the magnetic field, but depending on the species, they will have different kinetic energy per nucleon.

Secondary cosmic rays are not produced and accelerated by a source so there is no $Q_i(E)$ term and the primary production method is from spallation. Some secondary particles are stable so they do not include the decay term. Other nuclei, like ^{10}Be, are unstable so the decay term is necessary.

1.7 HELIX Scientific Motivation

The HELIX experiment is designed to measure light isotopes during long-duration balloon flights. It includes a 1 Tesla superconducting magnet and a drift chamber tracker to measure the rigidity of cosmic particles. A time-of-flight system and ring-imaging Cherenkov detector measure their velocity. The energy for these experiments is usually expressed as the energy per nucleon, GeV/n, contained in the nucleus. HELIX is designed to measure light isotopes with charges up to Z=10 for energies ranging from 0.2 GeV/n to 10 GeV/n over two flights [28].

As shown in Fig. 1–6, ACE/CRIS measured ^{10}Be/^{9}Be up to 200 MeV/n [22] while ISOMAX made measurements up to 1-2 GeV/n [23]. The measurements by these experiments were limited to lower energies where the models behave similarly. Fig. 1–6 also shows that HELIX expects to be able to measure this ratio to high enough precision to distinguish between propagation models.

The primary scientific goals for the two stages of HELIX are given in Table 1–1. ^{10}Be/^{9}Be is the main measurement since it is vital for constraining propagation models and the instrument has been specially designed for this. The first stage will focus on ^{10}Be/^{9}Be ratio measurements up to 3 GeV/n to cover just beyond the energy range already covered by ACE/CRIS and ISOMAX. The second stage will increase the measurement range to 10 GeV/n.

Nuclei	**Energy [GeV/n]**
^{10}Be/^{9}Be	0.2 - 10
^{3}He/^{4}He	0.3 - 12
^{22}Ne/^{20}Ne	>1
^{7}Li/^{6}Li	>1
^{10}B/^{11}B	>1

Table 1–1: Primary scientific goals of HELIX [31].

With the high-resolution required to make those measurements and the energy range of interest, HELIX offers the ability to measure other isotope ratios. HELIX will measure the ratios of ^{10}Be/^{9}Be, ^{22}Ne/^{20}Ne, ^{7}Li/^{6}Li, ^{10}B/^{11}B at the highest energies to date [31]. These measurements are intended to complement the results of other cosmic-ray experiments to provide a clearer view of the cosmic-ray propagation mechanism.

Some secondary goals of HELIX include the first measurements of ^{15}N/^{14}N, ^{18}O/^{16}O and ^{13}C/^{12}C above 1 GeV/n. There will be additional measurements of B/C and ^{2}H/^{4}He as well as an attempt to measure ^{14}C/^{12}C. Primary H and He will be measured up to 125 GeV/n [31].

CHAPTER 2
High Energy Light Isotope Experiment (HELIX)

This chapter serves as an introduction to the HELIX experiment, including background information about balloon-borne experiments and the reasoning for the HELIX design. It also includes descriptions of the different detector components and the aerogel fabrication process for the ring-imaging Cherenkov detector.

2.1 Overview of Balloon-Borne Experiments

HELIX is a balloon-borne detector to measure the energy spectra of light nuclei in cosmic rays. The experiment is designed to be carried via a balloon to an altitude of 40 km where the interaction depth is $\sim$ 28.3 kg/m^2. This means that the balloon is above over 99 % of the atmosphere. At this altitude, the primary cosmic rays will interact directly with the detector system before entering the bulk of the atmosphere and producing particle showers. The HELIX scientific program includes at least two balloon flights, the first of which will measure the cosmic-ray energy spectrum up to 3 GeV/n during its initial seven day flight. The first flight data acquisition is limited to about 7 days due to the limited amount of liquid helium on board to cool the superconducting magnet. The first flight is currently scheduled for the 2021/2022 austral summer NASA Antarctic Balloon Campaign out of McMurdo Station. The second flight will include an upgraded system to measure cosmic rays up to 10 GeV/n in a 28 day flight.

Figure 2–1: Partially filled balloon prepared to carry the STO-II payload during the 2016 balloon campaign. Image Source: [32].

The project will use a 1.13×10^6 m^3 zero-pressure balloon partially filled with helium during launch, as shown in Fig. 2–1. The balloon expands to the full volume around the desired float altitude as the pressure outside of the balloon decreases. This helium provides the lift while it is ascending [33].

During the austral summer, the station receives 24-hour daylight that is useful for balloon experiments. The payloads are all solar powered and so the constant daylight keeps the project electronics functioning. The constant light makes it easier for balloons to maintain a constant altitude and have longer flights. This is because a day/night cycle heats and expands the balloon gas during the day, lifting the balloon and then at night the gas condenses and lowers the balloon. The Antarctic austral summer also produces a stratospheric anticyclone that provides a circular flight path around the South Pole over the Antarctic continent [32]. When the balloon runs out of helium, the payload is disconnected by an operator on the ground and it descends using an attached parachute. The combination of the vast, isolated location with effectively no electronic interference and constant daylight makes it an ideal place for medium to long duration balloon flights.

2.2 Detector Background Information

This section is meant to introduce the physical motivation for the detector design so that HELIX is capable of making high precision measurements of multiple light isotopes in cosmic rays.

2.2.1 Measurement Goals

The HELIX instrument is designed to hold multiple detection systems to measure cosmic-ray properties such as the charge, rigidity and velocity in order to identify the nuclei that pass through the system. The instrument consists of four main components: a 1 T superconducting magnet and a drift chamber tracker (DCT) to measure the rigidity, as well as a time-of-flight (TOF) system and a ring-imaging Cherenkov (RICH) detector to measure the velocity. The charge Z is measured by

analyzing the pulse height from the TOF scintillator bars, which scales as Z^2. The particle mass, velocity and momentum are related by

$$p = \beta\gamma mc. \tag{2.1}$$

The momentum of a particle is determined by how much a particle track bends in a magnetic field. For HELIX, this is measured with a 1 T superconducting magnet and a DCT. The trajectory of a non-relativistic charged particle travelling in a perpendicular magnetic field should bend in a circular path with the Larmor radius given by $qvB = (mv^2)/r_L$. This can also be written in a form better suited for relativistic particles, $r_L = p/(ZeB)$, where r_L is the Larmor radius, p is the particle momentum, B is the magnetic field strength and Z is the charge [20]. This Larmor radius is often converted to a rigidity R in Volts. The rigidity quantifies the resistance of a charged particle to being deflected by a magnetic field according to

$$R \equiv r_L Bc = \frac{pc}{Ze}. \tag{2.2}$$

Combining Eq. 2.1 and Eq. 2.2, the mass of the particle can be calculated using the measurements of the charge, rigidity and β by

$$mc^2 = \frac{ZeR}{\gamma\beta} = ZeR\frac{\sqrt{1-\beta^2}}{\beta}, \tag{2.3}$$

where the energy is often presented in terms of the energy per nucleon GeV/n.

The velocity of the particle can be measured in multiple ways. For lower energy particles, the simplest method is a TOF system consisting of at least two detection planes placed at a fixed distance apart. The amount of time it takes for the first system to trigger, travel that distance and then trigger the second system should give a measurement of β. This technique is used to measure β for particles up to approximately 1 GeV/n. At higher energies, a RICH measures the velocity. A charged particle travelling through a transparent radiator medium faster than

the speed of light in the medium will emit coherent radiation in a cone known as Cherenkov radiation (see Appendix A). A RICH consists of the radiator plane where the Cherenkov photons are emitted from and a detection plane covered with photosensors, such as silicon photomultipliers (SiPMs), that detect these photons at a fixed distance from the radiator. The Cherenkov cone is detected as a ring on this plane. Information on the radius of that ring, the distance between the radiator plane and the detection plane and the radiator thickness are used to calculate the Cherenkov opening angle θ_c. The radiator refractive index n, the velocity β and θ_c are related by

$$\cos\theta_c = \frac{1}{n\beta}, \tag{2.4}$$

where particles with a higher β will produce a larger Cherenkov ring. Thus the velocity of the particle has a direct effect on the Cherenkov ring radius.

2.2.2 Expected Resolution

With measurements of the mass and the charge, it is possible to identify the specific isotopes and produce mass histograms like Fig. 2–2. The width of the peaks depends on the precision of the charge, rigidity and velocity measurements. One of the principal goals of HELIX is to measure the mass with high precision to achieve a four-sigma mass separation between the isotope peaks for ^{10}Be and ^{9}Be [27]. According to the simulation summarized in Fig. 2–2, this four-sigma separation should be possible with a mass resolution $\Delta m/m = 2.5$ % at 3 GeV/n. It would be difficult to distinguish the two isotopes at $\Delta m/m = 10$ %.

The mass resolution is calculated according to

$$\left(\frac{\Delta m}{m}\right)^2 = \left(\frac{\Delta R}{R}\right)^2 + \left(\gamma^2 \frac{\Delta\beta}{\beta}\right)^2, \tag{2.5}$$

where R is the rigidity as measured using the magnet and the DCT and β is the velocity as measured with the TOF system and the RICH.

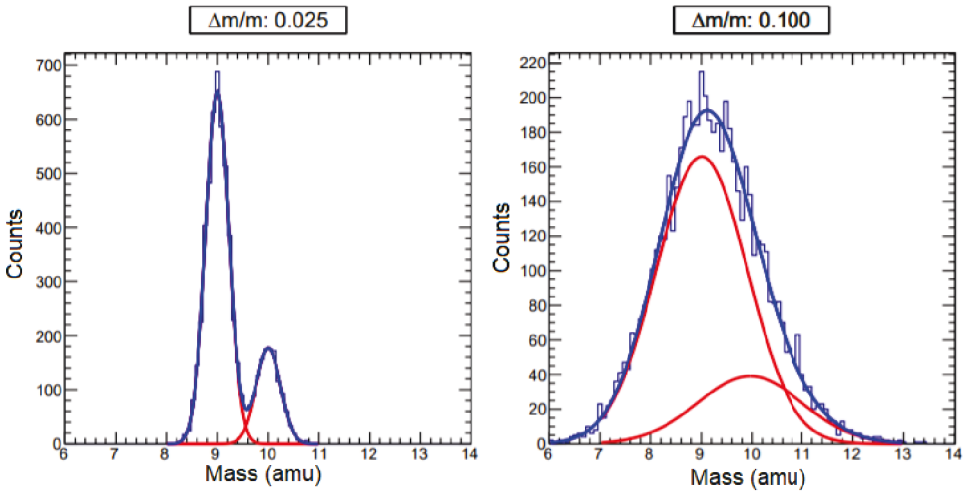

Figure 2–2: Comparison between an instrument with 2.5 % mass resolution (left) and one with 10 % resolution (right) to distinguish a ^{10}Be peak from a ^{9}Be peak. The blue curve is the 'measured' mass spectrum in the simulation and the red curves are the individual isotopic contributions assuming ^{10}Be/^{9}Be = 0.3. Image Source: [26].

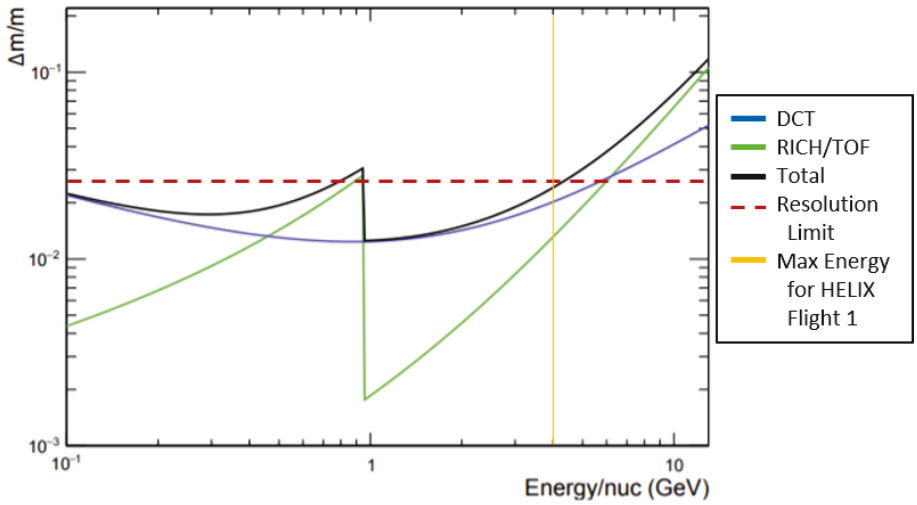

Figure 2–3: The mass resolution of the different HELIX components. The black curve is the quadrature sum of the RICH/TOF and DCT contributions according to Eq. 2.5. The mass resolution goal for HELIX (dashed line) shows that for essentially all cosmic rays with E≤3 GeV/n (orange line), the measurements should be close to or within the 2.5 % mass resolution. Image Source: [26].

The 2.5 % total mass resolution 'budget' for this experiment is split evenly between the rigidity and velocity measurements $\Delta R/R = \gamma^2 \ \Delta\beta/\beta \ \approx 1.8$ %. For 3 GeV/n, this works out to $\Delta\beta/\beta \ \sim 1$ % [27]. For the RICH, the resolution is split

evenly along the θ and n components of Eq. 2.4 according to

$$\left(\frac{\Delta\beta}{\beta}\right)^2 = \left(\frac{\Delta n}{n}\right)^2 + (\Delta\theta\tan\theta)^2 . \tag{2.6}$$

This results in $\Delta n/n = \Delta\theta\ \tan\theta \approx 0.07$ %. Considering the other limitations of the detector, the refractive index of the aerogel RICH radiator must be known to within $\Delta n/n = 0.07$ % to get the velocity resolution necessary for the RICH detector.

Fig. 2–3 shows the contributions of the rigidity and velocity measurements and their combination to the total mass resolution as a function of particle energy according to Eq. 2.5. The rigidity is measured by a single instrument, which is limited by the resolution of the particle tracking system. Up to 1 GeV/n, the TOF measures β, but above that energy the uncertainty gets too large for the resolution allowance so the RICH becomes the principal β detector. In Fig. 2–3, the sudden drop in the TOF/RICH line at 1 GeV/n is due to switching from the TOF to the RICH detector.

2.3 HELIX Detector Components

The HELIX detector is composed of four main instruments: the 1 Tesla superconducting magnet and the DCT to measure the rigidity, and the TOF and RICH detectors to measure the velocity, as shown in Fig. 2–4. These components will be explained in the following section.

2.3.1 Superconducting Magnet

The central part of HELIX is occupied by a 1 T superconducting magnet built by Cryomagnetics Incorporated and previously used by the High-Energy Antimatter Telescope (HEAT) [34] for its five flights starting in 1994. HEAT measured the positron fraction ($e^+/(e^+ + e^-)$) and antiproton-proton fraction ($\bar{p}/p$) in cosmic rays. The magnet is sitting in a 260 L cryostat filled with liquid helium (LHe) to cool it below the 9.8 K critical temperature [28, 27]. The LHe is expected to last seven days. The magnet system previously functioned in an external pressure vessel. With the HELIX upgrade to the system, it now functions at the low atmospheric pressure

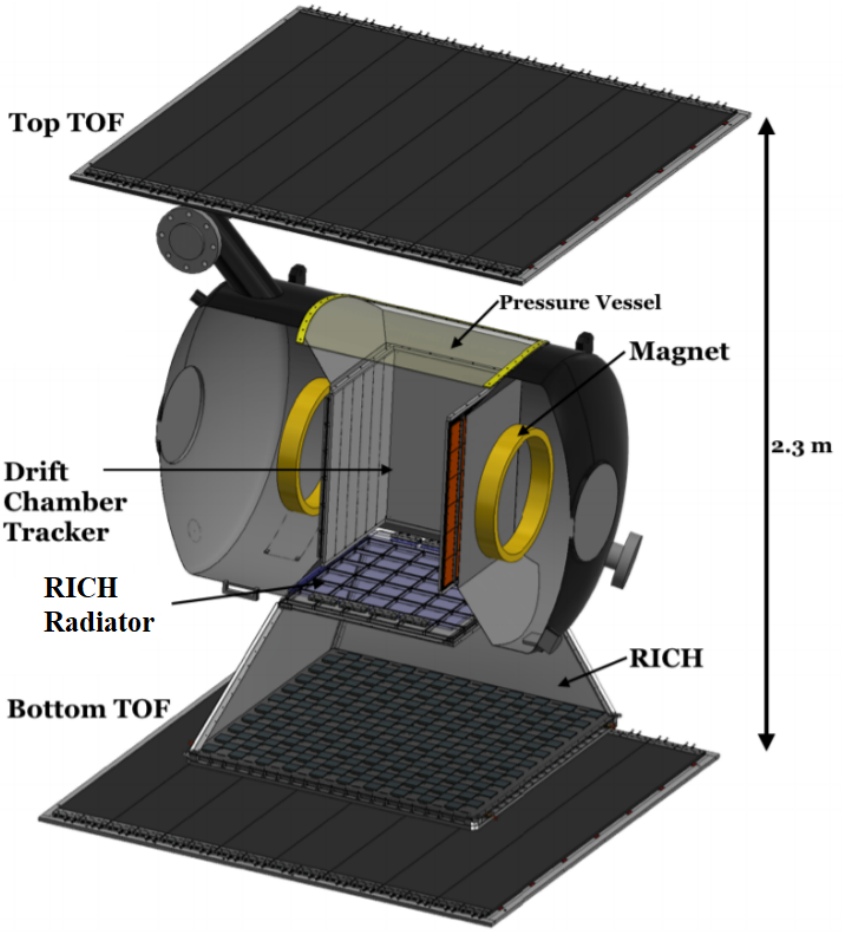

Figure 2–4: The HELIX detector labelled with all of the major components. The gold coloured rings are the superconducting magnet coils and the DCT sits between the coils in a pressurized vessel. The scintillator bore paddle is not shown in this image, but it is located between the bottom of the DCT and the RICH radiator. Image Source: [27].

experienced during flight when the balloon is at 40 km altitude. The magnetic field has been mapped within the rectangular warm bore that measures $0.51 \times 0.51 \times 0.61$ m^3 [26]. The DCT sits within this rectangular bore, as seen in Fig. 2–4 [26].

2.3.2 Drift Chamber Tracker

The DCT tracks cosmic-ray nuclei that are deflected in the magnetic field from the superconducting magnet. The purpose of the DCT is to measure the rigidity of the particle passing through it, according to Eq. 2.2. The DCT fills the bore with a multi-wire flat-geometry drift chamber. The DCT is housed in a pressure

vessel so it can run at 1 atm, but the magnet could run at the local atmospheric pressure. The DCT consists of 72 sense layers each with three drift cells. Each fills $0.45\times0.45\times0.58$ m^3 of the pressure vessel [28, 27]. The tracker uses CO_2 as it is a low diffusion drift gas. Combined with the $\sim$100 kV/m drift field and the high sampling rate electronics, it is possible to achieve a spatial resolution of 65 μm for Z$>$3 cosmic rays [26, 27].

2.3.3 Time-of-Flight

The TOF system is designed to measure the velocity for particles with $E \leq$ 1 GeV/n as they pass through the different detector layers and to measure the charge using scintillation light. There are three layers of the TOF system: the top layer, bottom layer and bore paddle. The top and bottom TOF are separated by 2.3 m where each layer consists of eight 0.2×1.6 m^2 scintillator paddles that are 10 mm thick [26] covering a total area of 1.6×1.6 m^2. Each paddle is read out with 16 SiPMs, 8 at each end [27]. The signals from the SiPMs are digitized with 10 ps time-to-digital converters that should achieve a timing resolution for the entire system to less than 50 ps for cosmic rays with Z$>$3 [28]. The timing resolution of the system is dependent on the type and geometry of the scintillator and the electronics. This includes the time for photons produced to reach the SiPMs and pass a discriminator threshold on all of the TOF scintillator layers in the detector.

Particles traversing all of the layers of the TOF system trigger the data acquisition. The transit time between the paddles can be used to estimate the velocity, however, as the energy increases the velocities approach the speed of light c. For energies above 1 GeV/n, the time difference for two particles with different masses, such as ^{9}Be and ^{10}Be, measured over the 2.3 m separation, is within the 50 ps timing resolution of the TOF system. So it cannot be used to distinguish the particles. Therefore, at higher energies, the RICH system is used to make velocity measurements.

There is a bore paddle located between the DCT and the RICH radiator plane. It is a 0.6×0.6 m^2 scintillator paddle that is read out with 32 SiPMs total, 16 on each end [27]. This bore paddle requires the particles to pass through the RICH radiator layer. The three layers of scintillator paddles measure to charge up to Z=10.

2.3.4 Ring-Imaging Cherenkov Detector

The HELIX RICH is used to make velocity measurements for cosmic rays with E>1 GeV/n, up to about 3 GeV/n for the first detector flight [28]. An explanation of the physics of the Cherenkov effect is included in Appendix A. The RICH consists of a radiator plane and a SiPM detection array, as shown in Fig. 2–5. It is designed as a proximity focused Cherenkov detector so that it is compact, but able to produce the high-resolution measurements necessary to distinguish different isotopes [35].

The radiator plane is comprised of a square array of 36 radiator tiles covering an area of 0.6×0.6 m^2. This includes an NaF tile in each of the corners of the plane. NaF has a well measured spectrum with wavelength with an average refractive index of $n = 1.33$ so it will be used for in flight calibration of the RICH detector. The remaining 32 tiles are aerogel tiles with $n \approx 1.15 - 1.16$. This refractive index was chosen so that the velocity threshold ($\beta \geq 0.87$, $E \geq 1.03$ GeV/n) overlaps with the upper end of the TOF capabilities ($\approx$ 1 GeV/n). Both the aerogel and NaF tiles are approximately 100×100×10 mm^3 with flattened and angled corners to fit into aluminum frames.

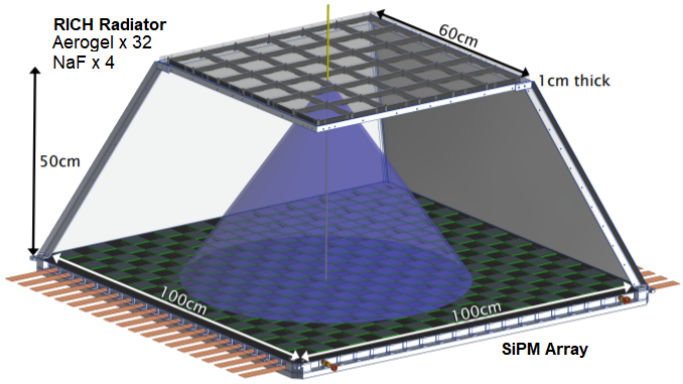

Figure 2–5: A diagram of the HELIX RICH detector including the aerogel and NaF radiator plane and the SiPM array. The yellow track is a possible Be track through the RICH detector and the blue cone is the resulting Cherenkov cone. Image Source: [35].

There is a 0.5 m expansion length between the radiator and the SiPM detection plane. The SiPM array is populated in a checkerboard pattern to save costs while still sampling the Cherenkov ring enough to meet the velocity resolution requirements. The SiPMs are 6×6 mm^2 Hamamatsu pixels arranged in 8×8 pixel arrays. The SiPM array is made of 200 pixel arrays of 64 pixels each which results in a total of 12800 SiPM channels [35]. 8 SiPM arrays are read out on a board consisting of 16 CITIROC1A [36], which have a timing resolution of 100 ps and single photoelectron charge resolution. The SiPMs were chosen because of their insensitivity to the magnetic field that is found in the region of the detector plane and because of their superior spatial resolution. For these reasons, SiPMs are a better choice than conventional photomultiplier tubes. The SiPM plane is maintained at 0° C to reduce the background from temperature-dependent dark current [35].

2.4 Aerogel Manufacturing and Properties

The principal focus of the thesis research was on the RICH aerogel and its refractive index variations. It is important to understand how the aerogel is produced and some properties to motivate that work. HELIX's aerogel was made by Makoto Tabata, a HELIX collaborator at Chiba University, Japan.

2.4.1 Aerogel Production

Aerogel was first used in physics experiments in the 1970s to fill the gap in the refractive index between gases and liquids/solids for producing Cherenkov light in a transparent material. Aerogel is a synthesized solid silica-based material that is highly porous, with silica and air structures on the order of 10 nm [37]. Silica aerogels are a class of materials with a wide range of refractive index, transparency and density that can be tuned to suit an experiment's requirements. It has a styrofoam-like texture, but it is extremely brittle and prone to cracking and surface deformations if it is not handled properly. Aerogel tiles have been produced with refractive indices just above 1 up to 1.3 [37].

Conventional aerogel fabrication methods are capable of producing extremely high transparency, low refractive index tiles that are either hydrophilic or hydrophobic and suitable for many experiments. If hydrophilic aerogel is exposed to moisture, it will become opaque and dissolve. It could be used for projects where it is sealed from moisture, but that is not practical for a balloon experiment. Hydrophobic aerogel is treated with a reagent that replaces the hydroxyl groups on the surface of SiO_2 with a hydrophobic group during drying so it will not react with water [38]. HELIX uses hydrophobic aerogel because it is not sealed and if water did reach the tile it would lose the transparency that the RICH detector depends on.

Based on the 1-3 GeV/n energy range of interest for the HELIX RICH, the geometry constraints in the RICH detector and the range already covered by the TOF, the RICH will use ultrahigh refractive index hydrophobic aerogel tiles with $n \approx$1.15-1.16. Tiles with these properties are difficult to fabricate with conventional methods due to cracking. Dr. Tabata uses a novel pinhole drying technique to make the tiles.

2.4.2 Fabricating the Aerogel

The aerogel starts its fabrication as a wet-gel that is synthesized with a silica precursor, water, a solvent such as methanol or N,N-dimethylformamide [37], and catalysts, whose ratios are tweaked depending on the desired ending refractive index [39]. The gel is then left to dry for an hour in a mold so it solidifies enough to be transferred to a pinhole drying container.

The pinhole drying container is a semi-sealed container where the wet-gel sits on a sieve with a glass lid. The lid has a series of pinholes with tape on top that is removed to control the drying rate as seen in Fig. 2–6. This fabrication method allows the wet-gel to dry uniformly and slowly and produces a high-density aerogel without any cracks. The mass of the wet-gel is measured every day until it reaches 65 % of its initial mass after about 70 days of drying [39].

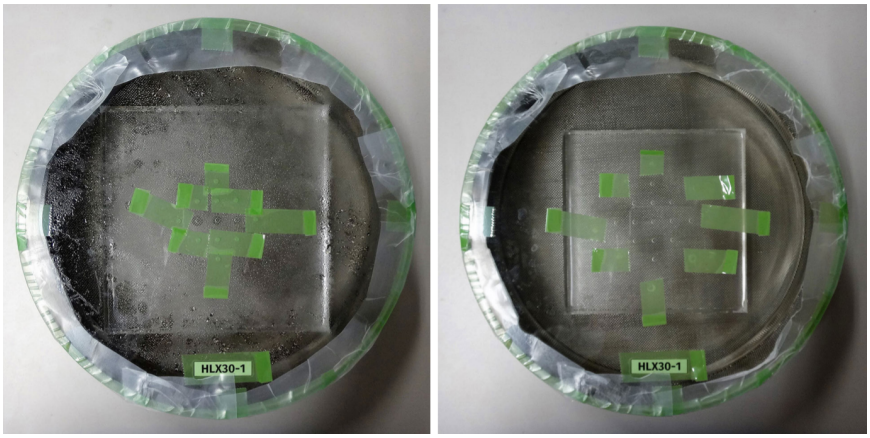

Figure 2–6: The pinhole drying process for an aerogel tile with the wet-gel sealed in the container with most holes closed on the left and then the same tile after drying with most holes opened. The tile shrinks as it dries. Image Source: [39].

After the pinhole drying, the wet-gel is put into a bath of ethanol along with the hydrophobic reagent silazane to exchange the initial solvent and to make the tile hydrophobic [37, 39]. Then the aerogel is subjected to supercritical drying by liquid CO_2 for approximately a week [40]. This process extracts the ethanol and replaces it with air. A photograph of a finished aerogel tile is shown in Fig. 2–7.

2.4.3 Aerogel Properties

The aerogel produced using this method has a final density of around 530 kg/m^3 with an estimated refractive index between n=1.15 and n=1.16 [40]. The refractive index is proportional to its density so a higher density aerogel will have a larger refractive index.

After the tiles are completed, they are subjected to several tests to determine if they are suitable for HELIX. The first test is a visual check to see if there are any major deformations or cracks. Of the 96 tiles produced for HELIX, 74 did not have cracks [39]. The transmittance is measured, using a Hitachi spectrophotometer, between 200 nm and 800 nm [38]. On average, the aerogel has a transmittance of about 73 % at 400 nm [39]. A preliminary refractive index measurement is completed for each tile using a laser deviation method. This method involves measuring the deviation of a 405 nm laser beam passing through a corner of the aerogel [38]. The

method to do this is described in great detail in [38]. Fig. 2–8 is summary of the transmittance and refractive index for each of the 96 aerogel tiles produced. The refractive index measurement for each point in Fig. 2–8 is the average measurement from the laser deviation in the four corners of a single aerogel tile, which was then repeated for all 96 aerogel tiles.

To get the required RICH resolution for HELIX, the refractive index must be known over the whole aerogel face, not just in the corner. Another method is required to measure refractive index variations across the aerogel tiles.

Figure 2–7: A picture of a flight quality aerogel tiles in its frame. Image Source: [39].

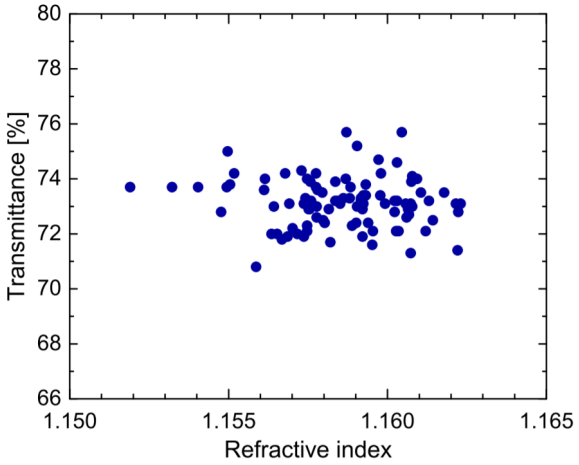

Figure 2–8: Transmittance and refractive index from the corners of an uncut aerogel tile. The measurements shown are from the 96 aerogel tiles produced for HELIX. Image Source: [39].

The aerogel tiles are initially 120×120 mm^2 and 10 mm thick. If the tiles pass the initial tests, the edges are water-jet cut to 100×100 mm^2 to fit the aluminum frames shown in Fig. 2–7. The full RICH radiator includes 32 aerogel tiles and 4 NaF tiles as mentioned previously. Of the 96 tiles produced, at least 32 of them must be considered flight quality. This means that they have no blemishes and are within the requirements for the refractive index, transmittance and thickness. Fifty aerogel tiles with these properties were marked as flight quality tiles and sent to McGill for full refractive index scans. This will ensure that there are backup tiles for the array.

CHAPTER 3
Aerogel Calibration System

This chapter is a description of the various components of the aerogel calibration system. It is designed to measure the Cherenkov cone opening angle as a charged particle of fixed energy from a linear accelerator passes through a HELIX RICH aerogel tile. The principal research focus of the author for this project was in all aspects of the development and operation of the calibration system.

3.1 Aerogel Calibration Background

This section presents the motivation for measuring the refractive index of aerogel tiles including an explanation of past techniques from other experiments to do this task. It explains the approach taken by HELIX to make these measurements.

3.1.1 Motivation for Aerogel Calibration

In the HELIX RICH, and other experiments that image Cherenkov rings, a charged particle with sufficient energy will pass through the radiating medium and produce a Cherenkov cone. This cone is detected on a plane at a fixed distance away as a ring. The radius of this ring gets larger with increasing velocity, so by measuring the radius, it is possible to determine the particle's velocity β. This interaction obeys Eq. 2.4, which relates the refractive index n and particle velocity β to the Cherenkov cone opening angle θ_c. During measurements with these types of systems, n is known and θ_c can be calculated. Determining θ_c requires information about the radiator geometry, the distance between the radiator and the detector and the measurement of the Cherenkov ring radius. Then it is straightforward to calculate β and hence the energy of the particle according to

$$\beta = \sqrt{1 - \left(\frac{mc^2}{E}\right)^2}\,, \tag{3.1}$$

that compares the rest energy and the total energy of the particle. This task becomes more difficult when the particles do not enter perpendicular to the radiator face as

that produces an ellipse of Cherenkov photons. That shape must be accounted for in order to determine β accurately.

However, all of these calculations are based on the assumption that the refractive index of the radiating medium is known precisely and that the faces are flat and parallel. In homogeneous materials that have flat parallel faces, like pure NaF crystals, the Cherenkov ring only needs to be measured at a single location since the refractive index should be constant throughout the material. This is difficult for aerogel where each tile has variations in the refractive index due to the fabrication. This necessitates having a way of making high precision refractive index measurements across all tiles.

The approach for the aerogel refractive index calibration measurements used in this experiment is to rearrange Eq. 2.4 such that the particles of fixed energy go through the aerogel perpendicular to the surface. In that scenario, the Cherenkov ring should be circular and, with all other variables fixed, the change in the radius measured should be solely due to the refractive index change. By this method, the setup of the calibration system is fairly similar to the RICH structure, but allows for a high precision measurement of the refractive index.

3.1.2 Cherenkov Ring Measurement Geometry

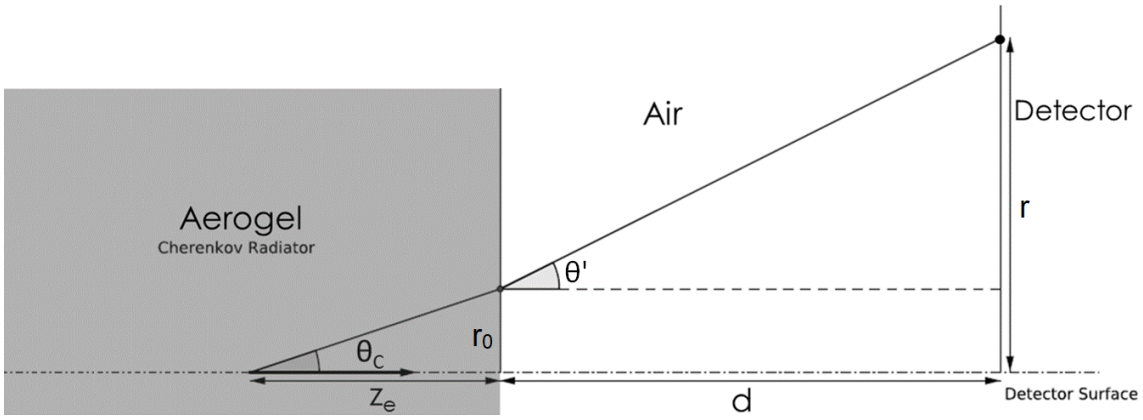

Figure 3–1: Diagram modified from [41] showing the geometry of the Cherenkov photon path through aerogel. r is the Cherenkov ring radius, z_e is usually half the aerogel thickness, d is the distance from the aerogel surface to the detection plane. The other parameters do not appear in the final equation of measured variables, Eq. 3.2, but are involved in the derivation.

At the interface between the exit face of the aerogel and the air, as shown in Fig. 3–1, there is an additional refraction of the Cherenkov photons due to the different refractive indices of the the two media. Cherenkov photons should be emitted equally throughout the ∼10 mm aerogel thickness so the average emission point z_e is just quoted as half of the aerogel tile thickness z_e ∼5 mm.

To account for this extra refraction there is an equation that uses the variables shown in Fig. 3–1 to relate the measurable quantities of the system, the ring radius r, the half-thickness z_e and the aerogel-CCD distance d, to the desired output, the Cherenkov cone opening angle θ_c. It requires additional input of the refractive index of air, n_0 - 1 = 3×10^{-4} [42], and the velocity of the charged particle. The main equation used for the analysis, based on Fig. 3–1, is

$$\tan\theta_c = n_0\beta\left(\frac{r - z_e\tan\theta_c}{\sqrt{(r - z_e\tan\theta_c)^2 + d^2}}\right) , \tag{3.2}$$

which is solved numerically using a function like Python's *scipy.optimize.fsolve*. θ_c is related to n and β by Eq. 2.4. In a calibration setting, β is fixed to extract n. During HELIX flight data analysis, β is calculated by a measurement of θ_c and n as measured with the described calibration system. The focus of McGill's HELIX research was to build a calibration system following the convention in Fig. 3–1 using a 35 MeV linear accelerator (linac). This linac provides a narrow beam of ultra-relativistic electrons to measure the refractive index variations across the aerogel tiles.

3.1.3 Measuring the Cherenkov Ring

Overall, it is important to have accurate measurements of r, d and z_e in order to accurately calculate the index n. However, this is an ideal model where the beam is coming in perpendicular to an aerogel tile with uniform n and z_e. If the beam interacts with the aerogel at an angle or z_e, d or r are not all correct, then this will introduce systematic uncertainties in the calculation of the refractive index.

The aerogel tiles for the HELIX experiment are expected to be between $n = 1.15$ and $n = 1.16$. For this reason, the index is typically set to 1.155 for calculations and simulations. The electron beam for the calibration experiment described in this work has an energy of 35 MeV resulting in $\beta \approx 1$. For a $n = 1.155$ medium with a 35 MeV electron beam, the Cherenkov cone opening angle $\theta_c = 30.0°$ by Eq. 2.4. If $n = 1.15$, $\theta_c = 29.6°$. While running the system, the distance d in Fig. 3–1 is typically between 274 - 280 mm according to the distance calibration procedure described in Appendix B. According to Eq. 3.2, with the aerogel tile half-thickness $z_e = 5$ mm and $d = 278$ mm, increasing n from 1.15 to 1.155 increases the Cherenkov ring radius on the detection plane by over 5 mm.

3.1.4 Previous Aerogel Calibration Experiments

LHCb, AMS-02 and CREAM required refractive index measurements of their aerogel tiles. LHCb [43] is an experiment on the CERN LHC to measure the decay of B mesons. The LHCb RICH consists of two separate detectors: one with $n = 1.03$ aerogel [44] and C_4H_{10} gas and the other with CF_4 [43]. AMS-02 [45] is an antimatter and cosmic-ray nuclei experiment mounted to the ISS where the RICH radiator plane includes an inner region of NaF tiles surrounded by $n = 1.05$ aerogel. The RICH measures the particle charge and velocity. The CREAM experiment was a balloon-borne experiment to measure the flux of cosmic-ray nuclei [46]. The CREAM CHERenkov CAMera (CHERCAM) system used $n = 1.05$ aerogel for their particle charge measurements. It could not measure velocity as γ of the particles are high so $\beta = 1$ and the Cherenkov ring radius does not change [47].

There are several methods that were employed to make the refractive index measurements for these projects. These methods can be divided into two categories: those using lasers and those with charged particle beams.

The laser methods measure deviations of a laser beam as it passes through a tile to either measure the absolute or relative refractive index at a specific wavelength.

In the so-called gradient method, if there is an index gradient perpendicular to the beam direction, the beam will deviate from the path it would take without a gradient [47]. For the rotation method, the refractive index is determined by measuring the deviation of the laser beam while the aerogel is at different angles with respect to the beam direction. The gradient and rotation methods were used to measure the refractive index for the HELIX project by Thomas Rosin [48]. These methods all require corrections for surface profiles and for thickness of the tiles and this introduces sources of systematic errors.

LHCb developed a method that involved the 500 MeV electron beam of the DAΦNE Beam Test Facility in Frascati, Italy and the Aerogel Photographic Analysis by CHerenkov Emission (APACHE) imaging system [44]. AMS and CREAM subsequently tested the use of this method for their calibration. The electron beam passes through the aerogel, creating a Cherenkov ring of photons that are recorded on a photographic plate. The ring size is reduced using a focusing system based on a spherical mirror. The Cherenkov ring properties are calculated by precise image analysis of the photographic plates. The main limitation is that this method is time consuming, taking three days to fully analyze two AMS-02 or CREAM aerogel tiles that are approximately $115 \times 115 \times 25$ mm^3 [45, 47]. This method was used for LHCb, although it was ultimately not used for the complete study of the aerogel tiles for AMS-02 [44].

3.1.5 Challenges in Measuring the Aerogel Refractive Index

There is no standard method of determining n of aerogel, as the choice of analysis method depends on the requirements of the specific project. Many methods rely on strict geometric assumptions such as that the faces of the aerogel are flat and that all adjacent edges are perpendicular, for their optics arguments to work. The gradient method relies on neighbouring measurements to calculate a relative refractive index

change. It also requires fine measurements of the aerogel properties like surface features and thickness.

The beam method most closely resembles what happens in a RICH detector, with a charged particle creating a Cherenkov ring, but analyzing the photographic plate takes too long to be reasonable for large scale experiments. One option is to use a charge coupled device (CCD) camera and scan on a detection plane at a fixed distance from the aerogel, but this would still take quite a long time for a single point on the aerogel tile. The method used by HELIX has the same general premise as this beam test, but focuses on a more efficient detection method.

3.1.6 Method Adopted for Calibration

One of the methods adopted by HELIX for the refractive index measurements is based on using an electron beam. With a fixed beam energy, the changes in the aerogel refractive index should alter the Cherenkov ring radius measured on a detection plane. HELIX does not use photographic plates on its detection plane, like LHCb in their beam method, to map the entire Cherenkov ring. HELIX opts instead to sample the radial profile of the Cherenkov ring and identify the ring radius based on the position of the Cherenkov profile peak. This sampling technique was initially proposed by Ian Wisher, a HELIX collaborator from the University of Chicago, as a way of saving on the cost and time of the calibration procedure compared to photographic plates or a full two-dimensional CCD array.

This method is based on the simplified design in Fig. 3–1 with the aerogel faces and the detection plane placed perpendicular to the beam direction. The velocity of the particle β dictates the Cherenkov cone opening angle θ_c. A fixed distance d away, the Cherenkov photons are recorded on a detection plane. The detection board features sixteen linear CCD photosensors placed radially from the centre of the detection board to sample the Cherenkov ring. The CCDs are positioned such that the centre of each CCD is at a 200 mm radius from the board centre. The board

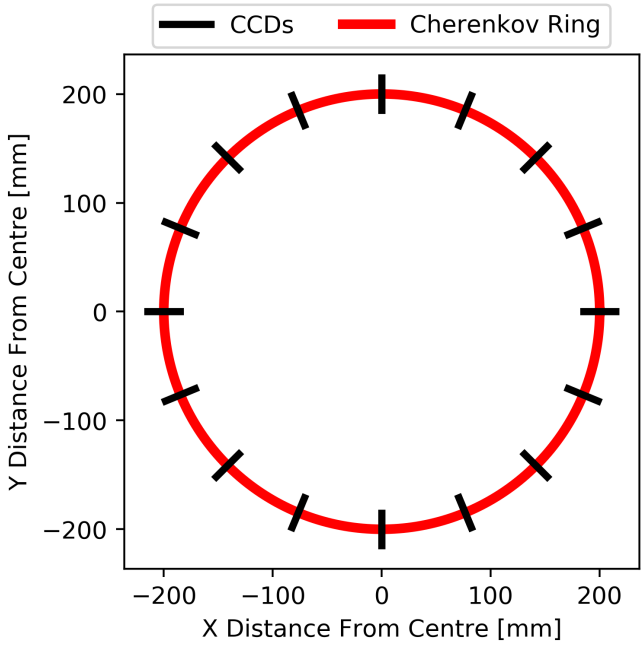

Figure 3–2: A diagram of the detection board for the aerogel calibration system. The black lines are the positions of the CCDs on the board centred at a 200 mm radius. It shows that if the board is placed at a distance where the resulting Cherenkov ring radius is roughly 200 mm, then the Cherenkov ring (red) will pass through the centre of all of the CCDs.

is placed at a specific distance from the aerogel where the radius of the Cherenkov ring on the board is approximately 200 mm. Fig. 3–2 shows an example of a 200 mm radius Cherenkov ring centred with the system where the ring passes through the middle of every CCD. These CCDs will record the radial profile of the Cherenkov ring during the calibration procedure. In the analysis, these profiles will be fit to find the peak of the distribution. The position of those peaks on the board will be used to fit a circle to determine the Cherenkov ring radius. This radius is used to determine the refractive index n according to Eq. 3.2.

The final detector design of this aerogel calibration system is the focus of the remainder of this chapter. Subsequent chapters will focus on analyzing the data to produce index maps of aerogel tiles and an exploration of the tolerances associated with the system's measurements.

3.1.7 Requirements

HELIX's electron beam method has certain requirements to make it a feasible way of measuring the refractive index. Each of the sixteen CCDs consists of 3694 pixels that are 8 μm long and 200 μm wide arranged in a single pixel wide line. This results in CCDs that are 200 μm wide and 29.552 mm long total. With an expected ring diameter of 200 mm, the CCDs cover a very small fraction of the detection board area, as shown in Fig. 3–2. The beam must run at high enough current so that it produces a sufficient number of photons to produce a significant CCD signal. This method also requires a well focused narrow beam so that it only probes a small region of the aerogel at a time. A larger beam could interact with areas with different refractive indices at the same time making the Cherenkov ring wider and difficult to analyze.

3.2 HELIX Aerogel Calibration System Components

The system designed to measure the Cherenkov ring consists of three main parts: the linear accelerator producing the electron beam, the aerogel scanning system and the detection system.

3.2.1 Electron Beam

This project uses a 35 MeV electron linear accelerator (linac) located at the National Research Council of Canada (NRC) in Ottawa.

The linac produces a focused pulsed beam of electrons up to 35 MeV with a normal energy distribution with $\sigma_E \approx 0.4$ % [49]. The beam pulses are 2.5 μs long and are produced at a rate, which is defined by the user, in multiples of 30 Hz. After acceleration, the electrons pass through the linac exit window pictured in Fig. 3–3. That image shows the laser alignment for the system. A small laser placed on the wall opposite the exit window allows the linac user to align their setup with the beam location within ∼1 mm of the true beam exit position, as shown in Fig. 3–3.

The linac beam profile is approximately a two-dimensional Gaussian with $\sigma_{x,y} \lesssim$ 2 mm, as measured by a beam profile monitor. The monitor measures the beam profile on wires in two dimensions located ∼100 mm before the exit window to get cross-sections of the beam and check its symmetry and positioning [49].

For the aerogel calibration procedure, the linac was set at 90 nA with the 2.5 μs pulses repeating at 60 Hz. These parameters were settled on during the detector's research and development phase since the current gave sufficient light output to clearly see a Cherenkov ring signal over the background, but without saturating the charge coupled devices (CCDs) on the detection plane.

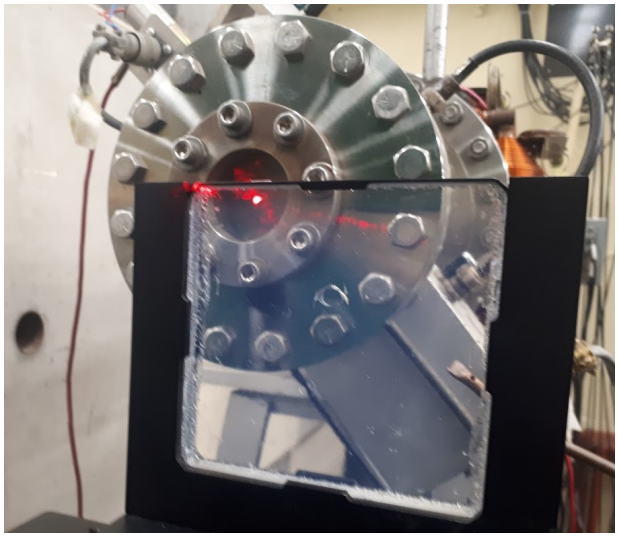

Figure 3–3: An aerogel tile is shown in the foreground. The laser beam passing through the upper left corner of the tile is used to align the system with the electron beam.

This information allows for a simple calculation of the number of electrons in every 2.5 μs linac pulse, according to

$$\frac{90 \times 10^{-9} \frac{\mathrm{C}}{\mathrm{s}}}{\left(1.602 \times 10^{-19} \frac{\mathrm{C}}{\mathrm{electron}}\right) \times \left(60 \frac{\mathrm{pulses}}{\mathrm{s}}\right)} = 9.36 \times 10^{9} \ \frac{\mathrm{electrons}}{\mathrm{pulse}}. \tag{3.3}$$

3.2.2 Charge Coupled Devices

The CCDs used in this project are Toshiba TCD1304DG linear CCDs (Fig. 3–4) that are 1 pixel wide and 3694 pixels long. Each CCD features 32 dummy outputs at the beginning followed by 3648 active pixels, which collect photons, and ending with 14 additional dummy outputs [50]. The pixels themselves are 200 μm wide and 8 μm long p-n photodiodes. Since the CCD is only one pixel wide and oriented radially from the board centre, the 3648 active pixels on each of the sixteen CCDs record

a one-dimensional radial profile of the Cherenkov ring along 8 μm×3648 pixels = 29.184 mm.

Figure 3–4: Toshiba TCD1304DG CCD.

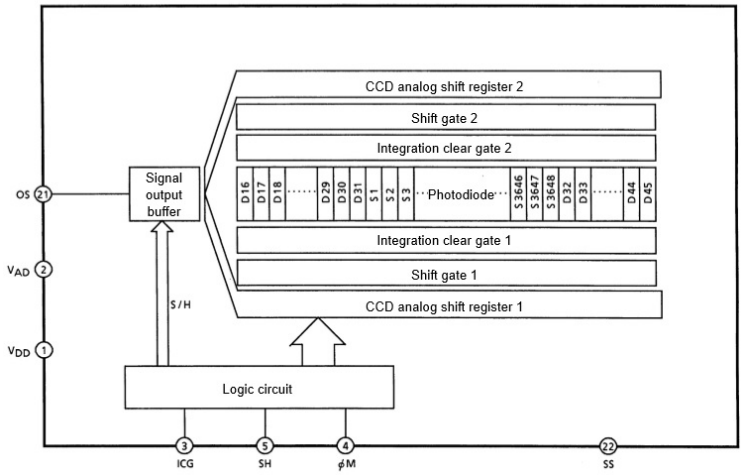

Figure 3–5: A diagram of the TCD1304DG layout from [50]. Three of the CCD pins are occupied by the ICG, SH and ϕM input timing signals. V_{AD} and V_{DD} provide power to the CCD. Data collected in the CCD is clocked out through a buffer to the output signal (OS) pin.

Each CCD has 22 pins, six of which are occupied. Two pins are reserved for supplying power to the board, one is the output signal pin and the remaining three are for input timing signals, as shown in Fig. 3–5. The CCDs are plugged into sockets on the electronics board to provide the input power and timing signals and to direct the output signals.

Three signals are required to run the CCDs. The shift gate (SH) is responsible for setting the exposure window; one pulse starts the exposure and the other ends it. During that exposure time, the CCDs accumulate charge from collecting Cherenkov photons. The integration clear gate (ICG) pulse acts as the readout trigger to the CCDs, after the exposure, to initiate readout of the individual pixels. It is also used as the system wide data acquisition trigger. The master clock (ϕM) is a 2 MHz square wave that shifts and reads out a pixel of a CCD every four ϕM pulses. This

works out to be every 2 μs. Each CCD has 3694 pixels so it is read out in 7.388 ms. The process of creating these timing signals will be discussed further in Section 3.3.2.

3.2.3 The Cherenkov Ring Detection Board

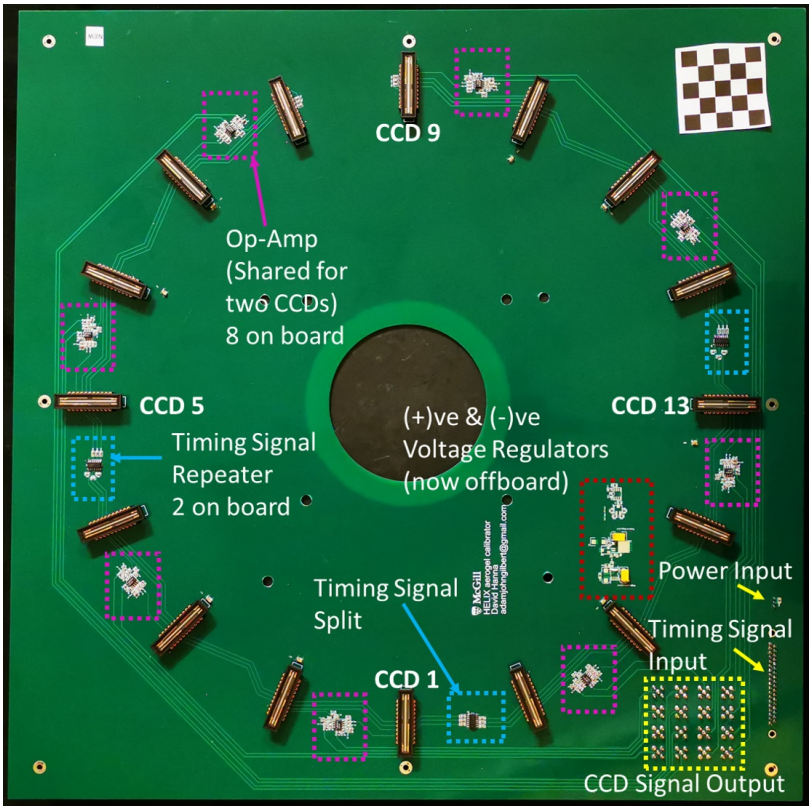

Figure 3–6: Diagram of the detection board designed and built by Adam Gilbert, an electrical engineer at McGill University, for this system. Any changes to the original board are given in the diagram in red, timing signal repeaters and splits are outlined in blue, the op-amps are outlined in magenta and the board connections for power, timing signal input and signal output are outlined in yellow.

The Cherenkov ring detection board holds the CCDs that detect the Cherenkov photons produced from the interaction of the electron beam with aerogel. It consists of a 500×500 mm^2 printed circuit board (PCB) designed by Adam Gilbert, an electrical engineer at McGill University, with the sixteen CCDs arranged radially around the board centre, as shown in Fig. 3–6. The CCDs are positioned such that the centre of each CCD is at a radius of 200 mm from the centre of the board so that it can record the radial profile of the Cherenkov ring. The ring is sampled at equal angular

intervals. The premise of this detection board is that the centre and radius of the Cherenkov ring can be calculated accurately with this sampling without having to detect the full Cherenkov ring.

The three timing signals that control the exposure and readout of the CCDs are produced by external NIM/CAMAC electronics modules and all enter the detection board through a connector in the back. These signals are split and copied so that each of the three signals reaches all of the CCDs. A single trigger sent to the board exposes and reads out all of the CCDs simultaneously. Data from the CCD pixels are routed to the digitizing electronics via coaxial cables with one cable per CCD.

3.3 Readout Sequence and Electronics

The pulses and timing signals are an essential part of running the CCD data acquisition (DAQ) system and ensuring that there is low electronic noise and background light levels. For the system electronics, there are pulses that are created with the linac electronics and those that make the CCDs function.

3.3.1 Linac Electronic Pulses

The trigger pulse is a signal provided by the linac electronics with the same frequency as the electron beam pulse. It acts as the overall trigger for the aerogel calibration system. The electron beam pulse occurs approximately 50 μs after the trigger. This time between the trigger and the beam pulse leaves some time to initialize the CCD exposure window so that when the beam pulse occurs, the CCD exposure will have already begun to collect the resulting Cherenkov photons.

However, there is some jitter observed in the arrival time of the beam pulse relative to the trigger. To amend this, there is an electronic alignment pulse created from the beam pulse that is 15 μs wide. This width encompasses the full range of the jitter observed in the beam arrival time, thus the electron beam pulse will occur at some point in this 15 μs window, as shown in Fig. 3–7.

If the delay is set properly, the alignment pulse will fit between the two shift gate (SH) pulses separated by the 20 μs exposure time. This effectively guarantees that a single beam pulse will occur during each CCD exposure window so that the CCDs collect the photons from that beam pulse. The process of creating the integration clear gate (ICG) and SH pulses for the CCDs are discussed in the next subsection.

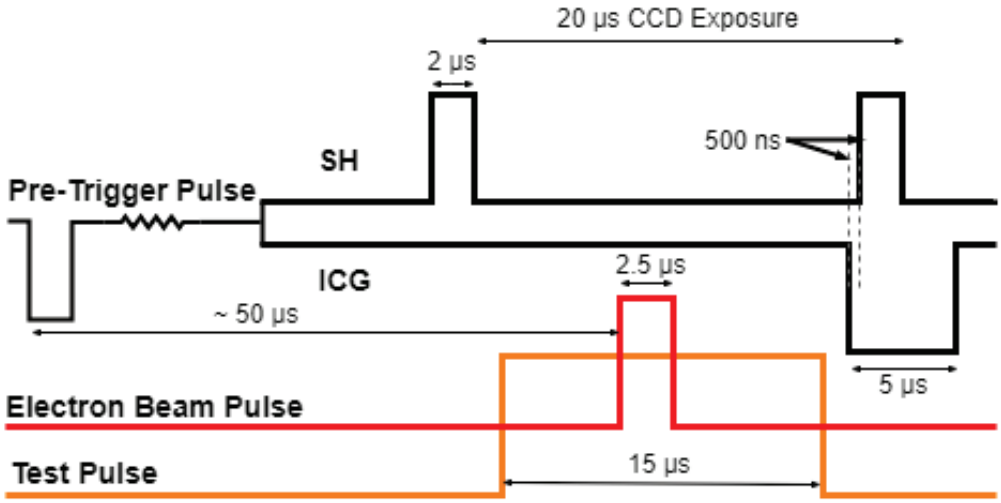

Figure 3–7: The relative timing of the electronics and beam pulses. The SH and ICG pulses are initiated by the trigger pulse. The trigger, alignment and beam pulses are all initiated by the linac electronics, but are separate signals. The beam pulse occurs ∼50 μs after the trigger. A delay after the trigger pulse aligns the SH pulses around the beam pulse. The beam pulse timing jitters relative to the trigger, so the alignment pulse encompasses the range for the jitter and is used to set the SH delay. The ϕM square wave is not shown as its short 500 ns period would clutter the diagram.

3.3.2 CCD Timing Signals

The timing signals for the CCDs are made using a series of NIM/CAMAC electronics modules. As mentioned previously, there are three timing signals to run the CCDs: the SH is made of two pulses marking the start and end of the CCD exposure, the ICG starts the readout of the pixels and the ϕM pulses clocks the data along and out of the CCD.

The main purpose of this timing signal system is to produce clean timing signals that synchronize the CCD trigger/readout with the linac beam pulses so that the CCDs are only exposed when the beam pulses, as discussed in Section 3.3.1. The key

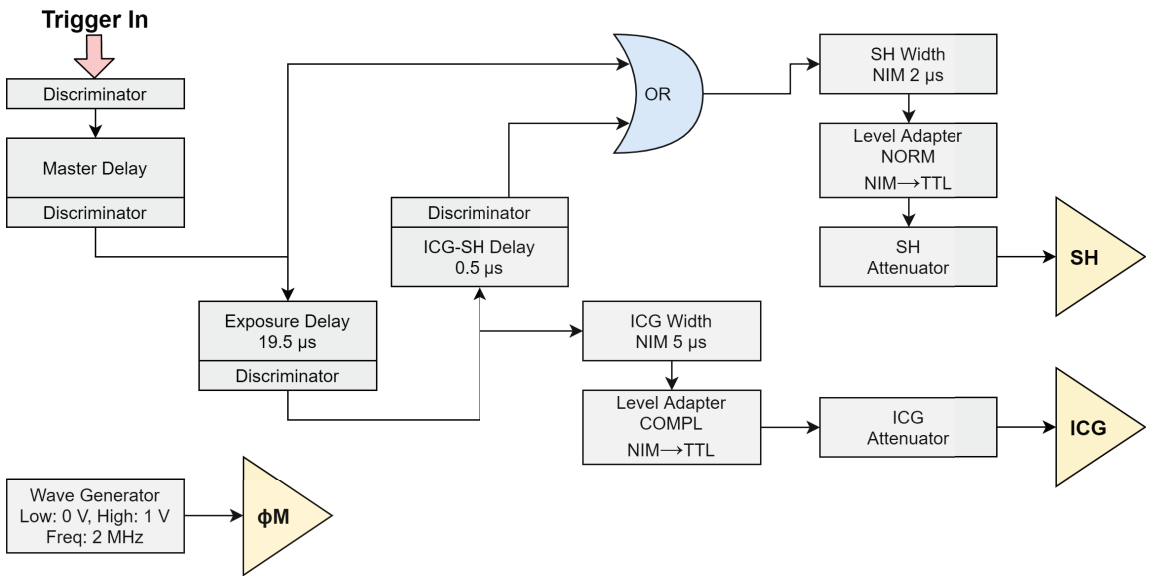

Figure 3–8: Diagram of the NIM and CAMAC system to produce the shift gate (SH), integration clear gate (ICG) and master clock (ϕM) timing signals for the CCDs given a trigger from the linac.

to connecting the beam pulse to the electronics trigger is the trigger NIM pulse and the master delay shown in Fig. 3–7 and Fig. 3–8. The trigger consistently pulses about 50 µs before the beam pulse. While the rest of the circuit in Fig. 3–8 is involved in coordinating the timing and structure of the ICG and SH pulses, the first delay in the circuit shifts all of those pulses so that the SH pulses surround the beam pulse.

The logic involved in creating the timing signals is summarized in Fig. 3–8 for the SH and ICG pulses. There are multiple NIM/CAMAC units that are used to split the discriminated trigger pulse signal to be used in the rest of the circuit. The length of pulses and their relative timing are based on requirements from the CCD data sheets [50]. All of the timing pulses are created after the trigger pulse and set to their relative timing structure and shape by a series of gate and delay generators, signal splits, a logic unit, level adapters and attenuators.

The master clock, ϕM, is generated using a Berkeley Nucleonics Model 645 arbitrary waveform generator to produce a 2 MHz square wave between 0 V and 1 V. The pulse is sent directly to the board to set the clock pulse rate.

The final relative timings of the pulses generated in the timing circuit are shown in Fig. 3–7. In this setup, the two SH pulses are 2 μs positive-going pulses, separated by 20 μs, which sets the exposure window of all of the CCDs for a given single trigger. The electron beam pulse arrives during that exposure time. When the exposure ends, the ICG pulse then initiates the readout of the pixels according to the timing of the ϕM pulses, where a pixel is read out every four ϕM pulses.

3.3.3 Data Acquisition Computer

The data acquisition is done using a single-board cPCI-6620 series Adlink computer in a crate connected to four Acqiris U1063A DC270 Fast Analog to Digital Converters (FADCs) [51]. The Acqiris DC270 is an 8 bit, 250 MHz bandwidth, 1 GS/s FADC with four internal channels and one external trigger channel. The computer runs a Linux-based operating system with drivers for the FADCs installed. The acquisition code consists of a central C++ structure to send the commands to the FADC, and a Python-wrapper to make the program easier to use. The FADC collects data by sampling these input channels at a user-defined number of samples and sampling rate after receiving a trigger pulse through one of the external channels.

The sixteen CCD outputs from the board are connected to the internal channels on the FADCs. The ICG pulse is the main trigger for the system in one of the FADC's external channels; it starts the CCD readout and the FADC sampling. The clock-out of the pixels and the FADC sampling are run completely separately, with one sending signals and the other recording signals. However, the parameters are set such that when one pixel is clocked out the FADC is ready to read it. After the ICG pulse, every four ϕM pulses, a single pixel is shifted and read out (clocked out) simultaneously on all of the CCDs. For a 2 MHz ϕM, the pixels are clocked out at 0.5 MHz or 2 μs for each of the 3694 pixels and those signals are sent to the FADC. Separately, but off the same ICG trigger, the FADC is set to sample from the signals sent to its channels from each CCD. The FADC is set to sample every 2 μs for 3694

samples starting at the same time as the CCD clock out so there is a single sample recorded on the FADC per pixel. The total readout takes 7.388 ms. When this data is analyzed, each recorded data value corresponds to the signal from a single pixel and can be plotted to form a trace like Fig. 3–9.

3.3.4 CCD Settings

All CCDs are supplied with 4.9 V, but when read out on the digitizers, each CCD has a slightly different baseline voltage and range due to manufacturing tolerances and how long the CCD has been used. Studies of the range of each CCD showed that they had very similar baselines and ranges. The digitizers are set to act like a digital oscilloscope so it has an adjustable time axis and an adjustable voltage axis. Those values are set so that the signal fits perfectly in the digitizer window. For the CCDs, the window size (1 V) and offset ($\sim$-0.7 V) for the readout with the FADC is the same for all of the CCDs. The time axis is set to match the number of samples (3694) and sampling rate (0.5 MHz) of the CCD readout.

Each CCD has a range of 0.7-0.8 V between the baseline of a completely dark CCD to the CCD saturation level. If light is applied past the point of saturation of a CCD pixel, then the signal will begin to bleed over to the neighbouring pixels. For this reason, the current of the linac is set such that there are enough photons to make a clear signal in the pixels, but it does not saturate them.

The FADC functions on an inverted voltage scale so that the baseline is at a high voltage and any light on the CCDs will cause the voltage recorded to decrease. Fig. 3–9 is an example of a single CCD readout, or trace, for one CCD directly from the digitizer showing this effect. There is one data set with a Cherenkov ring (data trace) and one from the dark frame (dark trace). The inverted scale is apparent with the higher signal voltage recorded for the dark trace and lower voltage for the data trace. The dark frame records the CCD baseline. The dark frame is the pixel mean of 100 dark traces taken successively. The data is usually plotted as the dark

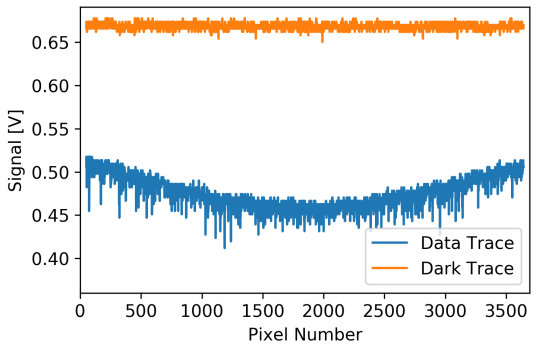

Figure 3–9: A single CCD readout trace from a Cherenkov ring data set and a dark frame readout. Both traces are raw data directly from the digitizers.

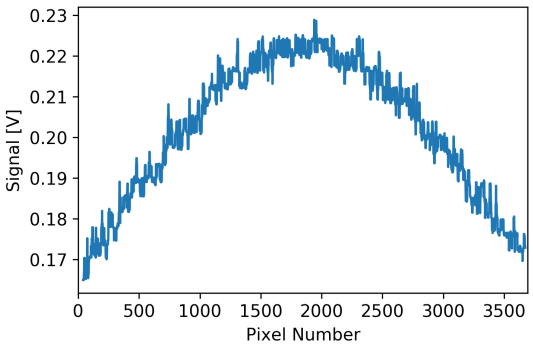

Figure 3–10: A single readout Cherenkov ring trace subtracted from the 100 dark frame readout average. The trace is smoothed with an 11 pixel median filter.

frame subtracting each data trace from it to get the signal above the background, as shown in the single CCD profile in Fig. 3–10. The signal change from the baseline is equivalent to the charge generated in the pixels from the absorption of photons.

The analysis chapter, Chapter 4, will describe the conversion of pixel number for each CCD to that pixel's physical position on the detection board, which is used during analysis. Fig. 3–10 is an example of a trace that would then be fit with parabolas to determine the peak position.

3.4 Scanning Setup

The experimental setup for the aerogel calibration system consists of two parts shown in the digital model of Fig. 3–11. The first part consists of the detection board that sits atop a three-axis positioning system. The second part is a two-axis positioning system with the aerogel in its holder on top of that system. This moves the aerogel in a grid pattern in the electron beam path. Both of these parts are mounted on an optical table so that they are aligned with each other and then the entire system can be positioned so that the detection board and the aerogel face are perpendicular to the beam.

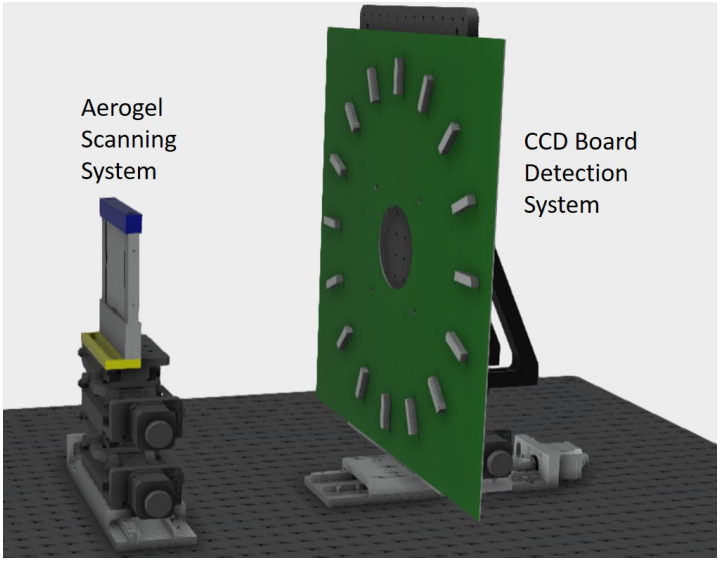

Figure 3–11: A digital model of the aerogel calibration system. The electron beam enters from the left producing a Cherenkov cone in the aerogel. The Cherenkov ring is detected by the CCDs on the board on the right. Model Credit: Thomas Rosin.

3.4.1 Detection Board Position and Orientation

The detection board is mounted vertically with the CCDs positioned as shown in Fig. 3–6, with CCD 1 at the bottom and the CCD number increasing clockwise. More details of the board itself and its electronics were discussed in Section 3.2.3. The board output on the bottom right corner leads to the FADC channels. The orientation of the board in Fig. 3–6 is how it is positioned in the setup. The board is supported vertically using brackets on top of the positioning system as can be seen in Fig. 3–12.

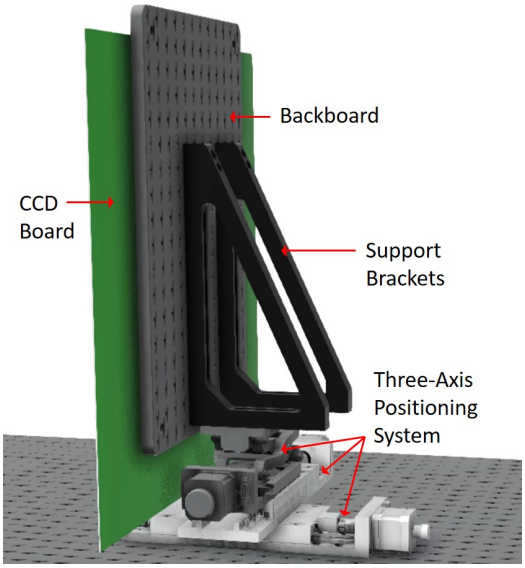

Figure 3–12: The back of the detection board system supported on the three-axis positioning system. Model Credit: Thomas Rosin.

Fig. 3–11 and Fig. 3–6 show a clearer view of the front of the board. The electron beam passes through the middle of the hole in the detection board.

3.4.2 Detection Board Positioning System

The board positioning system consists of two 100 mm range horizontal stages stacked, but oriented perpendicular to each other, and a single 50 mm vertical stage on top to form a three-axis positioning system. On top of this system there are two brackets supporting a small vertical optical breadboard that the detection board is secured to, as seen in Fig. 3–12.

These positioning stages are controlled by the user to calibrate the distance from the aerogel to the CCDs and to align the centre of the board with the Cherenkov ring centre. Any changes to the stage position are documented to be included in later analysis if necessary. These stages are used before the beam scans begin, but remain fixed during the scan.

3.4.3 Aerogel Frame and Holder

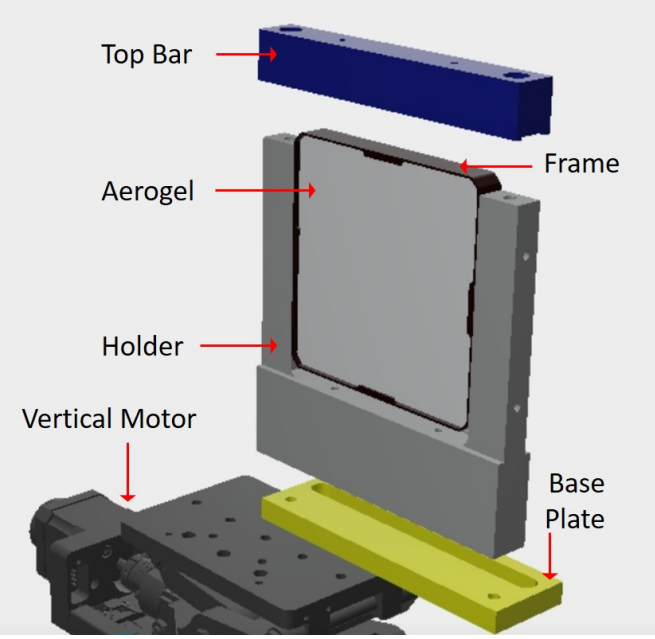

Figure 3–13: Diagram of the exit face of the aerogel tile in the holder. The aerogel is secured in the holder with the top bar. The base plate acts as an adapter between the holder and the stages. Model Credit: Thomas Rosin.

Each aerogel tile is cut such that it fits in a custom-made, anodized aluminum frame, as shown in Fig. 3–13. Since the aerogel is so fragile and brittle, the frame provides some protection to the edge of the aerogel. To secure the aerogel in the frame, it is glued in with Dow Sylgard 184 silicone adhesive. In addition, there are tabs on the edges of the frame. These tabs support the tile, when it is installed in the payload, in case the adhesive fails. The aerogel is placed so that it should be flush

with the inner edge of the frame tabs. Each tile has its own frame with a unique binary label to be able to identify and orient it, as described in Section 3.4.4.

Fig. 3–13 shows how an anodized aluminum aerogel holder secures the framed aerogel to the top of the aerogel scanning system. The holder remains fixed once adjusted to the correct alignment so that each aerogel tile is placed at the same position. It is U-shaped with a groove at the bottom to exactly fit the aerogel frame and secure it to the scanning system. A top bar with the same groove is screwed on the top to prevent the tile from tipping over.

3.4.4 Aerogel Scan Coordinate System

Fig. 3–14 defines the coordinate system of the beam scans. The aerogel is glued into its aluminum frame with the beam travelling towards the observer in this reference frame.

The beam exit face of the aerogel, as seen in Fig. 3–14, can be identified by the tabs next to the face. One of the tabs has a binary label that consists of a starting and ending mark and space for a six digit binary code between those. The flight quality aerogel tiles are numbered 1-50. The tile in Fig. 3–14 has the binary label -001010- that identifies it as flight tile 10. For all of the flight quality aerogel tile scans, the tiles are oriented with the tile ID along the top edge. Fig. 3–14 shows the labelled axes of this coordinate system. Any rotation of the tile is done by a right-handed rotation about one of the axes.

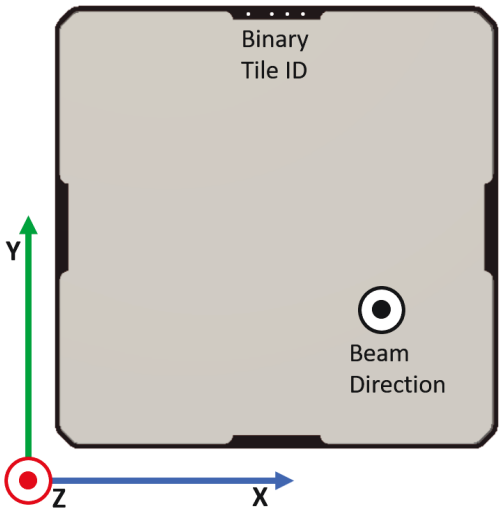

Figure 3–14: The coordinate system for the aerogel calibration system. All of the tile rotations about one of the axes are right-handed rotations.

3.4.5 Frame Scanning System

This system involves a stack of a single 100 mm range horizontal stage and two vertical 50 mm range stages with the aerogel holder bolted on the top so it has a vertical and horizontal range of 100 mm as visible in Fig. 3–11. The aerogel and the range of the positioning system are deliberately the same size so the entire aerogel tile can be scanned in the beam. To scan the aerogel, the beam and the detection board are fixed so the scanning stages move the aerogel in the beam's path in a 5 mm grid.

3.4.6 Frame and Board Systems Power and Control

Both of the systems are secured to a large optical breadboard base and fixed into place for the duration of the aerogel tests, as shown in Fig. 3–11. They are powered from a common 24 V DC power supply. All six of the stages are connected via ribbon cables to a motor driver control system where there is one DM556T digital stepper driver for each of the six stage motors. These drivers are all controlled by an Arduino Mega [52]. An Arduino program is integrated into a series of serial based commands to move each stage in the system.

3.5 Scanning Procedure

A lot of effort has been put into refining the procedure to make the results as reproducible as possible. To accomplish this there are tasks that need to be done at a specific time in a certain order to maintain the same standard for all scans.

3.5.1 Pre-Beam System Checks

There are several checks that need to be done on the system itself before the beam hall is closed and the beam is turned on. These checks include verifying that the timings signals are working properly and ensuring that the CCDs are free from dust that can block Cherenkov light.

In general, all of the components that cannot be directly observed during the scan procedure are checked ahead of time. All of the stages are checked to see if

they move properly for a specific movement command. If the stages failed to move, the same part of the aerogel would constantly be exposed to the beam. This would damage the aerogel after a few minutes exposure and cause the tiles to crack. The entire setup is covered with a large light-tight box to ensure that any stray photons from emergency lighting or electronics do not reach the CCDs.

3.5.2 Initialization

The initialization process of the beam test consists of all of the tasks that are done before every beam scan. The principal tasks are acquiring two data sets to ensure that the data set will be as clean and accurate as possible for analysis.

The linac is completely shut down every night so before a new day of aerogel calibration, the linac must be turned on. This process takes 20-30 minutes. Throughout the day, the beam is temporarily turned off so that the aerogel tiles can be changed in the calibration system. The system is not completely shut off for each of these temporary stops. The radio frequency feed to the linac is turned off to prevent the electron gun from pulsing. This can be turned back on, once needed, to produce a stable electron beam current in a minute.

The dark frame data set is taken before the beam is turned on and consists of 100 readouts of the 16 CCDs. This is a measurement of the background light levels when the beam is off and the linac hall is dark. The dark frame also corrects for the slightly different baseline in each CCD. All of the grid scan data sets use the same dark frame that is taken just before the scan.

The test data set is taken once the beam has been turned back on and it is stable at 90 nA. This test involves repositioning the board such that the Cherenkov ring is optimally aligned with the centre of each CCD. When the board is properly aligned the grid scan can begin. The position of the board's z-stage is recorded after this alignment as its position is necessary to calculate the distance d between the aerogel face and the CCD to use in the analysis (see Appendix B).

3.5.3 Graphical User Interface

The entire calibration system is controlled remotely from a graphical user interface (GUI) to move the stages and initialize data acquisition. The GUI was written by the author to have a simple interface for anyone who uses the system. Fig. 3–15 is a screenshot of the GUI.

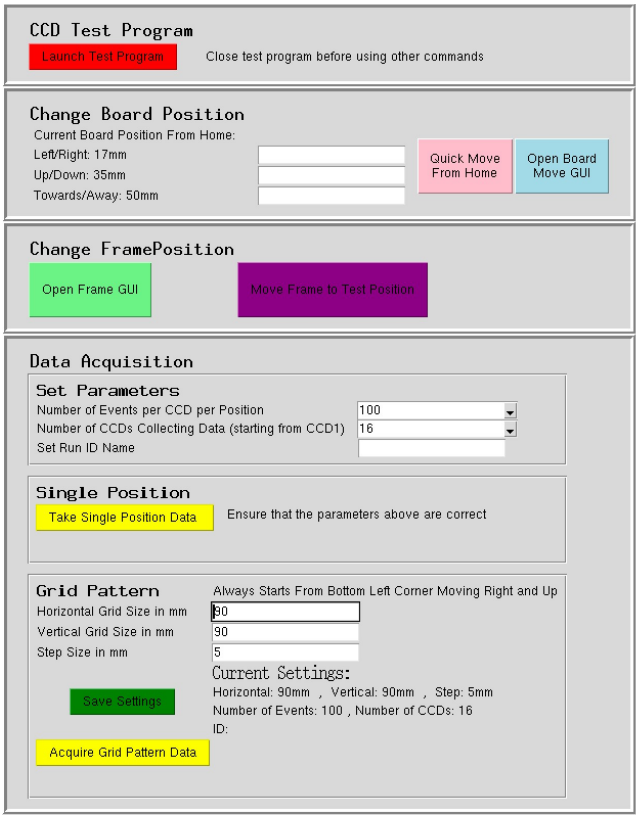

Figure 3–15: The graphical user interface used for data acquisition and for moving the frame scanning system stages.

The first section opens the test program that is included when the FADC drivers are installed. It is mainly used for CCD level troubleshooting.

The next section changes the board position. One moves all of the stages home and then moves them to the specified positions for large scale movements. The second opens up a smaller GUI to allow the user to press a single button to move any of the stages in 1 mm or 5 mm increments. It is used to move stages to centre the Cherenkov ring on all of the CCDs on the board.

The next section changes the aerogel frame position on its positioning system with essentially the same pop-up GUI except for two axes. There is also a shortcut to move the frame stages to (25,25), the distance from home horizontally and vertically in mm, for the test data set just before the grid scan.

The data acquisition section is the main purpose of this GUI. The grid scan was written during the project development to be as flexible as possible allowing for any

number of readouts, number of CCDs read, grid size and spacing. The single position takes a data set with the above parameters without moving any stages. To start the grid scan, the user saves the settings and begins the run in the Grid Pattern section, which moves the stages, acquires data and organizes files automatically.

3.5.4 Grid Scan Parameters

To avoid complications arising from scanning too close to the tile edges, the grid scan only takes data on the inner 90 mm square of the aerogel tile between 5 mm and 95 mm vertically and horizontally. There is 5 mm between each of the grid scan points and this results in a total of $19 \times 19 = 361$ data points. At each of these grid positions, the data set consists of 100 beam pulses and readouts. During each readout, the pixels are clocked out simultaneously on all of the CCDs and written to a buffer before the next beam pulse occurs.

As shown in Fig. 3–14, the aerogel coordinate system defines (0, 0) as the bottom left corner of the tile. When the stages are at home, the vertical stages are at their lowest so the beam actually passes through the (0, 100) position. When the beam scan starts, the stages first move to (5, 95) and then take data in a horizontal row before the moving up by 5 mm to scan the next line (90 mm) on the aerogel tile moving horizontally in the opposite direction. This scan pattern continues until the final grid point at (95, 5).

3.5.5 Data Formatting and Management

There is a standard scan directory naming convention for this system. One example of this is 'flight30_X0Y0Z0_191212'. The first part indicates the tile name 'flight30' so it is the 30^{th} tile deemed to be of flight quality by the tests in Section 2.4.3. Next is the rotation of the tile according to the right-handed coordinate system rotation in Fig. 3–14. X0Y0Z0 is the base orientation where the binary label is at the top and the beam exits out of the aerogel face with the tabs and label. This is followed by the date in YYMMDD. For the grid scan, this directory contains separate

.dat data files for each scan point. At the end of each of those data file titles there is an added '_hn_vm' tag. n and m are two-digit numbers to indicate the horizontal and vertical stage position for that data file relative to the origin in mm.

Each data file contains the 100 readouts of all of the 16 CCDs with 3694 samples for each CCD for a total of 5910400 measurements. The data file is a simple .dat file with a column for each CCD. Each row is the signal from one pixel for a readout of the CCD. Subsequent readouts are appended to the bottom. For example, readout 1 will be the data in rows 0-3693 and readout 2 is in rows 3694-7387. All of the data is written in binary format because there is a lower overhead time to write that many values in binary rather than floats. By switching to writing in a binary format the program went from completing an entire scan in 62 minutes with a 50 Mb file per scan point to a scan that took 35 minutes with a 23 Mb file per scan point. The program also outputs a header file to save the FADC settings used for that scan. These include the voltage range, offset, time between samples and the total number of samples.

At the beginning of the grid scan program, the parameters for the scan are read in from the GUI. Then the program initializes the construction of the dynamically-allocated arrays that are used as pointers for the data. This sets the size of the buffer memory for a three-dimensional array where the dimensions are the number of pixel samples per readout, the number of CCDs and the number of readouts per position. All 100 readouts are collected to fill the entire buffer before it is written in binary format to the file. At the end of the readout, the destructor is called to clear the constructed arrays so that the next data set can be acquired.

3.5.6 Beam Scan Timing

The beam scan process was refined over the course of more than a year of research and development with the electron beam before the production run of aerogel scans

was undertaken. This subsection is a detailed description of the timing involved in all of the processes of the calibration procedure.

For the actual grid scan there are two main contributions to the overall time of the scan: the data acquisition and the stage movements between grid points. The 60 Hz beam pulse rate means that there are 16.7 ms between pulses. This rate was specifically chosen so that there was enough time to expose the CCDs, read them out and write them to the buffer before the next pulse came. The CCDs are exposed for approximately 20 μs and then read out at a rate of one pixel every 2 μs. The total readout of the CCDs takes up 7.4 ms of the 16.7 ms between pulses, with a small amount of time dedicated to saving data to the buffer. The system does not do anything for the rest of the time between pulses. This was set intentionally as it was found that at trigger rates higher than 60 Hz, the FADC missed random triggers. The buffer is not written to the disk until all 100 readouts in that position are taken. In total, initializing the points, acquiring 100 readouts and writing all of that data to disk takes about 3.3 s per point. It then takes about 2.5 s for the stages to receive the command to move 5 mm, move that distance and then settle before the next data acquisition. With all of these different timing processes, a complete grid scan consistently takes about 35 minutes.

In an eight-hour day of aerogel scans, it is possible to scan 8-9 aerogel tiles. The start time of each grid scan is recorded in the aerogel scan logbook summary presented in Table 3–1. This table shows that there are 50-60 minutes between each aerogel scan. The scan itself takes 35 minutes. This would suggest that there is at least a 15 minute period between the end of one scan and the beginning of the next. There is a 2-3 minute pause before entering the linac hall to allow for the ozone produced from the linac electrons to subside. The aerogel tile is then taken out of the holder, repackaged and then a new one is secured into the holder. When that is done, the room is secured and sealed again. That whole process takes about 5 minutes. It takes

a further 5 minutes to take the dark frame, turn the beam on and allow it to stabilize and to take the test data sets to align the board, as outlined in Section 3.5.2.

3.6 Data Summary

There were fourteen multi-day trips to the electron beam at NRC in Ottawa. During the last four trips (11 days) all 50 flight quality aerogel tiles were fully scanned. Table 3–1 are the logbook entries for the flight quality aerogel tile scans.

All of the flight tiles were scanned at least once with a few repeated scans for tiles where data was missing due to beam quality. There was also at least one scan of the reference tile HLX 21-3 at the beginning of each day. The analysis of all the data is still ongoing.

Date	Tile ID	Time
2019-12-03	HLX 21-3	4:28:24 PM
	flight4	5:29:25 PM
	flight5	6:29:44 PM
	flight6	7:24:18 PM
	flight7	8:14:31 PM
2019-12-04	flight8	11:02:50 AM
	21-3	11:52:43 AM
	flight9	12:38:28 PM
	flight10	2:10:46 PM
	flight11	3:07:03 PM
	flight12	4:03:41 PM
	flight13	5:04:54 PM
	flight14	6:20:30 PM
2019-12-05	HLX 21_3	10:27:33 AM
	flight15	11:21:30 AM
	flight16	12:11:05 PM
	flight17	1:00:27 PM
	HLX 21_3	5:15:30 PM
	flight18	6:07:34 PM
	flight19	6:51:16 PM
	flight20	8:20:33 PM
	flight21	9:07:06 PM
2019-12-06	HLX 21_3	10:15:01 AM
	flight1	11:10:55 AM
	flight2	12:01:51 PM
	flight3	1:39:30 PM
2019-12-11	HLX 21-3	11:54:20 AM
	flight22	12:54:41 PM
	flight23	2:49:33 PM
	flight24	3:34:21 PM
	flight25	4:26:11 PM
	flight26	5:09:24 PM
	flight27	6:17:27 PM
	flight27	7:05:41 PM
2019-12-12	HLX21-3	10:12:29 AM
	flight28	11:34:45 AM
	HLX21-3	12:19:18 PM
	flight29	1:06:10 PM
	flight30	2:06:25 PM

Date	Tile ID	Time
2020-02-18	HLX 21-3	11:53:42 AM
	flight31	1:09:37 PM
	flight32	2:04:34 PM
	flight33	3:00:55 PM
	flight34	3:45:57 PM
	flight35	4:47:06 PM
	flight36	5:37:55 PM
	flight37	6:45:12 PM
2020-02-19	HLX 21-3	12:13:03 PM
	flight35	5:06:13 PM
	flight36	5:51:56 PM
	flight37	6:40:32 PM
	flight38	7:39:01 PM
	flight39	8:28:09 PM
	flight40	9:12:29 PM
	flight41	10:04:42 PM
	flight42	10:58:21 PM
2020-03-02	HLX 21_3	4:22:38 PM
	flight43	5:14:57 PM
	flight44	6:45:48 PM
	flight45	7:31:32 PM
2020-03-03	HLX 21_3	11:51:53 AM
	flight45	1:22:10 PM
	flight46	2:12:56 PM
	flight47	3:02:39 PM
	flight48	4:00:42 PM
	flight49	7:00:47 PM
	flight50	7:56:40 PM
	flight6	8:48:22 PM
2020-03-04	HLX 21_3	11:56:19 AM
	HLX 21_3	12:45:00 PM
	HLX 21_3	1:38:00 PM
	HLX 21_3	3:17:21 PM
	flight9	4:26:31 PM
	flight10	5:28:08 PM
	flight12	6:27:27 PM

Table 3–1: Aerogel scan logbook summary.

CHAPTER 4
Aerogel Scan Analysis

Ste O'Brien, a postdoc at McGill University wrote the data analysis software used to get from the raw data sets collected during the beam scan to full aerogel tile refractive index maps. This section was written by the author of this thesis to explain that software's features and general data analysis properties.

4.1 Mapping CCD Output to Physical Position

For each of the 361 positions in a grid scan, there is a data file with 100 readouts of 16 CCDs with 3694 pixels each. For every grid there is also a file of 100 dark readouts to correct for background illumination on the CCDs. The dark frame used for analysis is the pixel by pixel average over the 100 dark readouts, which results in a single 3694 element data set for each CCD. The inverted scale of the data set is dealt with by subtracting each of the 100 readouts from the dark frame leaving a positive going signal with a baseline at 0 V. Then an 11-pixel-wide median filter is applied to the readouts to smooth out pixel-to-pixel variations, as shown in Fig. 4–1.

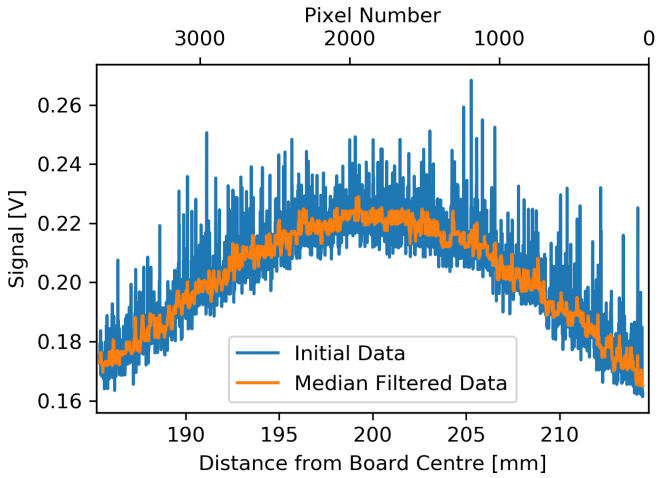

Figure 4–1: A background subtracted initial CCD readout (blue) and the same data processed with an 11 pixel median filter (orange). The x-axes show the conversion between pixel number and the physical position of that pixel on the board.

These variations could come from different pixel gains or from the various sources of noise. CCDs will have dark noise, the photon counting shot noise from Poisson

statistics, readout noise associated with converting photoelectrons to a voltage and noise in the digitizers among other sources. The median filter helps to reduce the intensity of these variations to make it easier to analyze the data. It does this by comparing the signal of a pixel to the signals in surrounding pixels and taking the median signal of the group as the central pixel's new value. An outlying signal from a single pixel compared to the overall trend will not pass this filter and thus the overall CCD readout is smoothed out while preserving the underlying signal structure of the Cherenkov ring.

The 16 CCDs are positioned radially and at equal angular intervals where the CCD centre is at a radius of 200 mm from the board centre. Each of the CCDs' 3694 pixels are 8 μm long. If the CCDs are placed perfectly, where half the pixels are on either side of 200 mm, then the first pixel should be at 214.772 mm and the last one at 185.228 mm from the board centre. The CCD position is highly unlikely to be exactly correct, but this micron-level pixel position is given for the purpose of having a pixel position for the data analysis. The raw data is usually expressed in pixel number, but this is converted to a distance r from the board centre using

$$\phi = (CCD - 1) \times 22.5^{\circ} \tag{4.1}$$

$$r = 214.772 - (p \times 8 \times 10^{-3}) \text{ mm} , \tag{4.2}$$

which depends on the CCD number (1-16) and the pixel number p (0-3693). This conversion is shown in the two x-axes of Fig. 4–1.

The coordinates of each pixel on every CCD can be calculated by

$$x = -r\sin\phi \text{ mm} \qquad y = -r\cos\phi \text{ mm} . \tag{4.3}$$

With the CCD angle and the pixel number, it is simple to match the position of each pixel on a CCD physically with the data for that pixel. An example of this is shown in Fig. 4–2. In Fig. 4–2, the CCD readouts are plotted 150 mm closer radially

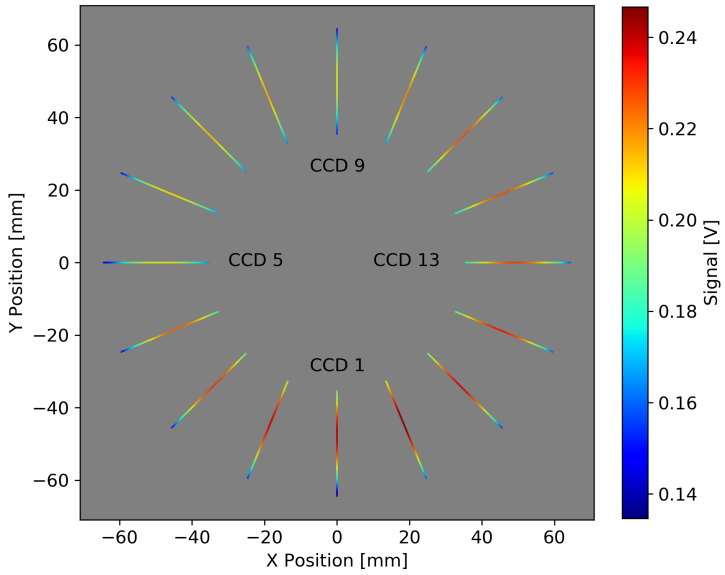

Figure 4–2: An example of the output of the CCDs projected to their angular position. To make the CCD details easier to see, the CCDs are plotted at 50 mm radius instead of the true 200 mm position. The intensity of the light recorded by the CCD is given by the colour scale.

to the board centre compared to their physical positions to make it simple to see the Cherenkov ring sampled by the CCDs. The plot uses the mean CCD readout for the 100 events on each CCD with the dark frame subtracted and then matches that data to the physical pixel coordinates using Eq. 4.1-4.3. A version of this plot is used to centre the Cherenkov ring on the CCDs before each grid scan.

4.2 Determining the Peak of the Cherenkov Ring

At this point in the analysis, the pixels of the 16 CCDs are mapped to their physical positions on the board using Eq. 4.1-4.3. The data for each of the CCDs is then individually fit with a two-pass parabolic fit to find the peak of the distribution, as shown in Fig. 4–3.

For the first parabolic fit in Fig. 4–3a, the first and last 250 pixels of each CCD are ignored as there can be some deviations on the edge of the CCD. This first pass is meant to find the parabolic peak that should be close to the Chernekov ring peak. That first fit peak can be used for the second fit. The second fit, shown in Fig. 4–3b, is another parabolic fit done with the 2000 pixels surrounding the peak of the first fit. This two-pass technique helps to reduce the chance that deviations or noise on

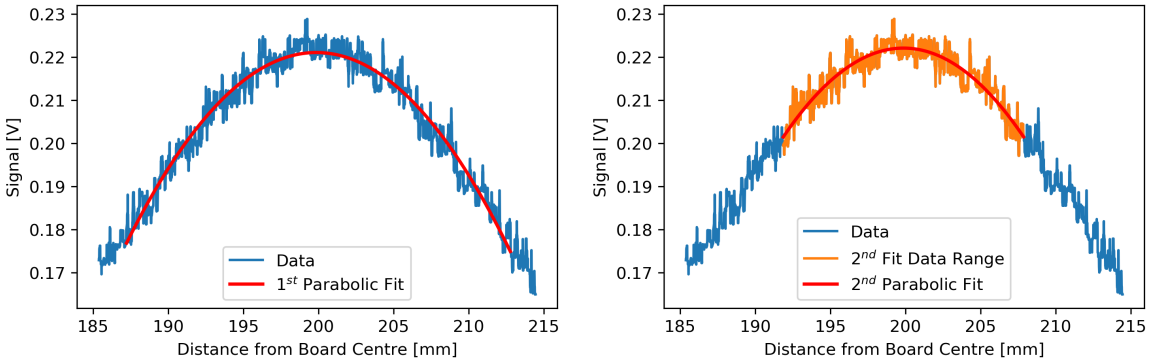

(a) 1st parabolic fit.

(b) 2nd parabolic fit.

Figure 4–3: The parabolic fits to the Cherenkov ring profile data from a single CCD, shown in blue. (a) is the first parabolic fit and it does not include the first and last 250 pixels due to potential edge effects. (b) is the second parabolic fit over a 2000 pixel window around the peak of the first parabolic fit.

the edges of the CCDs affect the final fit peak position. Both fits involve a parabolic fit done with *numpy.polyfit*, a Python least-square polynomial fitter.

Using the parabola standard form formula $az^2 + bz + c = 0$, the peak is found at

$$z_{max} = -\frac{b}{2a}. \tag{4.4}$$

The uncertainty in that peak position is calculated from the diagonals of the *polyfit* covariance matrix and the formula

$$\Delta z_{max} = \sqrt{\left(-\frac{1}{2a}\right)^2 \Delta b^2 + \left(\frac{b}{2a^2}\right)^2 \Delta a^2}. \tag{4.5}$$

Eq. 4.1 and Eq. 4.3 are used to convert the position of the second parabolic fit peak for a given CCD, z_{max}, to its physical position on the detection board (x_{max}, y_{max}), setting $r = z_{max}$.

4.3 χ^2 Cut to Poor Parabolic Fits

The inclusion of a χ^2 cut in the data analysis was motivated by the observation of signal variations in just under 20% of the CCD readouts which are not associated with photons. These variations will be referred to as background waves. The majority of the data does not have significant noise and remains essentially constant except

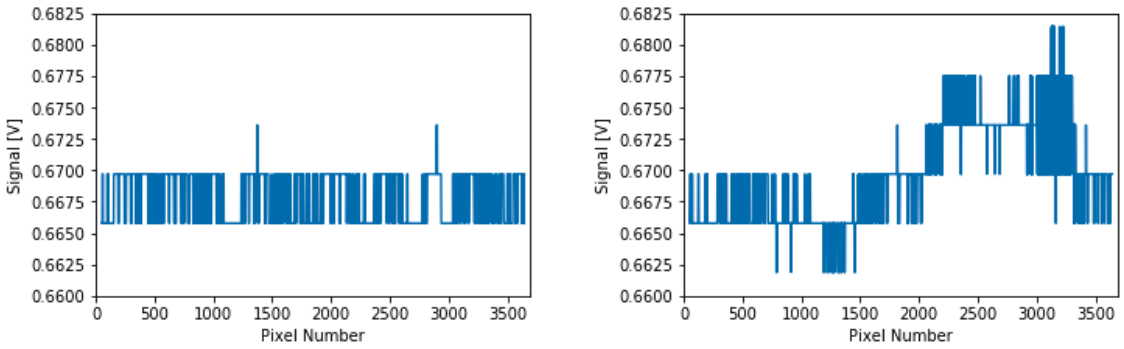

(a) Clean Dark Frame Trace.

(b) Dark Frame Trace With Background Wave.

Figure 4–4: Examples of dark frame traces without (a) and with (b) the background wave. The background wave appears in about 20% of dark and data traces.

for some small variations on the level of the digitizer sensitivity, as seen in Fig. 4–4a. The digitizer measures the voltage at fixed intervals hence the step structure. Ideally, there would be no background wave and, in the absence of Cherenkov light, the trace would be essentially flat like in Fig. 4–4a. The dark frame traces were used for these plots instead of Cherenkov ring data as it is simply much easier to see the waves on a flat background. Fig. 4–4b is an example of the next CCD readout in the same data set that has this background wave. The background wave will appear in all 16 CCDs for a single readout. Overall, these waves have a total voltage range of about 18 mV covering the majority of the pixels. A typical Cherenkov ring has a voltage range of the CCD of about 70 mV so this effect can cause variation in the voltage on the scale of 25%. Even at this level of noise, the gradual change of the voltage from this background wave across the CCD makes it difficult to see on a plot, but easy to identify in a χ^2 distribution.

The dark frame is an average of the 100 readout traces for each of the 16 CCDs. The background wave will also appear in about 20% of the dark frames. Based on observations, the background wave can appear anywhere in the CCD pixels. Generally, the average dark frame was not observed to be noticeably affected by the background waves. χ^2 cuts eliminate the data frames with the background wave.

After an extended search into the source of the background waves, it was traced to cross-talk caused by the ϕM signal going into the detection board. Resolving this issue would necessitate redesigning the detection board to separate the timing signal input. The decision was made to account for these waves in the analysis.

A χ^2_{par} cut acts as a filter to eliminate poor parabolic fits to CCD readouts. It is calculated for all the CCDs in each of the 100 readouts excluding the first and last 250 pixels again, but using the second parabolic fit parameters.

The χ^2_{par} is calculated for the parabolic fit for each CCD readout according to

$$\chi^2_{par} = \sum_{i=250}^{3444} \left(\frac{data_i - fit_i}{\sigma_{pixel}} \right)^2 , \tag{4.6}$$

where the sum is over all of the pixels in the desired range and σ_{pixel} is the the pixel error. The χ^2_{par} is usually expressed in its reduced form where $\chi^2_{\nu,par}$=$\chi^2_{par}/(N-3)$ where N is the number of pixels, in this case N=3444-250=3194.

The pixel error is estimated as the pixel-to-pixel variations in the CCD. Consider the signal variation of each pixel i to its immediate neighbours, which is $data_i - data_{i-1}$ and $data_i - data_{i+1}$ for i in the range 250$\leq$ i $\leq$3444. The collection of these two variation calculations for every pixel is expected to form a normal distribution. The pixel error σ_{pixel} is set to the rms of this distribution.

The CCD readouts with the background waves produce the highest $\chi^2_{\nu,par}$ which has been observed to consistently affect just under 20% of the 100 readouts$\times$16 CCDs = 1600 data sets. The simplest way of cutting the affected data sets is to set a straight cut level. This is done by putting the $\chi^2_{\nu,par}$ in increasing order and associating it with a cumulative distribution function (CDF) to produce a list ordered from 0 to 1. Any of the $\chi^2_{\nu,par}$ that have a CDF value greater than 0.8 are cut. This eliminates the upper 20% of $\chi^2_{\nu,par}$. In total, 0.8$\times$1600 traces = 1280 fits will pass this cut. The peak position (x_{max}, y_{max}) of each of those fits on the detection board and the error on that peak position, Δz_{max}, are used for later analysis.

4.4 Excluding CCDs

The aerogel's aluminum frame and the tile holder obscure the path of some of the Cherenkov photons when one is scanning near the edges. The Cherenkov photons should be produced almost uniformly throughout the ∼10 mm aerogel thickness. However, those produced when the beam passes close to the tile edge and the frame can get absorbed by the frame or scatter off of it. In Fig. 4–5 and Fig. 4–6, the electron beam passes through the top edge of the aerogel tile. The upper portion of the Cherenkov ring is blocked by the frame and will not reach the CCDs. The lower CCDs still record their typical Cherenkov ring profile like CCD 1 in Fig. 4–5. The top CCD (CCD 9) and the three CCDs on either side of it (CCDs 6-12) record very low levels of light with no apparent Cherenkov ring profile structure. These low light CCDs are excluded from the analysis for that point and potentially the entire top row as all of the plots should produce similar results to Fig. 4–2.

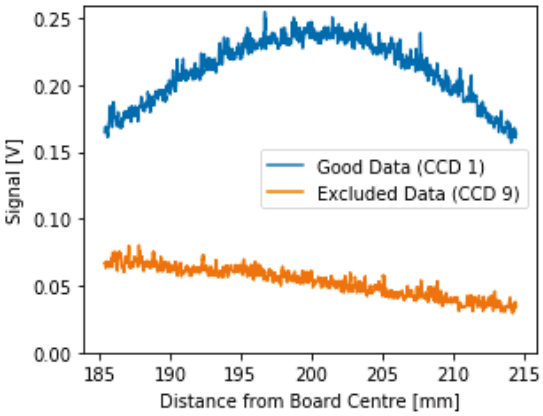

Figure 4–5: An example of CCD readouts from the (x, y) = (50, 95) position of a grid scan showing an acceptable CCD 1 and an excluded CCD 9 from Fig. 4–6.

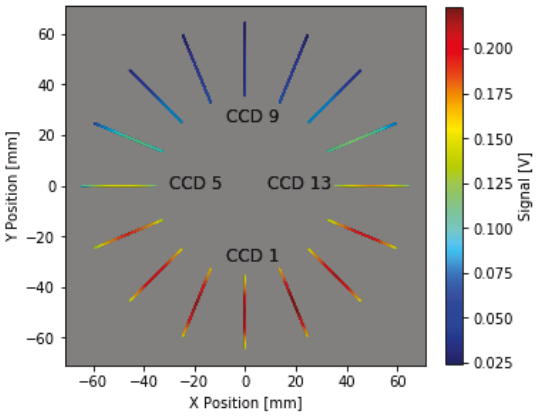

Figure 4–6: Board view of signals with the beam at (x, y) = (50, 95). The Cherenkov light is partially blocked by the aerogel frame.

This poor data is excluded by creating a list of CCDs that should be excluded at each grid scan position. Since this is an edge effect, the list only includes data for the first two or three rows and columns from the tile edges. Each aerogel tile is placed at the same position so, for a given geometry, the list of CCDs that should be excluded

for a specific position should be the same. These excluded CCDs have been verified by more analytical means. One of these methods is the mean signal since it will be much lower for excluded CCDs than those with light, as shown in Fig. 4–6.

4.5 Fitting Data to a Circle

After the last analysis step, the data consists of the x-y positions on the board of the pixels where the Cherenkov ring peaks for every readout of each CCD. The data is filtered by the $\chi^2_{\nu,par}$ limits. If a CCD is blocked by the frame then all of the points belonging to that CCD are excluded from the circle fit for that run. This smaller data set is fit with a circle of radius r and centre position (x_c, y_c) using the *iminuit* [53] minimization package to minimize

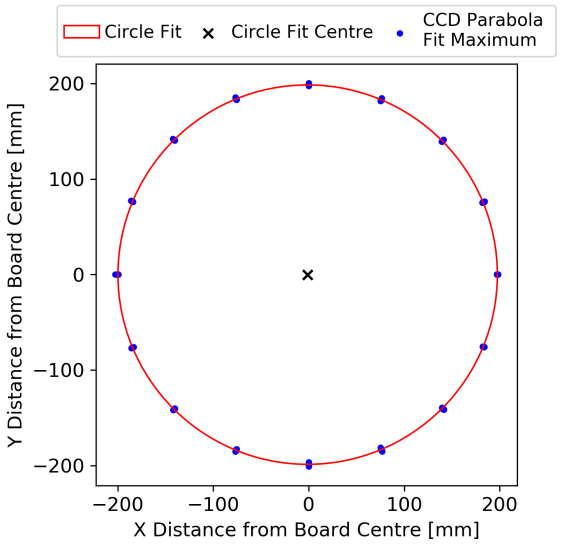

Figure 4–7: A circle fit to the CCD readouts to determine the Cherenkov ring radius. The blue points are the parabolic fit maxima of the CCD data, the red circle is the fit to those points with the centre marked by the x.

$$\chi^2_{circle} = \sum_i \left(\frac{r - \sqrt{(x_{max,i} - x_c)^2 + (y_{max,i} - x_c)^2)}}{\Delta z_{max,i}} \right)^2 , \tag{4.7}$$

which is a sum over the readouts from all CCDs that passed the $\chi^2_{\nu,par}$ cuts. Fig. 4–7 is an example of matching the position of the maximum for each CCD readout's parabolic fit to its physical position on the board. *iminuit* fits those points with a circle that represents the Cherenkov ring position. The radius of the circle and its uncertainty are necessary to then calculate the refractive index.

4.6 Calculating the Refractive Index

The final step in the analysis for a single data point is to convert the calculated Cherenkov ring radius to the refractive index. For the data set in this example, the

aerogel-CCD distance is $d = 278 \pm 1$ mm. There is a half-thickness of $z_e = 5$ mm, an air refractive index of $n_0 - 1 = 3 \times 10^{-4}$ and $\beta \approx 1$ for E = 35 MeV. The radius for this example data set is $r = 198.6 \pm 0.1$ mm based on the circle fit from the previous section. The refractive index n is calculated by using Eq. 3.2 to get the Cherenkov cone angle θ_c and then applying θ_c to Eq. 2.4 to get n.

At the time of writing, a full determination of the systematic uncertainties are still ongoing. As such, the uncertainty on the aerogel surface to CCD distance is stated as $d = 278 \pm 1$ mm, for this specific example, which was calculated by measuring various distances in the system as discussed in Appendix B. An exact systematic uncertainty for z_e for use in the analysis has not been agreed upon yet. Systematic uncertainties for d and z_e are not incorporated into the analysis yet, but they are discussed in Chapter 5. It is also important to note that this data analysis procedure and the Geant4 simulations presented in Chapter 5 assume that the electron beam is perpendicular to both the aerogel tile faces and the CCD detection plane. Realistically, it is possible that the beam is at some small angle with respect the system. Future analysis into sources of systematic uncertainty should explore the effect to determine the possible contribution from the electron beam alignment.

The statistical uncertainty on the refractive index, Δn, is calculated by building a normal distribution of r where $\mu = r$ and $\sigma = \Delta r$ and calculating n for each value in that distribution. This produces another normal distribution where $\mu = n$ and $\sigma = \Delta n$. For the example in this section, $n = 1.154$ and the statistical error is $\Delta n = 1 \times 10^{-4}$, which results in $\Delta n / n_{stat} = 9 \times 10^{-5}$. These values will vary depending on the tile and the position on the tile, but should be similar. This relative statistical uncertainty is well within the required resolution of $\Delta n / n = 7 \times 10^{-4}$. The overall measurement uncertainty will be dominated by systematic uncertainties, which are still under investigation, with a small contribution from statistical uncertainties.

4.7 Producing Refractive Index Maps

A full aerogel calibration scan involves a grid with 19×19 = 361 positions separated by 5 mm on the tile's inner 90×90 mm^2. The analysis procedure is used to calculate the index n at each of these points. The final data product of this analysis is the position of the beam on the aerogel face and the refractive index at that position. The colour map is a way of visualizing these final (x,y) position and index arrays.

Fig. 4–8a is a colour map of the refractive index made by repeating the analysis for all the grid scan point. There is more variation in the index near the tile edges, which coincides with where more CCDs are excluded due to the frame edge blocking the photons. The accuracy of the radius measurements and refractive index decreases where more CCDs are excluded. There are a few points where the fit failed (dark blue) due to bad data or a computation error. Each of these refractive indices are entirely independent measurements, and overall they show that the refractive index is smoothly varying within the expected refractive index range.

Fig. 4–8b is a two-dimensional fourth-order polynomial fit to the data which helps to soften the sudden changes in refractive index near the tile edges and estimate the refractive index where the analysis failed. The model fit is important for those points where the fit failed or near the tile edges where CCDs were excluded from the fit. Fig. 4–8c is the residual plot of the model and the fit. As expected, the largest variation from the model map fit is at tile edges and where fits failed.

32 of the 36 tiles in the RICH will be aerogel while the 4 in the corners are NaF. After this analysis, each of those aerogel tiles will be associated with a grid of refractive index measurements covering the face of a tile. During the HELIX data acquisition, when the RICH detector records a cosmic ray, the refractive index at the closest measured point is used to calculate β and the mass. Therefore, it necessary to understand how changes in the calibration system parameters can change the refractive index and, in turn, the calculated cosmic-ray velocity β.

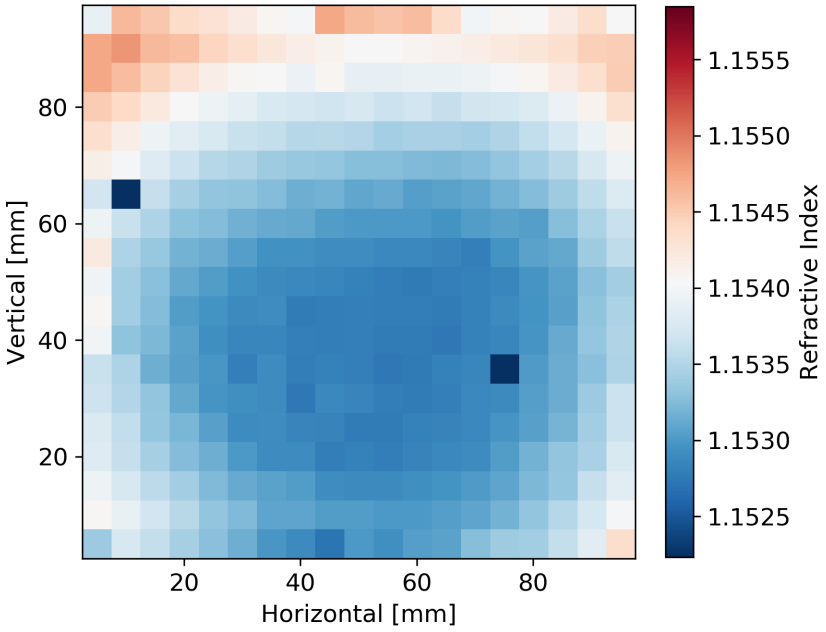

(a) Calculated data map.

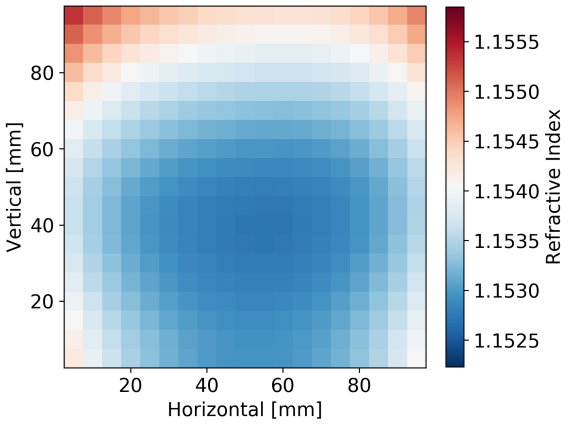

(b) 2D polynomial fit to data.

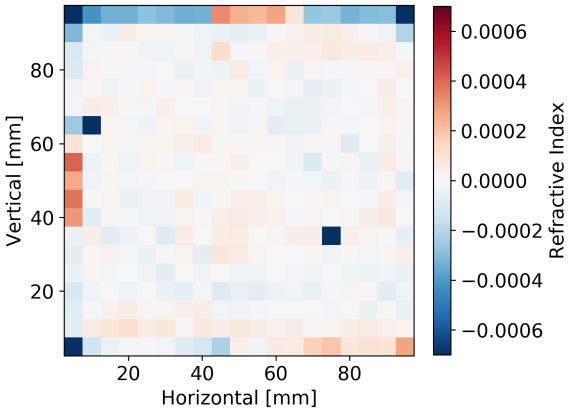

(c) Residuals from the data fit.

Figure 4–8: Refractive index maps for a single aerogel tile at all of the grid points. (a) is the output data from the analysis procedure. (b) is a 2D 4th order polynomial fit over all of the data. Assuming the index varies smoothly, the fit helps to eliminate sudden variations and to provide an estimate of the index for failed fits (dark blue) in (a). (c) is the residual map calculated as (data-fit)/fit to show how the model differs from the data. The tile edges where multiple CCDs are excluded and random fits failed are the most affected. Initial plots generated by Ste O'Brien.

CHAPTER 5
Exploring Aerogel Scan Systematic Uncertainties

The HELIX index resolution goal, $\Delta n/n$ = 0.07 %, is affected by the statistical uncertainty described in Section 4.6 and systematic uncertainties. The aerogel calibration system aimed to limit sources of systematic uncertainty. Differences between the real detector and the model from [41] will introduce uncertainty in the measurements. There is a limit to how much uncertainty is allowable to achieve $\Delta n/n$ = 0.07 %. This chapter will focus on exploring the properties of the electron beam and calibration system and their effect on the refractive index and β.

5.1 Simulating the Cherenkov Ring with Geant4

Geant4 simulations are useful to explore properties that are difficult to do in the real setup. For the calibration system, it is used to understand how the electron beam properties affect the Cherenkov ring. The initial simulation for this section was adapted from code written by R. Prechelt, a HELIX graduate student at the University of Chicago [41]. Some parameters were modified to match the aerogel calibration system setup and the linac beam properties. See Fig. 5–1 for a sample of the simulation display.

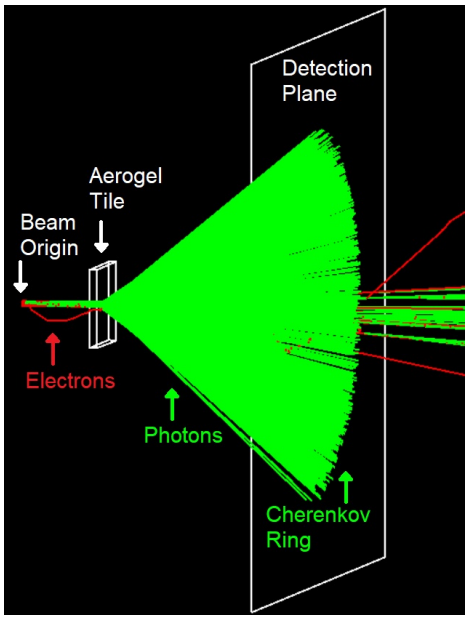

Figure 5–1: Geant4 simulation of the calibration system. Electrons (red) generated before the tile produce Cherenkov photons (green) in the aerogel, which are projected on a detection plane after the tile.

5.1.1 Simulation Setup

The simulation begins with a two-dimensional Gaussian shaped electron beam with $\sigma_{x,y}$ = 2.0 mm. This beam profile is based linac beam profile monitor measurements. The electron beam diverges; electron tracks are assigned angles pulled from a normal distribution with $\mu = 0°$ and a divergence $\sigma = 1.1°$, which is discussed in Section 5.1.3.

The aerogel is a $100\times100\times10$ mm^3 tile and the beam passes through the square faces. The entry face of the aerogel is placed 100 mm after the beam origin, perpendicular to the beam axis. The Cherenkov photons are produced uniformly through the 10 mm thick tile. When the photons reach the exit face of the aerogel tile, they refract at the aerogel-air interface, as shown in Fig. 3–1. The aerogel density is assigned $\rho = 531$ kg/m^3 at $T = 295$ K and $P = 101325$ Pa, based on an example of HELIX's aerogel density. The detection plane is a 0.5×0.5 m^2 board placed $d = 278$ mm from the exit face of the aerogel tile and perpendicular to the beam.

The entire system is in air with $n_0-1=3\times10^{-4}$. Unless otherwise stated, $n = 1.155$ and the half-thickness $z_e = 5$ mm. With these parameters in Eq. 3.2, the Cherenkov ring radius is 197 mm. The simulation parameters are set to match the real beam calibration setup as close as possible. The simulation records the position and energy of photons and electrons on the detection plane. A typical simulation consists of 10000 electrons, producing $\sim1.6\times10^6$ photons.

5.1.2 Analyzing Geant4 Results

The Geant4 photon coordinates correspond to the horizontal and vertical distance from the board centre, in mm, which is also the central electron beam axis. Based on the system setup, the Cherenkov ring on the detection plane should be azimuthally symmetric. Due to this symmetry, if there were CCDs, they would all record the same signal so the simulated photons are written in terms of the distance from the board centre $D^2 = x^2+y^2$ to describe the radial profile.

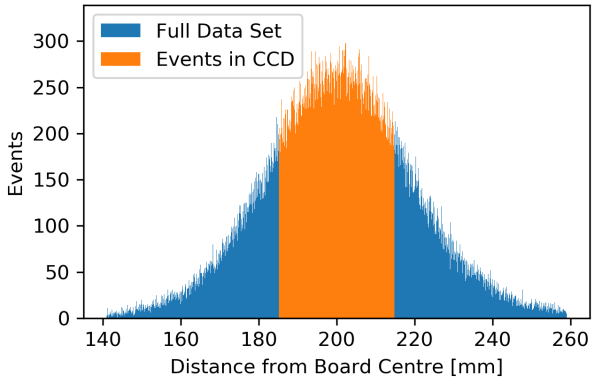

Figure 5–2: Plot of the full simulation photon distribution (blue+orange) to the distance range covered by the CCD pixels (orange). Bins have the same size and position of the real CCD pixels.

In the histogram in Fig. 5–2, the bin width and position exactly correspond to the theoretical position of the pixels in the real CCDs in orange according to Eqs. 4.1-4.3. It also shows the overflow of photons not detected by the CCD in blue. The distance, CCD pixel positions and general aerogel and beam parameters are the same between the beam test data and the simulated data. Therefore, it should be possible to compare these data sets to determine how beam properties affect the resulting Cherenkov ring, a task that would be impossible to test in the real system.

5.1.3 Determining the Beam Divergence for Geant4

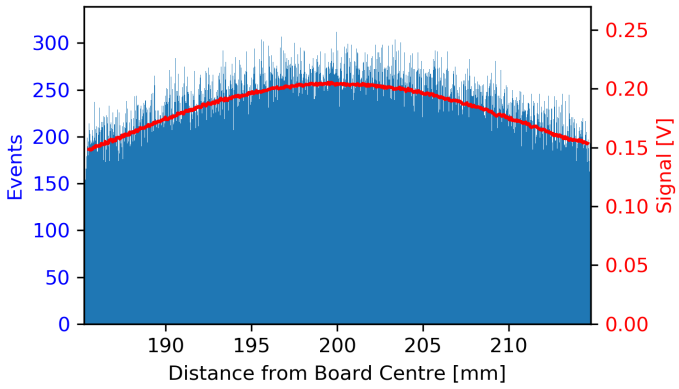

Figure 5–3: Comparing Cherenkov ring data on a single CCD with an unknown n (red fit) and a Geant4 simulation result for $n = 1.155$ aerogel (blue histogram).

Knowing the divergence of the electron beam is necessary to compare the real beam data to the simulation. The simulated Cherenkov ring without divergence is much thinner than what is observed experimentally so the divergence stretches the Cherenkov ring so they have the same profile. Fig. 5–3 is a real data set which was fit with a Gaussian with $\sigma = 18.7$ mm. The simulation was run for multiple divergences until the width of the Cherenkov ring produced was similar to σ for the real data. When the divergence was set at 1.1°, the fit to the simulation had the same width as the data, $\sigma = 18.7$ mm.

The CCD readout sample and the closest Geant4 equivalent data set are given in Fig. 5–3. The distance is the same in the real and simulated data sets, but Geant4 has a known $n = 1.155$ while, for the real data set, $n = 1.154$ with a statistical uncertainty of $\Delta n/n_{stat} = 9\times10^{-5}$, as calculated in Chapter 4. Based on the refractive index difference alone, the peaks of the distributions are not expected to be close but

not perfectly aligned. The beam divergence helps to adjust the simulation to model the real setup. This does not mean that the beam divergence of the NRC linac is actually 1.1°. Rather, the width of the simulated Cherenkov ring with this divergence and the starting beam profile most closely resembles the width of the data fit.

5.1.4 Contributions to the Cherenkov Ring Width

The divergence, explored in Section 5.1.3, is not the only contribution to the Cherenkov ring width. However, with the aerogel calibration system, it is difficult to discern if the observed width is from beam divergence or other physical processes. This study explores how the Cherenkov ring width, and general shape, change depending on the physical electron processes involved. In the Geant4 simulation, there are three electron processes: ionization, bremsstrahlung and multiple scattering. Divergence and multiple scattering are expected to be the principal contributors to the width since divergence is required to match the data Cherenkov ring width. For multiple scattering, the effect decreases with increasing energy. At $E = 35$ MeV, multiple scattering could significantly contribute to the profile width. Looking into these factors is perfectly suited to Geant4 where they can be carefully controlled.

Fig. 5–4a is the base case, with the parameters described earlier, where there are no electron processes or beam divergence. The only contributions to the Cherenkov ring shape are photon processes like absorption, Rayleigh scattering and Compton scattering, and the two-dimensional $\sigma = 2$ mm Gaussian beam. A Gaussian fit to the Cherenkov ring gives a width of $\sigma = 2.7$ mm.

When ionization and bremsstrahlung are introduced (Fig. 5–4b), the Cherenkov ring is wider with $\sigma = 2.9$ mm, which is mainly due to the wider range of energy of electrons. Simulations with only ionization showed that this small shape change is due almost entirely to ionization and not bremsstrahlung. A second simulation was run to measure the energy of the electrons exiting the aerogel to determine the energy loss, as shown in Fig. 5–5. With no electron processes, the electron energy remained

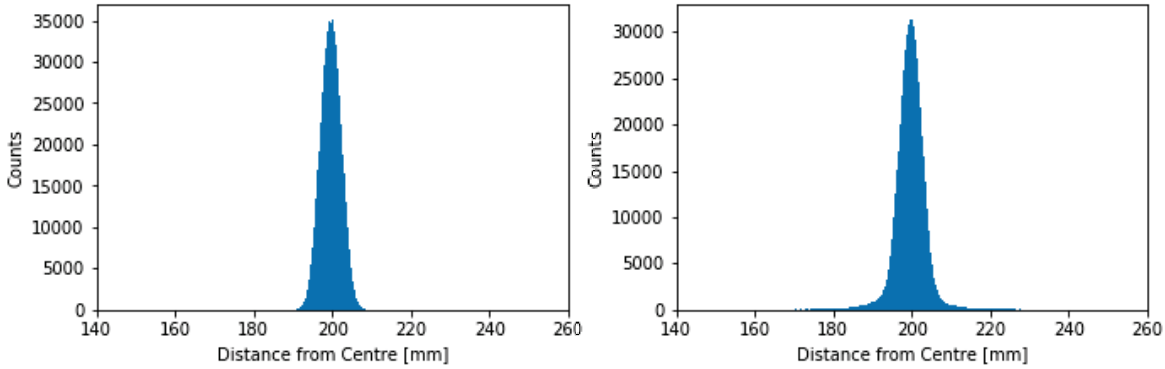

(a) No electron processes

(b) Ionization and bremsstrahlung

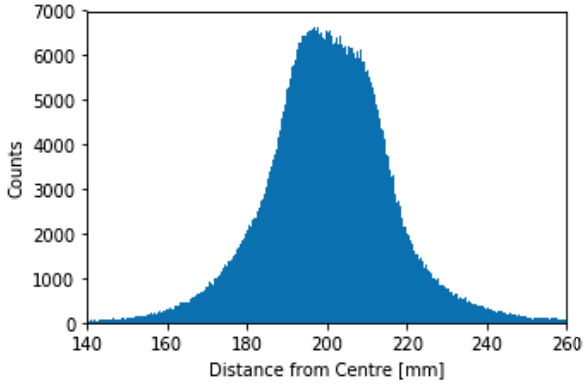

(c) All electron processes

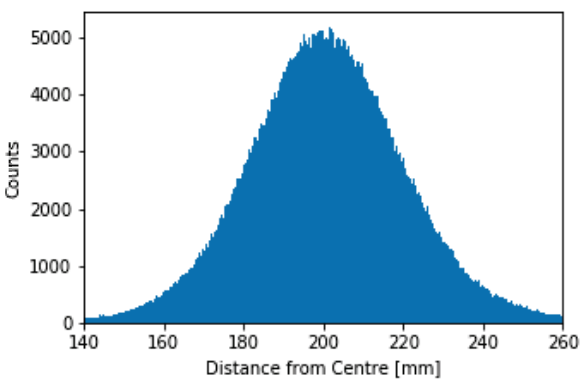

(d) Electron processes + divergence

Figure 5–4: The Cherenkov ring from Geant4 simulations with different electron physical processes. (a) does not include any electron processes or divergence, (b) adds ionization and bremsstrahlung and (c) adds multiple scattering. (d) includes all three electron processes and beam divergence.

at 35.0 MeV, but with ionization, the weighted mean of the distribution decreases to 33.6 MeV with a skew towards lower energies, producing a wider energy range. Adding bremsstrahlung and multiple scattering does not change the shape of the distribution although it decreases the mean energy to 32.3 MeV. Since the Cherenkov cone angle gets smaller with decreasing velocity, the wider energy range produces a wider distribution of Cherenkov angles. This produces a wider Cherenkov ring and introduces some asymmetry from the skewed energy distribution towards smaller radii. The electron energy distribution with added bremsstrahlung and multiple scattering does not change its general shape or significantly shift its position. Thus, the width observed in Fig. 5–4d is not due to the electron energy change.

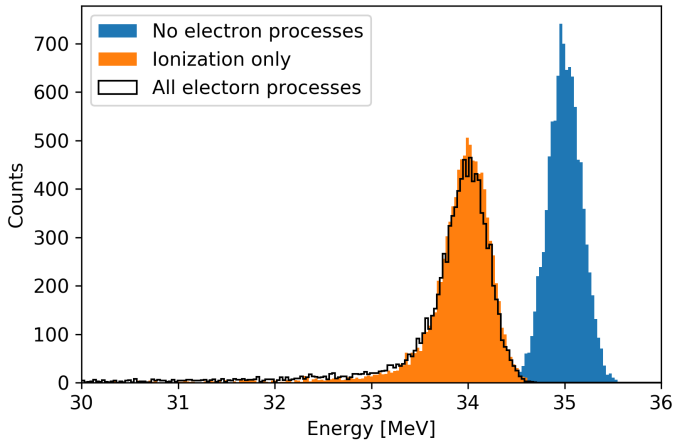

Figure 5–5: The energy of electrons at the aerogel exit face. The no-processes case is a symmetric distribution while adding ionization changes the energy of the electrons and skews it towards lower energy. Bremsstrahlung and multiple scattering do not significantly impact the electron energy.

Fig. 5–4c adds multiple scattering to the data from Fig. 5–4b. This process results in a significant change to the width of the Cherenkov ring as well as some additional asymmetry in the shape. The Cherenkov ring width increases to σ= 13.3 mm compared to 2.9 mm without multiple scattering. Multiple scattering is an elastic process so the energy of the electrons does not change, but the angular distribution of electrons changes. The analysis is based on the idea that, on average, the electron and Cherenkov cone axis should be perpendicular to the aerogel face. If electrons are scattered at different angles from that axis then the Cherenkov cone will be at an angle. With the refraction off the aerogel-air interface, the off-axis Cherenkov ring will refract off that interface with different angles. These effects introduce a wide angular distribution to Cherenkov cones which will produce an overall wider Cherenkov ring on the CCDs and it could also account for the asymmetry.

Fig. 5–4d includes all three electron processes and the 1.1° beam divergence to match the real data width. Like multiple scattering, beam divergence increases the angular distribution of electrons producing off-axis Cherenkov cones. This leads to a wider overall Cherenkov ring. Adding divergence increases the ring width from

$\sigma = 13.3$ mm to 18.7 mm. This does assume that photon and electron processes and beam divergence are the only contributions to the Cherenkov ring width.

All of the plots in Fig. 5–4 have the same binning and same number of simulated electrons. Therefore, the difference in the height of these distributions is representative of the intensity of light reaching the detection board. Between the case with no electron processes (Fig. 5–4a) and the one with all processes and divergence (Fig. 5–4d), the peak intensity of the light decreases to 1/7 of its initial value.

5.1.5 Cherenkov Ring Width Dependence on Aerogel Tile Thickness

One effect on the Cherenkov ring width that has not been considered yet is the aerogel tile thickness. To explore this effect, the Geant4 simulation was run with different thicknesses while keeping all other variables the same as previous simulations including $d = 278$ mm, $n = 1.155$, $\sigma = 2$ mm Gaussian beam and 1.1° beam divergence.

As shown in Fig. 5–2, real CCD data is limited to only a portion of the full Cherenkov ring profile. In the CCD distance range, the Cherenkov ring profile does not show the standard Gaussian structure so it is simpler to fit with a parabola. The Geant4 simulation for the thickness test will appear as a full Gaussian-like distribution like Fig. 5–2. Due to the overall Gaussian-like shape in this wider distance range, the σ of the Gaussian fit is treated as the Cherenkov ring width. Fig. 5–6 shows the change in the Cherenkov ring width σ as a function of tile thickness.

The ring width increases with thickness due to the amount of material the electrons go through. The Cherenkov photons are generated uniformly throughout the aerogel. For $n = 1.155$ aerogel and electrons with $E = 35$ MeV, the Cherenkov cone angle is 30°. A Cherenkov cone generated near the entry face will always be larger, at a given position, then one generated later. This introduces an aberration from all of the different radii contributing to the detected ring. The Cherenkov ring width and the tile thickness are related by $r_0 = z_0 \tan\theta_c$, replacing the z_e in Fig. 3–1

with the total tile thickness z_0. For z_0=10 mm, the Cherenkov ring width due to aberration is r_0=5.8 mm while for z_0=5 mm, r_0=2.9 mm.

The Cherenkov ring width is approximately linear with tile thickness. A linear fit to the data has a y-intercept of 13.1 mm. Based on this intercept, a very thin piece of aerogel the Cherenkov ring would still have a finite width that must come from other contributions. Based on the studies in Section 5.1.4, the electron beam properties such as the initial beam width, electron processes and beam divergence are the most significant contribution to the Cherenkov ring width. Therefore, a thinner aerogel tile would decrease the Cherenkov ring width, but the decrease is limited by the contribution of electron processes and beam divergence.

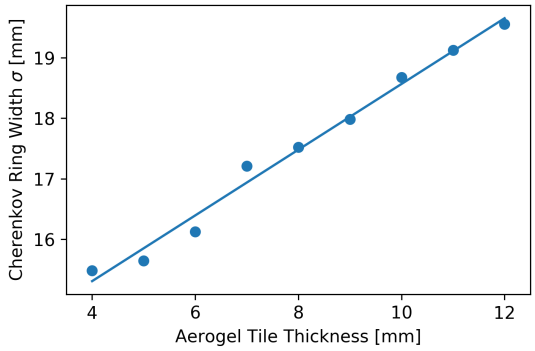

Figure 5–6: The effect of changing the aerogel tile thickness on the Cherenkov ring width. The width of a Gaussian fit to the Cherenkov ring profile increases linearly with the tile thickness.

The number of photons changes with tile thickness according to Eq. A.1 in Appendix A. In a thicker tile, there are more opportunities for electron interactions with the aerogel to produce photons. The Geant4 simulation produces ∼16 photons/mm/electron in the aerogel tile. The wider 10 mm thick aerogel tile is used in HELIX to maximize the CCD signal at the expense of having a wider Cherenkov ring with the associated ring fitting difficulties.

5.1.6 Calculating the Refractive Index of Simulations

Most of the studies done with Geant4 in this section do not depend exactly on the index output. They depend on the relative trends in the width and features of the Cherenkov ring that can be used to explore parameter spaces that are difficult with the real beam. For completeness, it is important to explore what n_{output} is calculated, when the exact n used for the simulation, n_{input} = 1.155, is known.

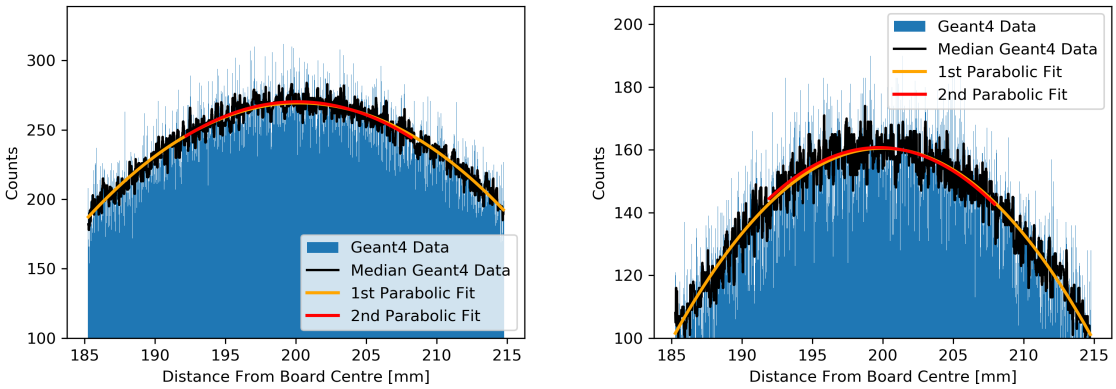

(a) Typical simulation, 10 mm thick, all electron processes.

(b) 5 mm thick aerogel tile, all electron processes

Figure 5–7: Calculating n for a Geant4 simulation with $d = 278$ mm, $z_e = 5$ mm and $n_{input} = 1.155$ and analyzed with the two pass parabolic fit. (a) is the full realistic beam width fit for the typical 10 mm thick tile while (b) is the fit for a thinner distribution from a 5 mm thick tile.

For this study, the simulation parameters are used including $n_{input} = 1.155$. Assuming, for now, that d and z_e do not have any uncertainties, any difference in n_{output} to n_{input} should be due to the Cherenkov ring shape and the fitting function. The simulated Cherenkov ring was put into bins corresponding to the size and position of the CCD pixels and analyzed using the procedure from Chapter 4. This includes the 11 pixel median filter and the two-pass parabolic fit. n_{output} is calculated with Eq. 3.2 with the known d, z_e and the peak of the fit, as shown in Fig. 5–7a.

If the peak of the first parabolic fit was used as the radius to calculate the output index then it would be $6{\times}10^{-4}$ above n_{input}. The second fit improves the accuracy so the index is $4{\times}10^{-4}$ over n_{input}. From this result, it is clear that there is a certain amount of error associated with fitting a Cherenkov ring with this width. For HELIX, the allowed uncertainty is $\Delta n/n \leq 7{\times}10^{-4}$ so this shift from the true input refractive index is significant. Ideally, $n_{output} = n_{input} = 1.155$ and instead it is higher. This difference could be due to a combination of the fitting technique and the Cherenkov ring width.

To determine if the Cherenkov ring width was responsible for the poor fit, the same analysis was applied to a 5 mm thick tile in Fig. 5–7b. The effect of the tile thickness on the Cherenkov ring width is discussed in Section 5.1.5, however, in this section, the thinner tile is only used to determine if the thinner Cherenkov ring will improve the fit quality. The two-pass parabolic fit was applied which produced a calculated refractive index over the input n_{input}=1.155 of $n_{output} - n_{input} = 5\times10^{-5}$. In comparison, the wider Cherenkov ring has $n_{output} - n_{input} = 4\times10^{-4}$. Both cases had $\chi^2_\nu = 0.13$. Therefore, the Cherenkov ring width is a major contributor to how accurately the two-pass parabolic fit can determine the refractive index.

The difference between $n_{input} = 1.155$ and n_{output} is dominated by the width of the Cherenkov ring. The width alone can shift the calculated refractive index. This is assuming that the distance, thickness and CCD positions are all perfectly accurate, but in reality these measurements have uncertainties.

5.2 Effect of Parameter Variations on the Refractive Index

This section focuses not on simulations, but on manipulating the equations used during data analysis. Eq. 3.2 and Eq. 2.4 are used to calculate n from the Cherenkov ring radius r, which is based on d and z_e. If d and z_e are not exactly the same as the values for the aerogel and the system, then this will introduce systematic uncertainties. In this section, we will alter d and z_e in Eq. 3.2 and Eq. 2.4 to determine the largest variations which will still result in $\Delta n/n$ <0.07 %.

The basic parameters used are $r = 200.0$ mm, $z_e = 5.0$ mm, $\beta \approx 1$ for $E = 35$ MeV electrons and $n_0-1=3\times10^{-4}$. The initial distance between the aerogel tile and the CCD plane is 278.6 mm as that is the distance where the base $n = 1.155$ results in a $r = 200.0$ mm Cherenkov ring.

5.2.1 Distance d Variations

To simulate the change in the refractive index if the distance was measured incorrectly, the refractive index was calculated above and below the ideal distance of

278.6 mm in 1 mm intervals. This is the situation where the radius is $r = 200.0$ mm and $z_e = 5.0$ mm, but the distance is not correct. If it were set to $d = 278.6$ mm, the refractive index would be 1.155. The blue points in Fig. 5–8 show the results of using those distances with Eq. 3.2 to calculate the refractive index compared to the true refractive index given by the black dashed line.

The second test incorporated into this plot is the deviation in d at the limits of $\Delta n/n$. For an $n = 1.155$ aerogel and $\Delta n/n = 0.07\%$, $\Delta n = 8{\times}10^{-4}$ mm. The plot includes this limit in red above and below $n = 1.155$. These lines represent the maximum deviation from the true refractive index that would still be within 0.07% systematic shift in the refractive index. This does not incorporate uncertainties on r and z_e.

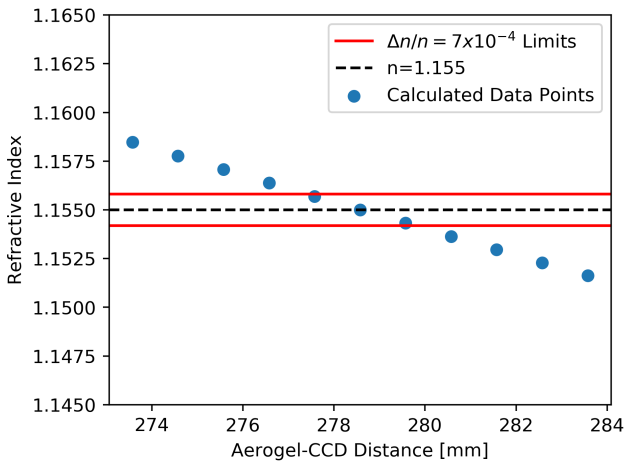

Figure 5–8: The change in refractive index due to an incorrect measurement of the aerogel-CCD distance for a 200.0 mm radius Cherenkov ring and a $n = 1.155$, 10.0 mm thick aerogel tile.

Rearranging the equation to find the distance where the refractive index reaches the two red limit lines results in $\Delta d_{\pm}{=}d_{\pm}{-}278.6$ mm$=\mp 1.2$ mm. This is just a simple example to show that if the distance is not measured with uncertainties less than approximately 1.2 mm, then the refractive index will be too far off of its required resolution for HELIX's target sensitivity. Therefore, the overall uncertainty must be within these limits since r, z_e and d each have their own uncertainties.

5.2.2 Half-Thickness z_e Variations

The aerogel tile is not always 10.0 mm thick, as it is usually assumed to be, and it is not necessarily constant across the aerogel tile. The thickness was measured at TRIUMF, using a coordinate measuring machine, for all of the tiles and showed that

the aerogel tile thickness ranged from 9.4 mm to 10.0 mm. These scans also showed that the aerogel faces were not completely flat like Eq. 3.2 assumes. They actually have slightly parabolic shapes.

Fig. 5–9 follows the same procedure as Fig. 5–8 except that it involves a change in the half-thickness z_e between 4.0 mm and 6.0 mm. d is fixed and r is recorded for different values of z_e which is converted into n. The limits of the allowed refractive index resolution correspond to a z_e variation of $\Delta z_{e,\pm}$=$z_{e,\pm}$−5.0 mm=$\mp$ 1.5 mm. At $\Delta d_\pm = \mp 1.2$ mm, the allowable distance error is similar to $\Delta z_{e,\pm}$=$\mp$1.5 mm, but the relative error is very different, 1.2/278.6 = 0.5 % for the distance compared to 1.5/5.0 = 29.0 % for z_e.

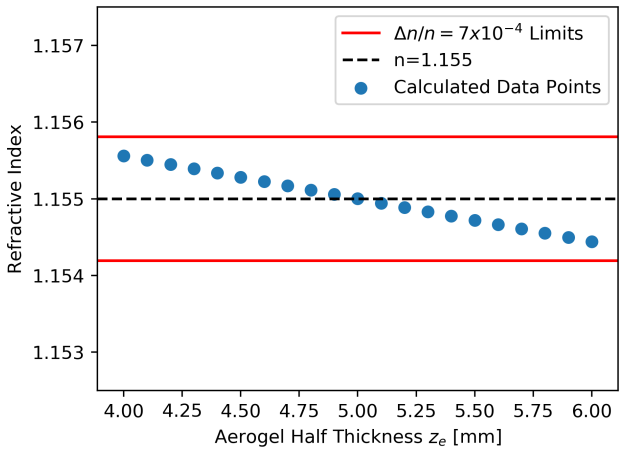

Figure 5–9: Variations in refractive index n due to the half-thickness z_e with r = 200 mm, d = 278.6 mm. The standard n = 1.155 is in black and the n resolution limits are in red.

Based on the TRIUMF thickness measurements, z_e might be 0.3 mm smaller than expected, which is well within the 1.5 mm maximum uncertainty allowance. According to these calculations, Eq. 3.2 is less sensitive to changes in z_e than in d. Going forward in the analysis, it should not be assumed that the thickness is always 10 mm as that will unnecessarily introduce errors into the index. The TRIUMF thickness maps of the aerogel tiles were done along the same coordinates as the scan so they can be used to correct z_e.

5.3 Distinguishing Isotopes with Refractive Index and Rigidity Variations

This study looks at the wider HELIX experiment and how the errors introduced from refractive index measurements affect the ability to distinguish between Be

isotopes. The DCT rigidity, R, and the TOF/RICH velocity, β, measurements are related to the particle mass by Eq. 2.3 where the charge $Z = 4$ for Be. A more useful form of this equation is

$$\beta = \left(\left(\frac{mc^2}{ZeR} \right)^2 + 1 \right)^{-\frac{1}{2}} , \tag{5.1}$$

which uses a specific R, m and Z. This is the parameter space of HELIX so it is useful to plot the expected β for many R for both Be isotopes to understand where measurements should fall in this space. It also helps to understand how changing some parameters can alter where the curves appear in this space and even how the curves get wider and more indistinguishable when uncertainties are introduced.

5.3.1 Adding Variations to the Refractive Index and Rigidity

The first panel of Fig. 5–10 simply uses Eq. 5.1 for the two isotopes. It is assumed that ^{9}Be and ^{10}Be have masses of 9 amu and 10 amu, respectively. Converting amu to GeV/c^2, the isotope masses become 8.38 GeV/c^2 and 9.32 GeV/c^2. β is calculated for a range of rigidities for both isotopes. One of the principal goals for HELIX is to distinguish ^{9}Be and ^{10}Be. This is possible if the β and R measurements clearly fall closer to one of the isotope curves. The greater uncertainty there is in these two parameters, the wider these curves will appear which will make it hard to associate a measurement definitively with either ^{9}Be or ^{10}Be.

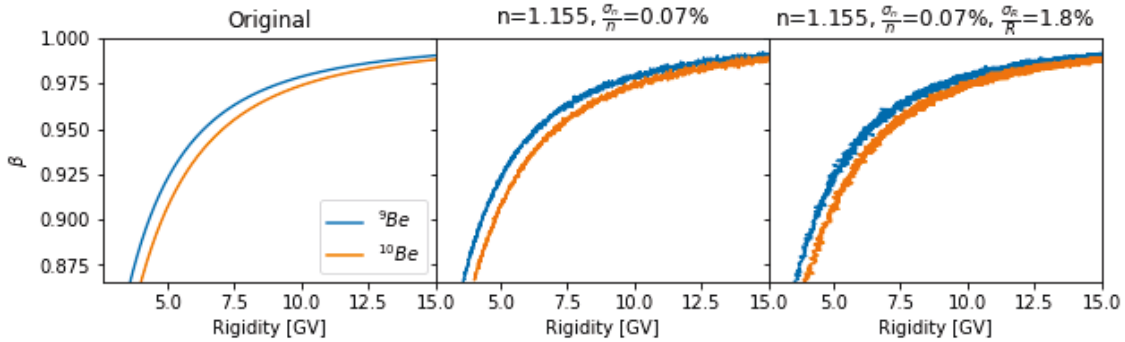

Figure 5–10: Effect of refractive index n and rigidity R variations on distinguishing ^{10}Be and ^{9}Be according to Eq. 5.1. Left: The original plot of R and β. Middle: Added variation in input n, but analyzing as a constant n to find β. Right: n variations and additional R variations on the scale of the HELIX DCT uncertainty.

The middle panel in Fig. 5–10 considers what happens with variations in n. The goal for HELIX is for $\Delta n/n \leq 0.07$ %. To determine the effect of n on the left panel and Eq. 5.1, the β calculated is put through $\cos\theta_c = 1/(n\beta)$. The n used here is pulled from a normal distribution with $n = 1.155$ and $\sigma_n/n = 0.07\%$ to represent the n variations in the tile measurements. This results in a smeared θ_c distribution which then goes back through the equation to recalculate β. During the analysis, n is assumed to be constant. This should give a more realistic aerogel model where there are n variations that propagate to β. The 'smearing' affects the curve thickness, but at lower β there is still good distinguishing power between the two isotopes. The smearing makes it difficult to distinguish the isotopes near $\beta = 1$. In a full plot, there should be a geometric factor, $\Delta\theta\tan\theta$ from Eq. 2.6, included in the uncertainty in the calculation of β and its uncertainty, which has not been included here. That would increase the uncertainty to 1%.

The right panel of Fig. 5–10 involves the same process as the middle panel except that there is also an R variation. HELIX's rigidity resolution $\Delta R/R$ as a function of R ranges between 0.01-0.04 up to $R = 30$ GV [26]. To simplify the calculation, $\Delta R/R$ is set constant at 1.8%, the rigidity resolution allowance for HELIX. R is picked from a normal distribution with the mean at the input R and $\sigma_R = \Delta R$ which introduces horizontal smearing in R. This smearing means that moderate β data, where the isotope curves were still distinguishable with only n variations, are now harder to distinguish due to the R variations.

It will be more difficult to distinguish the Be isotopes with an uncertainty in n and R. Although this is an obvious conclusion, it is shown clearly in the two smeared overlapping curves in Fig. 5–10. However, the values for the uncertainties are based on the allowed resolution to still achieve the 2.5% mass resolution. Even with the uncertainties, up to $R = 15$ GV [26], it should still be possible to distinguish ^{10}Be from ^{9}Be to the four-sigma goal even including the geometric factor to β.

5.3.2 Comparing Precision and Accuracy in Index Measurements

The main purpose of these plots is to check whether it is more important for the β-R curves to be accurate around the true value or precise with low uncertainty. Ideally both would be true. This study generates data in the same way as the middle panel of Fig. 5–10, introducing a $\sigma_n/n = 0.07\%$ uncertainty in the n of the tile and then either changing that uncertainty or the n used in the analysis to get β from θ_c.

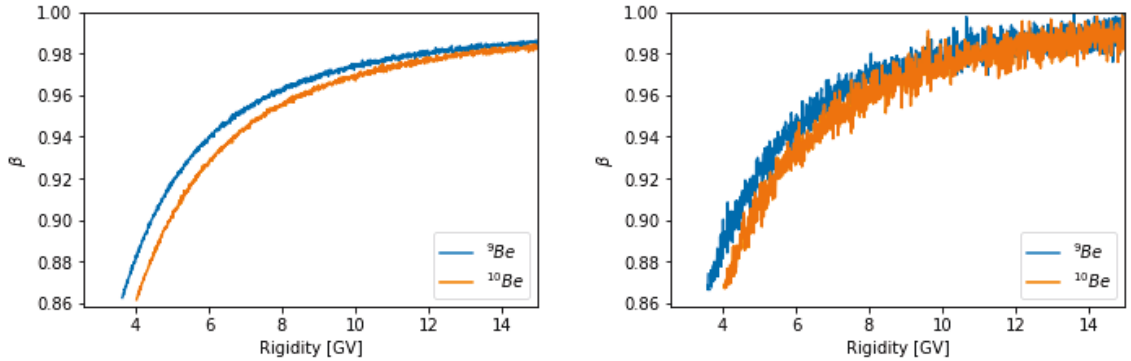

(a) Absolute value of n increased by 0.5 % in analysis ($n = 1.16$), $\sigma_n/n = 0.07\%$

(b) $\sigma_n/n = 0.5$ % variation of the tile n, analyzed as having a n uniform $n = 1.155$.

Figure 5–11: Determining the effect of precise or accurate measurements of n on β. (a) The tile is uniform $n = 1.155$ with 0.07% uncertainty, but it is analyzed with higher n of $n = 1.16$. (b) The case where the tile index has 0.5 % variations from the true n, $n = 1.155$, but it has not been mapped so it is analyzed as a uniform tile.

If the calibration of n is done correctly with the same n used in analysis and 0.07% uncertainties, the resulting β-R plot would look like the middle panel of Fig. 5–10. Consider the case where the n measured during calibration is 0.5 % higher ($n = 1.16$) than the true value ($n = 1.155$) and the higher value is used to analyze data. The measurements of n are precise within the 0.07% n resolution goal. Fig. 5–11a is the result using $n = 1.16$ to analyze data from a tile with $n = 1.155$. This increased n causes the isotope curves to shift β downwards by 0.5 %, compared to the analysis with $n = 1.155$. This shift maintains the relative isotope curve separation, but its absolute β value is incorrect. With this shift, but low uncertainties, it would still be easy to distinguish the two curves and notice that they are not at the correct

β for a given R. Since it is a simple shift, a β correction factor could be applied to the curves to improve the β results so they match the expected mass distribution.

If there was no aerogel tile calibration and the tiles naturally had a 0.5 % n variation distribution, the β-R curves would be like in Fig. 5–11b. The 0.5 % variation is pulled from a normal distribution centred at $n = 1.155$. Without a more accurate measurement, it would be simplest to assume that the tile has a uniform n. For this example, that uniform n is set to match the mean of the distribution, $n = 1.155$. The 0.5 % n uncertainty introduces uncertainty into the β-R curves. Without the colour coding of the two isotopes in Fig. 5–11b, it would be difficult to distinguish the isotope curves enough to definitely identify a measurement as ^{9}Be or ^{10}Be.

Fig. 5–11a is where the relative variations in n extent of the tile are measured precisely, but the overall scale is off by some scaling factor. In comparison, Fig. 5–11b is when the measured n is accurate to the true n of the tile, but it is not precise enough to distinguish isotopes. In this sense, it is better to have a high precision like Fig. 5–11a because the data can be corrected later. With Fig. 5–11b, there is too much noise to distinguish ^{10}Be from ^{9}Be. The focus of all of the n calibration measurements is to have low uncertainties in the measurements and try to get an accurate n. There is the understanding that there are many measurements involved in calculating n, such as the distance d and the position of the CCDs, which could result in a systematic shift observed in all of the data. If these systematic shifts exist, then they can potentially be corrected for in later analysis if β-R does not produce an accurate mass distribution.

CHAPTER 6
Conclusion

The HELIX cosmic-ray experiment is designed to measure the abundances of light nuclei, especially ^{10}Be and ^{9}Be to a mass resolution of $\Delta m/m = 2.5\%$. The HELIX RICH radiator plane is predominantly composed of $n = 1.15$ - 1.16 aerogel tiles. Variations in the refractive index across the tile must be measured across the tile because they are larger than the allowed resolution of $\Delta n/n \leq 0.07$ % due to the aerogel fabrication process.

The purpose of this research was to build a system to make efficient and precise measurements of the refractive index on a grid over the aerogel tiles. This includes details of the final system design, running the system and the analysis procedure. The radius of the Cherenkov cone on a detection plane produced when a linear accelerator electron beam passes through a point on the aerogel is directly related to the refractive index. A full 361 data point scan of the index takes 35 minutes per tile. Analysis is still ongoing, but preliminary results show that this method is capable of detecting smooth refractive index variations across a tile in the expected refractive index range.

The accuracy of the refractive index measurements is dependent on many factors. Electron processes, divergence and the tile thickness produce a wider Cherenkov ring which is difficult to fit accurately. In addition, any deviations from the true values of the radius, the aerogel-CCD distance or the tile thickness, will affect the final calculated refractive index and its uncertainty. Studies showed that even if there are systematic shifts in the refractive index compared to the true value, if the uncertainty is low, it should still be possible to distinguish Be isotopes and calculate ^{10}Be/^{9}Be.

The 50 flight quality aerogel tiles produced for HELIX have all been scanned and analyzed at least once using the discussed calibration system. Further scans and more detailed analysis are planned to fully understand sources of systematic uncertainties and to test result reproducibility.

APPENDIX A: The Cherenkov Effect

In the Cherenkov effect, a charged particle polarizes the nearby atoms in the material asymmetrically [55]. The atoms will relax and emit dipole radiation that moves out spherically, according to Huygens principle, at the phase velocity of the medium [56]. When $\beta < 1/n$ the emitted waves interfere destructively and no light is emitted. At $\beta > 1/n$, they constructively interfere and emit coherent radiation in a cone along the particle path, as shown in Fig. A-1 [56]. The photons are in phase along a line at an opening angle θ_c from the charged particle's direction of travel. Frank and Tamm wrote the quantitative theory of Cherenkov radiation [55] and found that the emission obeyed Eq. 2.4. Since $\cos\theta_c$ is bounded with a maximum of 1, only particles with $\beta > 1/n$ will produce Cherenkov radiation [55].

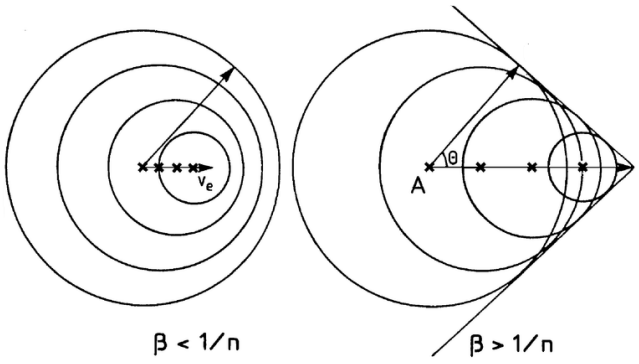

Figure A-1: The Huygens spherical wavelet diagram for a charged particle travelling below (left) and above (right) the phase velocity threshold. The right diagram shows the Cherenkov emission wavefront. Image Credit: [54].

Frank and Tamm also derived the expected number of photons emitted per unit length and wavelength λ [56] and found

$$\frac{\partial^2 N}{\partial x \partial \lambda} = 2\pi\alpha \left(1 - \frac{1}{n^2\beta^2}\right) \frac{1}{\lambda^2} \,, \tag{A.1}$$

where $\alpha = 1/137$, the fine-structure constant.

The photon yield increases when the wavelength decreases leading to the blue-violet colour generally observed for Cherenkov radiation.

APPENDIX B: Distance Calibration

To accurately determine the refractive index, the aerogel-CCD distance d must be known to mm precision over the ~ 300 mm expanse marked in Fig. 3–1. Calculating d involves multiple precise measurements. All distance values are written to the precision of the measuring instruments for this calculation.

The calibration rod is a piece of aluminum machined to have flat parallel ends which was approximately the distance between the backboard that holds the detection board to the aerogel holder base. The rod was measured with calipers as 306.14±0.01 mm. The board z-stage is moved until there is a tight fit between the backboard, the calibration rod and the holder, which occurs when the z-stage is 26.0±0.1 mm from its home position. The horizontal distance from the aerogel face to the base of the holder is 4.00±0.02 mm based on frame measurements. The average distance from the board to the CCD face is 7.78±0.12 mm, measured using calipers. Three washers separate the detection board from the backboard and, on average, each are 1.57±0.03 mm thick, as measured with calipers. The detection board itself was measured also using calipers at multiple points resulting in a mean thickness 1.55±0.02 mm.

The overall distance is 322.1±0.4 mm calculated using

$$d = \underbrace{306.14}_{\substack{\text{Calibration}\\ \text{Rod}}} + \underbrace{26.0}_{\substack{\text{Motor}\\ \text{at Rod Fit}}} - (3 \times \underbrace{1.57}_{\text{Washer}}) - \underbrace{1.55}_{\text{Board}} - \underbrace{7.78}_{\substack{\text{Board}\\ \text{-CCD}}} + \underbrace{4.0}_{\substack{\text{Holder}\\ \text{-Aerogel}}} - \underbrace{\text{z}}_{\substack{\text{Stage}\\ \text{Position}}} \text{ mm.} \quad \text{(B.1)}$$

The board position is adjusted before each scan to center the CCDs, which can alter the z-stage position. For the production run, the z-stage position was between z = 42.0 and z = 48.0 mm (±0.1 mm) making d = 274.1 - 280.1 mm with $\Delta d \approx 0.7$ mm. Δd is likely larger than what is measured so in preliminary analysis it is set to 1 mm. Thus the distance is often written in the thesis to zero significant figures unless the extra precision is required for a theoretical calculation.

REFERENCES

[1] T. Wulf, "Über die in der Atmosphäre vorhandene Strahlung von hoher Durchdringungsfähigkeit," *Phys. Zeit.*, vol. 10, pp. 152–157, 1909.

[2] V. Hess, "Über Beobachtungen der durchdringenden Strahlung bei sieben Freiballonfahrten," *Phys. Zeit.*, vol. 13, pp. 1084–1091, 1912.

[3] V. Hess, "On the Observations of the Penetrating Radiation during Seven Balloon Flights," *arXiv e-prints*, p. arXiv:1808.02927, 2018. Ed. and Trans. by A. Angelis and C. Arcaro, July 2018.

[4] C. D. Anderson, "The Positive Electron," *Phys. Rev.*, vol. 43, pp. 491–494, Mar. 1933.

[5] S. H. Neddermeyer and C. D. Anderson, "Note on the Nature of Cosmic-Ray Particles," *Phys. Rev.*, vol. 51, pp. 884–886, May 1937.

[6] H. Dembinski *et al.*, "Data-driven model of the cosmic-ray flux and mass composition from 10 GeV to 10^{11} GeV," in *35th International Cosmic Ray Conference (ICRC2017)*, vol. 301 of *International Cosmic Ray Conference*, p. 533, Jan. 2017.

[7] M. Tanabashi *et al.*, "Review of Particle Physics," *Phys. Rev. D*, vol. 98, p. 030001, Aug 2018.

[8] J. R. Hörandel, "Models of the knee in the energy spectrum of cosmic rays," *Astroparticle Physics*, vol. 21, pp. 241–265, June 2004.

[9] E. G. Berezhko and L. T. Ksenofontov, "Composition of cosmic rays accelerated in supernova remnants," *Soviet Journal of Experimental and Theoretical Physics*, vol. 89, pp. 391–403, Sept. 1999.

[10] K. Greisen, "End to the cosmic ray spectrum?," *Phys. Rev. Lett.*, vol. 16, pp. 748–750, Apr. 1966.

[11] G. T. Zatsepin and V. A. Kuz'min, "Upper Limit of the Spectrum of Cosmic Rays," *Soviet Journal of Experimental and Theoretical Physics Letters*, vol. 4, p. 78, Aug. 1966.

[12] M. Ackermann *et al.*, "Detection of the Characteristic Pion-Decay Signature in Supernova Remnants," *Science*, vol. 339, no. 6121, pp. 807–811, 2013.

[13] D. H. Perkins, *Particle Astrophysics, Second Edition.*, vol. 2nd ed of *Oxford Master Series in Physics*. OUP Oxford, 2009.

[14] T. K. Gaisser, R. Engel, and E. Resconi, *Cosmic Rays and Particle Physics*. Cambridge University Press, 2 ed., 2016.

[15] M. Aguilar *et al.*, "Towards Understanding the Origin of Cosmic-Ray Electrons," *Phys. Rev. Lett.*, vol. 122, p. 101101, Mar 2019.

[16] M. Aguilar *et al.*, "Towards Understanding the Origin of Cosmic-Ray Positrons," *Phys. Rev. Lett.*, vol. 122, p. 041102, Jan 2019.

[17] Y. Bai, J. Berger, and S. Lu, "Supersymmetric resonant dark matter: A thermal model for the AMS-02 positron excess," *Phys. Rev. D*, vol. 97, p. 115012, Jun 2018.

[18] R. Cowsik, B. Burch, and T. Madziwa-Nussinov, "The Origin of the Spectral Intensities of Cosmic-Ray Positrons," *The Astrophysical Journal*, vol. 786, p. 124, Apr. 2014.

[19] V. Formato, "Precision Measurement of Boron-to-Carbon ratio in Cosmic Rays from 2 GV to 2 TV with the Alpha Magnetic Spectrometer on the International Space Station," *arXiv e-prints*, p. arXiv:1612.09160, Dec. 2016.

[20] J. A. Aguilar, "Particle Astrophysics Lecture 3: Cosmic Rays," 2018, (accessed June 2020). https://w3.iihe.ac.be/ aguilar/PHYS-467/PA3.pdf.

[21] R. A. Mewaldt, "The abundances of isotopes in the cosmic radiation," *AIP Conference Proceedings*, vol. 183, no. 1, pp. 124–146, 1989.

[22] N. E. Yanasak *et al.*, "Measurement of the Secondary Radionuclides ^{10}Be, ^{26}Al, ^{36}Cl, ^{54}Mn, and ^{14}C and Implications for the Galactic Cosmic-Ray Age," *The Astrophysical Journal*, vol. 563, pp. 768–792, Dec. 2001.

[23] T. Hams *et al.*, "Measurement of the Abundance of Radioactive ^{10}Be and Other Light Isotopes in Cosmic Radiation up to 2 GeV/Nucleon with the Balloon-borne Instrument ISOMAX," *Astrophysical Journal - ASTROPHYS J*, vol. 611, pp. 892–905, Aug. 2004.

[24] R. Streitmatter and S. Stephens, "The abundance of radioactive nuclei under different physical environments around the Solar System," *Advances in Space Research*, vol. 27, no. 4, pp. 743 – 748, 2001.

[25] I. V. Moskalenko *et al.*, "Propagation of light elements in the Galaxy," in *28th International Cosmic Ray Conference*, pp. 1917–1920, June 2003.

[26] S. Wakely *et al.*, "Prospects for High Energy Light Isotope Measurements on Balloons," in *34th International Cosmic Ray Conference (ICRC2015)*, PoS(ICRC2015)682, 2015.

[27] P. Allison *et al.*, "Cosmic-ray Isotope Measurements with HELIX," in *36th International Cosmic Ray Conference (ICRC2019)*, PoS(ICRC2019)121, 2019.

[28] J. Beatty *et al.*, "Cosmic-ray isotope measurements with HELIX," in *35th International Cosmic Ray Conference (ICRC2017)*, PoS(ICRC2017)226, 2017.

[29] C. Evoli *et al.*, "AMS-02 beryllium data and its implication for cosmic ray transport," *Phys. Rev. D*, vol. 101, p. 023013, Jan 2020.

[30] R. Cowsik *et al.*, "Steady State of Cosmic-Ray Nuclei—Their Spectral Shape and Path Length at Low Energies," *Phys. Rev.*, vol. 158, pp. 1238–1242, June 1967.

[31] S. Wakely, "HELIX: The High Energy Light Isotope Experiment," *NASA Proposal 14-APRA14-121*, Jan. 2014.

[32] P. Black, "Balloons on Ice: Final Flight Launches in Antarctica," Dec 2016, (accessed June 2020). https://www.nasa.gov/feature/balloons-on-ice-final-flight-launches-in-antarctica.

[33] NASA, "Scientific Balloons: Technology," (accessed June 2020). https://sites.wff.nasa.gov/code820/ technology_balloon_types.html.

[34] HEAT, "HEAT (High-Energy Antimatter Telescope)," (accessed June 2020). http://stratocat.com.ar /fichas-e/1994/FSU-19940503.htm.

[35] P. Allison *et al.*, "The Design and Construction of the HELIX RICH Detector," in *36th International Cosmic Ray Conference (ICRC2019)*, PoS(ICRC2019)152, 2019.

[36] Weeroc, "Citiroc 1a," (accessed August 2020). https://www.weeroc.com/products/sipm-read-out/citiroc-1a.

[37] M. Tabata *et al.*, "Recent Progress in Silica Aerogel Cherenkov Radiator," *Physics Procedia*, vol. 37, pp. 642 – 649, 2012. Proceedings of the 2nd International Conference on Technology and Instrumentation in Particle Physics (TIPP 2011).

[38] M. Tabata *et al.*, "Hydrophobic silica aerogel production at KEK," *Nucl. Instrum. Methods Phys. Res. A*, vol. 668, pp. 64–70, Mar. 2012.

[39] P. Allison *et al.*, "Production of silica aerogel radiator tiles for the HELIX RICH detector," in *36th International Cosmic Ray Conference (ICRC2019)*, PoS(ICRC2019)139, 2019.

[40] M. Tabata *et al.*, "Developing a silica aerogel radiator for the HELIX ring-imaging Cherenkov system," *Nucl. Instrum. Methods Phys. Res. A*, vol. 952, p. 161879, 2020.

[41] R. Prechelt, "Measurement of the Refractive Index of Aerogel for Ring Imaging Cherenkov Detectors ," Master's thesis, University of Chicago, 2017.

[42] M. N. Polyanskiy, "Refractive index of air - ciddor," (accessed August 2020). https://refractiveindex.info/?shelf=otherbook=airpage=Ciddor.

[43] LHCb, "RICH detectors," (accessed June 2020). https://lhcb-public.web.cern.ch/en/Detector/RICH2-en.html.

[44] M. Alemi *et al.*, "A RICH with aerogel: a study of refractive index uniformity," in *2004 IEEE Nuclear Science Symposium and Medical Imaging Conference*, no. 1, pp. 637–641, 2004.

[45] AMS-02, "The Ring Imaging Cherenkov Detector (RICH)," (accessed June 2020). https://ams02.space/detector/ring-imaging-cherenkov-detector-rich.

[46] O. Bourrion *et al.*, "Design and construction of a Cherenkov imager for charge measurement of nuclear cosmic rays," *Journal of Instrumentation*, vol. 6, p. P06004, June 2011.

[47] Y. Sallaz-Damaz *et al.*, "Characterization study of silica aerogel for Cherenkov imaging," *Nucl. Instrum. Methods Phys. Res. A*, vol. 614, no. 2, pp. 184 – 195, 2010.

[48] T. Rosin, "Caractérisation optique des tuiles d'aérogel pour le détecteur RICH d'HELIX," Master's thesis, 2019.

[49] C. K. Ross *et al.*, "Measurement of multiple scattering of 13 and 20 MeV electrons by thin foils," *Medical Physics*, vol. 35, no. 9, pp. 4121–4131, 2008.

[50] Toshiba, *TOSHIBA CCD Linear Image Sensor TCD1304DG*, 2019. https://toshiba.semicon-storage.com/us/semiconductor/product/linear-image-sensors/detail.TCD1304DG.html.

[51] Keysight, "U1063A 8-bit High-Speed cPCI Digitizers," (accessed June 2020). https://www.keysight.com/en/pd-1184894-pn-U1063A/acqiris-8-bit-high-speed-cpci-digitizers?cc=CAlc=eng.

[52] Arduino, "Arduino Mega 2560 Rev3," (accessed June 2020). https://store.arduino.cc/usa/mega-2560-r3.

[53] iminuit team, "iminuit A Python interface to Minuit." https://github.com/scikit-hep/iminuit, 2018, (accessed June 2020).

[54] E. Nappi and J. Seguinot, "Ring Imaging Cherenkov Detectors: The state of the art and perspectives," *Nuovo Cimento Rivista Serie*, vol. 28, pp. 1–130, 07 2005.

[55] I. Frank and I. Tamm, *Coherent Visible Radiation of Fast Electrons Passing Through Matter*, pp. 29–35. Springer Berlin Heidelberg, 1991.

[56] H. Alaeian, "An Introduction to Cherenkov Radiation," Mar 2014. http://large.stanford.edu/courses/2014/ph241/alaeian2/.